M 2014

U.PORTO
FEUP FACULDADE DE ENGENHARIA
UNIVERSIDADE DO PORTO

ANALYSIS OF GATED MYOCARDIAL PERFUSION SPECT IMAGES USING COMPUTATIONAL IMAGE REGISTRATION TECHNIQUES

RAQUEL DA SILVA ALVES
DISSERTAÇÃO DE MESTRADO APRESENTADA
À FACULDADE DE ENGENHARIA DA UNIVERSIDADE DO PORTO EM
ÁREA CIENTÍFICA

ANALYSIS OF GATED MYOCARDIAL PERFUSION SPECT IMAGES USING COMPUTATIONAL IMAGE REGISTRATION TECHNIQUES

Dissertation submitted in fulfillment of the requirements of "Dissertation" Course of Master Degree in Biomedical Engineering

Raquel da Silva Alves

Degree in Biomedical Engineering from the University of Trás-os-Montes and Alto Douro (2012)

Monograph prepared under the supervision of:

Professor Doutor João Manuel R. S. Tavares (supervisor)
Department of Mechanical Engineering
Faculdade de Engenharia da Universidade do Porto, Portugal

Professor Doutor Durval Campos Costa (co-supervisor)
Nuclear Medicine – Radiopharmacology
Champalimaud Centre for the Unknown
Champalimaud Foundation

Abstract

Modern medicine has been widely using imaging as a fundamental tool to aid in diagnosis procedures, monitoring the evolution of pathologies and the planning of treatments and surgeries. Myocardial perfusion is commonly studied through the evaluation of the left ventricular function using stress-rest gated myocardial perfusion single photon emission computed tomography (SPECT). SPECT provides a suitable identification of the myocardial region, facilitating both the identification and localization of perfusion abnormalities. A suitable performance of semi- or full automated methods for intra- or inter-modality registration and automated methods for computer quantification of LV functional abnormalities can minimize inter- and intra-observer variability and increase the reproducibility, which have an important role in risk stratification and selection of the best treatment strategy.

Here, computational techniques of medical image analysis, mainly of image registration, are integrated in a computational solution to automatically compute a set of features from myocardial perfusion SPECT images and use them to statistical analysis and classification of patient exams as from a healthy patient or with an associated disease. The image registration algorithms used, including the transformation, similarity measure, optimization and interpolation algorithms, will be described and discussed, as well as the computational processing, analysis and classification techniques employed. Experimental results will be presented and discussed.

Keywords: Image registration, image processing and analysis, image segmentation, image classification, myocardial perfusion SPECT images.

Resumo

A medicina moderna tem vindo a utilizar a imagiologia como uma ferramenta fundamental no apoio aos procedimentos de diagnóstico, monitorização da evolução de patologias e planeamento de tratamentos e cirurgias. A perfusão do miocárdio é comummente estudada através da avaliação da função do ventrículo esquerdo (VE) usando a tomografia computorizada por emissão de um único fotão (SPECT) com acoplamento ao sinal electrocardiográfico em estado de esforço físico e de repouso. A SPECT permite identificar a região do miocárdio, facilitando a identificação e localização de anormalidades de perfusão. Uma performance adequada de métodos semi ou completamente automáticos para o alinhamento inter- e intra-modalidades, e também de métodos automatizados para a quantificação computorizada das anormalidaes funcionais do VE, podem minimizar a variabilidade intra- e inter-observador, aumentando a reprodutibilidade que é fundamental para a estratificação do erro e selecção da melhor estratégia de tratamento.

Nesta dissertação, técnicas computacionais de análise de imagem médica, principalmente de alinhamento de imagem, são integradas numa solução computacional que automaticamente calcula um conjunto de características de imagens SPECT de perfusão do miocárdio. Estas são utilizadas para análise estatística e classificação dos pacientes como estando associados a pacientes saudáveis ou com doenças cardíacas associadas.

***Palavra-chave**: Alinhamento de imagem, processamento e análise de imagem, segmentação de imagem, classificação de imagem, imagens SPECT de perfusão do miocárdio.*

Agradecimentos

Ao orientador Prof. Dr. João Manuel R.S. Tavares, pelo apoio e orientação prestados ao longo deste mestrado, tanto ao nível da dissertação como na publicação de comunicações científicas relacionadas.

Ao co-orientador Prof. Dr. Durval Campos Costa, da Fundação Champalimaud, pela sua disponibilidade para orientação da presente dissertação e pela oportunidade de trabalhar com um profissional da sua excelência.

Ao Diogo Faria, do Hospital dos Lusíadas Porto, pela disponibilidade e apoio técnico constantes. Sem o seu contributo, esta dissertação não seria possível.

À Universidade de Trás-os-Montes e Alto Douro que em muito contribuiu para a minha formação pessoal e profissional em Engenharia Biomédica, nomeadamente aos professores que me orientaram durante todo o meu percurso académico.

A Vila Real, uma cidade que deixa saudade, pela sua beleza, pelo espírito académico, pelas pessoas com que me permitiu cruzar, pelas histórias que guardo na memória, pelos companheiros e afilhados da praxe académica e pelos amigos que ficaram para a vida.

À Faculdade de Engenharia da Universidade do Porto, que com a sua excelência, levou ao amadurecimento exponencial dos meus conhecimentos em Engenharia Biomédica.

À Banda Musical de Gondomar, e ao maestro Luís Carvalhoso, que compreendeu a disponibilidade reduzida para as actividades relacionadas durante este ano lectivo, devido ao estatuto trabalhadora-estudante.

À Prof. Isabel Anjo, que além da sua disponibilidade e excelente trabalho como professora de saxofone, sempre compreendeu a difícil conciliação de horários entre o ensino superior e o curso suplementar de saxofone. Nos últimos 8 anos, o apoio demonstrado nos momentos de maior pressão e as muitas histórias e gargalhadas partilhadas merecem um agradecimento muito especial.

A toda a minha família, avós, padrinhos, tios, primos e afilhada, pelo apoio e carinho que mostram diariamente, sempre disponíveis a ajudar em vários aspetos e presentes nos momentos mais importantes da minha vida. Ao meu avô Franklim.

Aos meus pais, ao meu irmão e ao meu namorado, pelo apoio, compreensão, paciência, dedicação, carinho e amor incondicional nas horas mais difíceis e pelos muitos sorrisos, alegrias e momentos fantásticos. Um agradecimento especial aos meus pais, pelo esforço financeiro que sempre fizeram para me proporcionar formação enquanto engenheira biomédica e também saxofonista.

A todos aqueles que, de forma direta ou indireta, contribuíram para a realização desta dissertação, e acima de tudo, contribuíram para o meu crescimento pessoal e profissional, muito obrigada!

CONTENT

CONTENT xi
LIST OF FIGURES xiii
LIST OF TABLES xv

Chapter 1 1

Introduction 1
1.1. Motivation & Goals 1
1.2. Organization 2
1.3. Contributions 3

Chapter 2 5

Gated Myocardial Perfusion SPECT Images 5
2.1. Single Photon Emission Computed Tomography 6
2.1.1. Radiotracers 7
2.1.2. Detectors 8
2.1.3. Deterioration factors and corrections 9
2.1.4. Image reconstruction algorithms 11
2.1.5. Spatial Resolution 12
2.1.6. SPECT Multimodalities 13
2.1.7. Pre- and Clinical Applications 14
2.2. Myocardial Perfusion SPECT Study 15
2.2.1. General principles 16
2.2.2. Radiotracers and clinical protocols 17
2.2.3. Image acquisition and reconstruction 18
2.2.4. Image analysis 18
2.2.5. Clinical applications 20
2.3. Conclusions 21

Chapter 3 23

Medical Image Registration 23
3.1. Registration methods: classification 24
3.2. Image registration techniques 25
3.2.1. Geometric transformations 29
3.2.2. Similarity measures 31
3.2.3. Optimization 33
3.2.4. Interpolation 34
3.3. Accuracy Assessments and Validation 35
3.4. Image registration software packages 36
3.5. Registration in Nuclear Medical Imaging 40
3.6. Conclusions 41

Chapter 4 ..... **43**

Image processing, segmentation and quantitative analysis **43**
4.1. General Principles of Digital Image 44
4.2. Image processing 45
4.2.1. Image intensity normalization 45
4.2.2. Image resampling 46
4.2.3. Image interpolation 46
4.2.4. Image averaging 47
4.2.5. Morphological Image Processing 48
4.3. Image segmentation 49
4.3.1. Otsu thresholding 50
4.3.2. K-Means Clustering 51
4.3.3. Region growing 52
4.3.4. Level set methods 53
4.4. Image Quantitative Analysis 54
4.4.1. Labeling 54
4.4.2. Extraction of geometric dimensions 54
4.5. Image classification 56
4.5.1. Bayesian classifier 56
4.6. Evaluation 57
4.7. Conclusions 59

Chapter 5 ..... **61**

Developed implementation, results and discussion **61**
5.1. Implementation 62
5.2. Material and methods 62
5.2.1. Dataset 62
5.2.2. Template myocardial SPECT image 62
5.2.2.1. Healthy myocardial SPECT image registration 63
5.2.2.2. Segmentation of the LV and computation of related geometric dimensions 65
5.2.2.3. Coronary artery mapping 66
5.2.2.4. Registration of coronary artery mapping 67
5.2.3. Myocardial SPECT image segmentation and registration 70
5.2.4. Statistical analysis and image classification 72
5.3. Results 74
5.3.1. Template myocardial perfusion SPECT 74
5.3.2. Segmentation validation 76
5.3.3. Bayesian classifier evaluation 79
5.4. Discussion 88
5.5. Conclusions 91

Chapter 6 ..... **93**

Final considerations **93**
6.1. Final conclusions 93
6.2. Future works 94

References **97**

LIST OF FIGURES

Figure 2.1. Different configuration of detectors in gamma camera: single head (a), two orthogonal heads (b), two opposed heads (c), three heads (d), four heads (e) and multiple small-FOV scintillation detectors [11]. 9

Figure 2.2. Detection of liver abnormalities using CT (on the left), SPECT (on the middle) and fused SPECT/CT (on the right) [25]. 13

Figure 2.3. Principle of ECG-gated acquisition. Each cardiac cycle is represented by the R-R interval, divided into 8 frames of equal duration (A). Over multiple cardiac cycles, image data from each frame are acquired (B). Each data set represents a specific phase of cardiac cycle, which provides a volume curve representing endocardial volume for each of 8 frames (C). ED:end-diastole; ES: end-systole [79]. . 17

Figure 2.4. Myocardial perfusion imaging can be gated either using stress-rest (A) or rest-stress sequence(B), with 99mTc [79]..... 17

Figure 2.5. (a) From left to right, short axis, horizontal long axis and vertical long axis (adapted from [214]) and (b) correspondent myocardial perfusion SPECT slices, for perfusion analysis. 19

Figure 2.6. (a) Polar map representing LV normal perfusion distributions using Emory Cardiac Toolbox, for a stress sestamibi with attenuation correction. Regional tracer uptakes varies (adapted from [90]) (b) 20-segment model for apical, mid-cavity, basal of short axis and long axis (from left to right) [78]..... 20

Figure 3.1. Diagram of a typical feature-based registration algorithm [73]. 28

Figure 3.2. General scheme of the image registration methods based on the optimization of a cost function (adapted from [100])..... 29

Figure 3.3. Types of geometrical transformations: identity transformation (left); rigid transformation (center) and affine transformation (right) (adapted from [100]). 30

Figure 3.4. Application of the sum of absolute differences (SAD) to stress the differences between two images, before registration (up) and after registration (down). Before registration, or poor aligned images, the images give rise to large absolute differences, while the sum of absolute differences of well aligned images results in small differences..... 33

Figure 4.1. Digital image general framework..... 44

Figure 4.2. Image intensity normalization of (a) identity image results in (b) higher contrast image [206]. 45

Figure 4.3. Image interpolation results: (a) application of nearest neighbor interpolation and (b) using bilinear interpolation [206]. 46

Figure 4.4. Noise reduction of (a) X-ray image of circuit board corrupted by salt-and-pepper noise, using a 3 x 3 avraging mask, resulting in image (b) [206]. 47

Figure 4.5. Morphologic operations results of opening and dilation using object A (top row). The structuring element is the small circle, whose dot is its center. Opening operation consists of the application of erosion (second row) followed by dilation (third row). Closing operation consists of the application of dilation (forth row) followed by erosion (fifth row). 49

Figure 4.6. Application of Otsu thresholding method on a clear bi-modal image (a), resulting in a well segmented image (b). 51

Figure 4.7. (a) HLA myocardial perfusion slice. (b) Segmentation using k-means (3 clusters). (c) Segmentation using k-means (5 clusters). Note that an inappropriate choice of the number of clusters **k** may yield poor results, if the number of clusters in the data set is quite different. 52

Figure 4.8. Segmentation of (a) HLA myocardial perfusion slice using region growing method, resulting in image (b). The difficult definition of the stopping criteria can result in lack of accuracy. 52

Figure 4.9. Identification of three objects through different color labels. 54

Figure 4.10. Statistical pattern classification [181]. 57

Figure 5.1. Algorithm framework implemented to generate a template myocardial perfusion SPECT image. 64

Figure 5.2. Segmentation algorithm. 67

Figure 5.3. Pre-registration algorithm used to align the image's slices under study with the corresponding coronary artery mapping. 68

Figure 5.4. Segmentation and registration of patient's exam. Image segmentation provides an accurate visual analysis and image registration of the patient's exam with the template image enables a correct computation of related geometric dimensions according to the normal heart size. Note that the template image slices is chosen according the clinical protocol and axis of the image under study. 71

Figure 5.5. Algorithm used to perform statistical analysis and image classification. .. 73

Figure 5.6. Segmented template stress SPECT image obtained using computer image registration techniques: (a) SA ; (b) HLA ; (c) VLA. 75

Figure 5.7. Segmented template rest SPECT image obtained using computer image registration techniques: (a) SA ; (b) HLA ; (c) VLA. 75

Figure 5.8. 20-segments coronary artery mapping template SPECT for stress studies: (a) SA ; (b) HLA ; (c) VLA. 76

Figure 5.9. 20-segments coronary artery mapping template SPECT for rest studies: (a) SA ; (b) HLA ; (c) VLA. 76

LIST OF TABLES

Table 2.1 Commonly used single photon emitting radionuclides (adapted from [6]).... 7

Table 3.1 Classification of medical image registration methods (adapted from [73])..26

Table 4.1. Confusion matrix (adapted from [182]). 58

Table 4.2. Definition of performance metrics and respective mathematical formulas.58

Table 5.1. Main parameters' values defined in the pre-registration algorithm of healthy myocardial SPECT images.....65

Table 5.2. Main parameters' values defined in the registration algorithm of healthy myocardial SPECT images.....66

Table 5.3. Main parameters' values defined in the pre-registration algorithm used for aligning the template myocardial perfusion SPECT images with the coronary artery mapping. 69

Table 5.4. Main parameters' values defined in the registration algorithm used for aligning the template myocardial perfusion SPECT images with the coronary artery mapping. 69

Table 5.5. Dice's coefficient computation between manual segmentation and five automated methods. 76

Table 5.6. Dice's coefficient computation between a manual segmentation of a clinical expert and five automated methods. 77

Table 5.7. Geometric dimensions of the segmented objects. 79

Table 5.8. HLA geometric dimensions of segmented structures and respective Bayesian classification results and comparison with clinical diagnosis. 80

Table 5.9 VLA geometric dimensions of segmented structures and respective Bayesian classification results and comparison with clinical diagnosis. 82

Table 5.10. SA geometric dimensions of segmented structures and respective Bayesian classification results and comparison with clinical diagnosis. 85

Table 5.11. Confusion matrix obtained from Bayesian classifier results. 88

Table 5.12. Performance measures of the proposed classification method.....88

ABBREVIATIONS AND SYMBOLS

List of abbreviations (sorted alphabetically)

AIR Automated Image Registration

AMIDE Amide is a Medical Image Data Examiner

ANTs Advance Normalization Tools

ART Algebraic Reconstruction Techniques

CC Correlation Coefficient

CT Computerized Tomography

ERNA Equilibrium Gated Radionuclide Angiography

FFD Free Form Deformation

FIRE Functional Image Registration

FLE Fiducial Localization Error

FOV Field-Of-View

FPRNA First-Pass Radionuclide Angiography

FRE Fiducial Registration Error

GLIRT Groupwise and Longitudinal Image Registration Toolbox

GSPECT Gated Single Photon Emission Computed Tomography

ITK Insight Toolkit

LOP Left Posterior Oblique

LV Left Ventricle

LVEF Left Ventricle Ejection Fraction

MAbs Monoclonal Antibodies

MAP Maximum A Posteriori

MART Multiplicative Algebraic Reconstruction Techniques

MI Mutual Information

MIRT Matlab Image Registration Toolkit

MLEM Maximum-Likelihood Expectation Maximization

MRI Magnetic Resonance Imaging

OpenGL Open Graphics Library

OSEM Ordered Subset Expectation Maximization

OSL One Step Late

PET Positron Emission Tomography

PIU Partitioned Intensity Uniformity

PTM Photo-Multiplier Tubes

RC Residual Complexity

RMIPs Radiolabeled molecular imaging probes

RIU Ratio Image Uniformity

RMS Root Mean Square

SAD Sum of Absolute Differences

SD Standard Deviation

SPM Statistical Parametric Mapping

SPECT Single Photon Emission Computed Tomography

SSD Sum of Squared Intensity Differences

TPS Thin-Plate Splines

TPS-RMS Thin-Plate Spline Robust Point Matching

TRE Target Registration Error

VIR Variance of Intensity Ratios

VTK Visualization Toolkit

WBR Wide Beam Reconstruction

WLS-CG Weighted Least-Squares Conjugate Gradient

List of symbols

γ Gamma ray

Chapter 1

Introduction

1.1. Motivation & Goals

Modern medicine has been widely using imaging as a fundamental tool to aid in diagnosis procedures, monitoring the development of disease and planning treatment or even surgeries. Thus, it became a key element to support medical decision making through non-invasive procedures. In the last years, deep researches and developments have been increasing lead to a higher number of information types that can be acquired from such diagnostic tool.

Image registration computer techniques enable the integration of different medical image modalities and the easier detection of changes between images acquired from different points of view, different acquisition times or even with subject atlas to attain prior anatomic or functional information. It stresses changes in size, shape or image intensity over time, and relates both preoperative image and surgical plans to the physical reality of patients during intervention and aligns patient's anatomy to a standardized atlas.

Techniques of image registration aim the establishment of spatial correspondence with the goal of find the optimal transformation that best aligns the structures of interest in the input images. The minimization of an error measure, or of a cost function, is the goal of these techniques. Additionally, an optimization algorithm is needed to find the most suitable transformation, and an interpolator is employed to resample the features into the new registered space.

The application of image registration techniques in nuclear medicine includes correlative image interpretation, attenuation correction, scatter correction, correction for limited resolution and improvement of the reconstruction accuracy in emission tomography. These techniques also have been used in the co-registration of serial functional studies, for the transformation to standard spaces for their comparison with both normal studies and data from other modalities, in conformal radiotherapy treatment planning and functionally guided procedures. Besides, have been improving the interpretation of several functional studies based on static images, including brain, breast, chest, liver, kidneys and colon images, or on the motion analysis as in cardiac and lung studies.

Myocardial perfusion is commonly studied through the evaluation of the left ventricular function using stress-rest gated myocardial perfusion single photon emission computed tomography (SPECT). SPECT provides a suitable identification of the myocardial region, facilitating both the localization and definition of perfusion abnormalities [2]. The automated computer quantification of LV functional abnormalities can minimize inter- and intra-observer variability and increase the reproducibility, which have an important role in risk stratification and selection of the best treatment strategy. With such computational solution, the prevalence and clinical predictors of both myocardial ischemia and infarct in suspicious patients can be easier assessed.

Motivated by the potentialities of the application of computational techniques on stress-rest gated myocardial perfusion SPECT images referred above and their application, the goal of this dissertation consists of developing a computational solution to automatically compute a set of features from myocardial perfusion SPECT images and use them to statistical analysis and classification of patient's exams as from a healthy patient or with an associated disease.

1.2. Organization

This dissertation is divided into the following chapters:

2. Gated Myocardial Perfusion SPECT Images

The second chapter describes SPECT imaging modality, describing the radiotracers commonly used, detectors and related image reconstruction algorithms.

Its main advantages and problems are referred, as well as clinical applications. Therefore, general principles of myocardial perfusion gated SPECT are exposed.

3. Medical Image Registration

In this chapter, medical image registration is presented through a state-of-the-art by the study and description of its methodologies and respective classification, as well as the main types of transformations, similarity measures, optimization and interpolation techniques involved in the process.

4. Image processing, segmentation and quantitative analysis

Computational image techniques employed in this experimental implementation are described.

5. Experimental implementation

The computational solution developed to automatically segment, analyze and classify the images as from subjects with myocardial perfusion associated diseases or not is described. Experimental results will be also presented and discussed.

6. Final considerations

Final conclusions and future works will be described in this last chapter.

1.3. Contributions

This dissertation presents a deep study and bibliographic revision of scientific literature in medical image registration and its applications on nuclear medicine images, specifically in gated myocardial perfusion SPECT images. The main contribution is the development of a template myocardial perfusion SPECT image and its coronary artery mapping, enabling the computation of mean geometric dimensions in healthy patients. Thus, image classification is reached through registration of the patient's images under study with the template myocardial perfusion SPECT and comparison of related geometric dimensions.

Chapter 2

Gated Myocardial Perfusion SPECT Images

Nuclear image modalities have been widely used in healthcare diagnostic since it provides a physiological diagnose through the use of radiotracers to map metabolism and fluid flow on tissues or organs. Unlike other imaging techniques, emission tomography modalities assess both the perfusion and metabolic activity, even if there are no changes from the structural point of view. It is commonly used as a diagnose complement in oncology, cardiology and neuropsychiatric disorders.

The enhancement of digital medical image acquisition and analysis, such as higher spatial and temporal resolutions, is actually the hot topic of medical imaging modalities. However, image analysis cannot be properly achieved without the development or better integration of different registration methods. They enable the integration of different medical image modalities, such as Positron Emission Tomography (PET), Single Photon Emission Computed Tomography (SPECT), Computerized Tomography (CT) and Magnetic Resonance Imaging (MRI), through the detection of differences between images acquired from different points of view, different time acquisition or even different subject atlas, to obtain anatomic and functional information that reflects completely the condition of the patient, providing a more complete information for supporting medical diagnosis.

The combined evaluation of myocardial perfusion and left ventricular function within a single study is carried out through electrocardiographically gated myocardial perfusion SPECT (GSPECT). This technique has been improving through

image processing and quantification, since it enhances diagnostic and prognostic capability of myocardial perfusion imaging. Furthermore, computation image techniques improve incremental information over the perfusion data and enables myocardial viability assessment and sequential follow-up after therapy.

In this chapter, SPECT imaging modality will be described, namely the radiotracers employed, detectors, image data acquisition, image reconstruction and algorithms in 2D and 3D, such as the common sources of degradation factors that minimize the quality of the images acquired and its corrections. Hybrid systems with molecular modalities commercially available and their applications are also reviewed. Its application as GSPECT is explored, namely general principles, clinical protocols and image analysis currently employed.

2.1. Single Photon Emission Computed Tomography

Single photon emission computed tomography is a nuclear image modality that uses radioactive tracers, to measure and evaluate both the perfusion and metabolic processes of the individual or object under study. SPECT studies are based on electronic detection of photons, by an Anger gamma camera, administered by intravenous injection into the human body, generating three-dimensional images of the radiopharmaceutical distribution [1].

The development of 3-D algorithms was fundamental to the evolution of SPECT till nowadays. Without improvements of the Anger camera with a rotating collimator attachment and the optimization of reconstruction algorithms or interactive methods, it would not be possible to improve the low contrast characteristic of the blurred SPECT images.

High-speed digital computer systems for acquisition and display of dynamic processes in the body such as the development of high-speed dynamic radionuclides, dual- and triple-camera contributed to an efficient molecular imaging modality. SPECT uses time as an additional coordinate, by collecting different information as a function of time and translating this into spatial information [2]. Accordingly, it is a valuable diagnostic imaging modality [3].

2.1.1. Radiotracers

Respecting single photon emitting radiopharmaceuticals, it must be considered the wide availability of the radioligands as a relative ease of labeling, which is based on the consumption of oxygen. Thus, SPECT has the ability of detecting and monitoring biological and pathophysiological processes, using radiolabeled peptides and drugs [4].

The radiotracers commonly used can be classified into the following groups:

- Radiolabeled molecular imaging probes (RMIPs) are highly specific radiolabeled. They allow visualization, characterization and measurement of biological processes in living systems, but must be design and chosen depending on the organ of study. Furthermore, they are classified based on their utility and nature of application, resulting in radiolabeled drug substance, radioligands [5], pathway marker and biomarkers.

- Peptides and proteins enable finding radiolabeled monoclonal antibodies (MAbs). Their specifically binding forms an antigen-antibody complex, ^{99m}Tc-labeled monoclonal antibodies, sulesomab, annexin V and radiolabeled peptides.

- Hypoxia imaging and cell labeling are also used, but in fewer applications [6].

Table 2.1. synthetizes the main radionuclides employed in SPECT studies and their most relevant characteristics.

Table 2.1 Commonly used single photon emitting radionuclides (adapted from [6]).

Radionuclide	Half-life	Energy	Mode of decay
Tc-99m	6.92h	142keV	Isometric Transition (100%)
I-131	8.03 days	364keV	Beta-minus (100%)
I-123	13.22h	159keV	Electron Capture (100%)
In-111	2.80days	171,245keV	Electron Capture (100%)

These radiopharmaceuticals contain long-lived radioisotopes emitting gamma rays that decay through an isometric transition, i.e. a nuclear de-excitation resulting

in the emission of a gamma ray or an electron by the process of internal conversion. The radioisotopes are metastable, characterized by relative long lifetimes, making them appropriate for in vivo imaging.

2.1.2. Detectors

Since it is a radionuclide imaging technology, the key elements in SPECT are (1) a highly specific biomarker, with sensitive characteristics to properly study the molecular or cellular phenomenon, and (2) an imaging device, consisting of a radiation detector with specific performance to localize the activity distribution within the human body [7–9].

A gamma camera consists of a collimator, a scintillation crystal that efficiently collects the scintillation of light and distributes it among a number of photo-multiplier tubes (PTMs). Then, the Anger gamma camera consists of a gamma ray position sensitive detector with crystal scintillators having position circuitry and energy determination [6].

The detection principle of gamma radiation is the same as PET, but the collimation principle is different [8]. SPECT collimators are mechanical structures made of high-Z material [10], which enhances the absorption of the oblique gamma rays, allowing the passage of radiation through the collimator openings. A centroid algorithm determines the interaction position of the gamma ray within the crystal [11].

Detectors geometries varies within parallel hole, pinhole, converging and diverging with various hole geometries [11]. Their design include rotating gamma camera, stationary detector or interchangeable multi-hole collimators [6]. However, it depends on the camera trademarks specifications. Figure 2.1 presents different configurations of gamma camera detectors.

Dedicated sodium iodide detector cardiac camera, dedicated upright and semi-reclining cardiac camera, cardiocentric, cardio-focused collimation, art detector geometry with rotating slit-hole collimation, multiple scanning parallel-hole collimators, multi-pinhole collimation such as solid-state detectors, indirect and direct solid-state detectors are some of the innovations in gamma cameras lately [12–14].

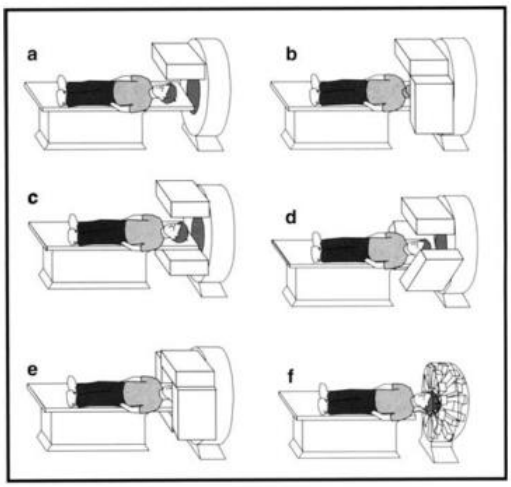

Figure 2.1. Different configuration of detectors in gamma camera: single head (a), two orthogonal heads (b), two opposed heads (c), three heads (d), four heads (e) and multiple small-FOV scintillation detectors [11].

2.1.3. Deterioration factors and corrections

Attenuation, scatter and resolution effects, as well as motion artifacts, are the main degradation factors of this imaging modality.

Attenuation is the most important factor of influence in spatial resolution, so the attenuation coefficients within the patient must be known, whose map is usually incorporated into an iterative algorithm. Besides the application of attenuation correction algorithms, the use of hybrid systems using a CT scanner enables lower image noise at the attenuation map, due to the less noise of CT image, faster acquisition and higher flux [15]. Furthermore, it is not influenced by cross-talk from SPECT radionuclides. However, its higher resolution implies fewer accuracy of the attenuation compensation [16]. Precision and noise of the attenuation correction also depends on both the emission and transmission statistics. Both transmission and emission noise and attenuation coefficients propagate into the images and the attenuation coefficients derived from the transmission image increase bias and noise as source decays. It is required transmission sources to be replaced frequently to maintain transmission statistics properly. This allows noise propagation at minimum values and ensure that the emission contamination do not overwhelm the transmission counts [17]. Another way to apply attenuation correction is the use of algorithms capable of removing the cross-contamination between the emission and transmission photons, whose simultaneous acquisition of emission and transmission data eliminate the misregistration between SPECT data and attenuation maps [16].

The distance-dependent attenuation can also be eliminated through the acquisition of projection scans for a complete rotation of the detector head, combining the measurement of opposing projections.

The Compton and Rayleigh (coherent) scattering are also common problems and depend on the energy of the emitted photons, making the photon to be deflected from its initial trajectory but still being detected from another detector or even never detected. It varies with the composition of the material through which the photons are travelling. Scattering compensation can be made without correction through minimizing the amount of scatter, modifying attenuation correction, filtering, or based on measurements, as dual and triple energy window corrections or even spectral models [10]. Other solutions are based on modeling the scatter distribution, using analytical models based on Klein-Nishina scatter equations [18], transmission-dependent convolution subtraction, object shape or slab-derived scatter estimation and reconstruction-based scatter correction including incorporation of fast Monte-Carlo scatter estimation. Incorporating multiple energy windows using multi-radionuclide SPECT and multi-energy radionuclides are also valuable scatter corrections [10].

Sensitivity is dependent on the material used and the thickness of the crystal, as well as on both geometry and material of mechanical collimation, which means that the scintillator's stopping power will be increased with the use of long crystals, as well as the number of detected events [11].

The dead-time losses and pile-up effects, processing electronics and systems' detectors cause underestimation of counts and can be compensated through mathematical models based on a count rate measurements covering the anticipated activity levels [11].

Respiratory, cardiac and patient motion effects can be compensated with a number of gated acquisitions realized for every breathing or cardiac cycle, producing a reconstructed image corresponding to a specific time frame of the cycle [11].

Note that a routine quality control of SPECT instrumentation is fundamental to detect changes in performance from a baseline condition, including a comprehensive suite of individual measurements to ensure adequate sensitivity to detect detrimental changes. So, it should not be burdensome; it reflects the clinical

use of the system, emphasizes measurements about system stability and reflects the system state adequacy for clinical use [19].

2.1.4. Image reconstruction algorithms

Image reconstruction in tomographic radionuclide-based systems consists on measured estimation of the integral of radiotracer distribution to produce a volume representation of the radiotracer distribution inside the patient's body.

The acquired data is organized as a number of counts along each LOR, which is the radial extension of the collimator hole across the field-of-view (FOV) in SPECT systems. For each projection, a 2D matrix contains the number of counts of every LOR at each angular view, called sinogram. Then, it is used as input for reconstruction algorithms in order to generate the final image [12].

Filtered Backprojection (FBP) has been used as an analytical reconstruction algorithm that models the measurement of radiotracer distribution calculated analytically, backprojecting and filtering homogenously each LOR. On the other hand, statistical iterative techniques solve many problems of diagnostic quality and quantitative accuracy compensating the inaccuracies introduced to the image, which is not possible with analytic approaches [20]. Iterative methods start with an estimation of the tracer distribution and compute the forward-projection, comparing calculated and measured projections; then, the image is updated according to the differences found. Maximum-Likelihood Expectation Maximization (MLEM) [21] and such as Ordered Subset Expectation Maximization (OSEM) are the most widely used iterative algorithms [22].

Wide Beam Reconstruction (WBR), an iterative and automatic algorithm, is a noise compensation technique that suppresses noise and enhances the signal-to-noise ratio through modeling the statistical characteristics of both emission process and detected data, counting for the Poisson distribution. This algorithm regularizes the likelihood objective function adding a Gaussian component. While the application of Gaussian components results in suppressed high-frequency components, Poisson components application results in the recovery of high-frequency signal. Then, the balance between them is adaptively and automatically determined according to the data analysis and desired smoothness [12].

There are other methods as Maximum A Posteriori (MAP) that suppresses the impact of noise, using a modified One Step Late (OSL) algorithm, with a Green prior optimized for each clinical protocol and for both gated and attenuation corrected image, and a Median root prior as last iteration [12]. More iterative algorithms commonly used are Algebraic Reconstruction Techniques (ART), Multiplicative ART (MART) and Weighted Least-Squares Conjugate Gradient (WLS-CG) [23].

Accordingly, an adequate filter, such as the cut-off frequency, is fundamental to obtain the optimal resolution and noise level in reconstructed images. The blurring effect can also be reduced with modeled edge penetration [24] and parallax errors in the reconstruction scheme [6].

2.1.5. Spatial Resolution

The spatial resolution of gamma cameras can achieve a sub-millimeter range, being even possible sub-half millimeters when it is used a specialized dedicated multi-pinhole geometry. Furthermore, it is improved with the application of a distance function of the object from the aperture and its distance from the detector surface, by minimizing the aperture size and specialized collimator geometry [6]. However, this causes the reduction of both detection efficiency, partially tackled by increasing the number of holes, and image field of view, such as insufficient data acquisition. Besides, given SPECT collimation is geometrical, spatial resolution depends on the distance between the source and the detector head, leading to distortions in the image if the process of reconstruction is not taken into account. This can be minimized with the use of reconstruction algorithms as descriptions of the resolution degradation based on measurements [11].

Consequently to a limited spatial resolution, a partial volume effect appears corresponding to the bias introduced on the estimation of the radiotracer concentration and depends on the size and shape of the object, such as the relative radiotracer concentration with respect to the surroundings. It can be minimized with a large object's size and its compensation is needed when the acquisition of quantitative information about the radiotracer distribution is wanted [11].

2.1.6. SPECT Multimodalities

Molecular SPECT imaging provides functional images with high spatial resolution but anatomical correlation. SPECT/MRI, SPECT-optical devices and SPECT/CT are used to extract more biological information with the same spatial and temporal framework, such as higher anatomical image resolution [25]. Thus, image fusion from different imaging modalities can aid in the decision making process, once it enables a better localization and definition of organs and lesions such as improves the precision of surgical biopsies, as exemplified in Figure 2.2.

A considerable work has been done on the development of algorithms for the co-registration of anatomical and functional images, making them more robust and accurate, providing accurate registration, which can be feature-based or volume-based. Those algorithms are fundamental to avoid misregistration due to patient motion and breathing artifacts, such as the fact that the acquisition of SPECT and CT or MRI data must be sequential.

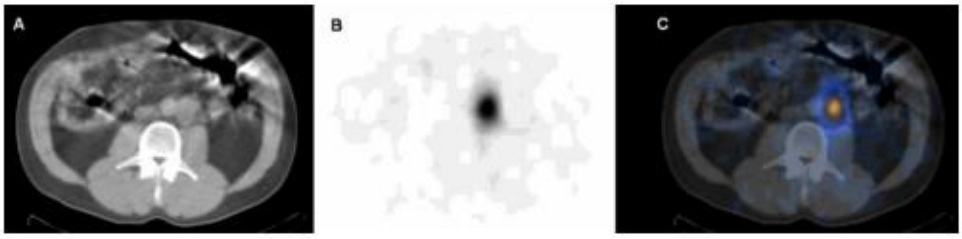

Figure 2.2. Detection of liver abnormalities using CT (on the left), SPECT (on the middle) and fused SPECT/CT (on the right) [25].

In SPECT/CT multimodality, there are scattering problems, truncation and beam hardening artifacts. Additionally, there are also misregistration between the emission and transmission in data, resulting on incorrect matching of the attenuation map to the emission data. It is also due to sagging of the emission table, as well as respiratory, cardiac and patient motion. To minimize the table sagging effect, the SPECT/CT systems employ a dual-table configuration whose patient pallet is a low attenuation carbon fiber tabletop, sited on the top of a second lower table, more rigid [16].

Respiratory and cardiac motions are more complicated to solve. It is fundamental SPECT/CT systems use a co-registration program to ensure correct alignment, associated with a quality control (QC) program to allow the re-alignment of different modalities images in manual or semiautomatic mode [21]. Quantifying

coronary artery calcium, evaluating the patency of vascular and coronary arteries and assessing myocardial perfusion, such as viability in one clinical setting, are some of the multiple applications where SPECT/CT has been applied, but it is necessary to become more available in the market, requiring lower costs [16].

In the last few years, integrated SPECT/CT systems have been widely used but MRI presents specific advantages compared with CT, such as lack of ionizing radiation, high soft-tissue contrast and sensitivity to tissue alterations evidenced by specific imaging sequences. However, using SPECT followed by MRI in clinical applications is a complicated task [26], once it requires transferring the patient to another system table and inherently separated dual-modality scans, followed by image fusion. Then, there are potential sources of misalignment due to uncontrolled movements and displacements of tissues and organs. Multiple anesthesia sessions are needed when SPECT and MRI devices are located in separate places, involving higher risks to the patient due to different biologic responses to anesthesia.

Attempting to compensate these problems, there are studies using SPECT followed by low spatial resolution MRI and also SPECT/MRI performed at very high magnetic fields to achieve high anatomic resolution, benefiting from a higher signal-to-noise ratio but it leads to field susceptibility artifacts and prevents closer proximity of SPECT scanner [27]. Hence, it is needed to minimize technical limitations of SPECT/MRI dual imaging, such as enhance registration methods [28]. Prototypes are being constructed to allow the minimization of all these problems, for applying dual modalities in clinical application, besides the many applications in pre-clinical applications [29–31].

Wherefore, integrated SPECT systems enable a direct correlation of anatomic and functional information resulting in a better definition and localization of scintigraphic findings [32].

2.1.7. Pre- and Clinical Applications

Preclinical models are valuable SPECT applications [33–35], having a great scope for noninvasively studies on dynamic biological processes at molecular and cellular levels. Through the assess of biological effects of drug candidates and the capability of following the development of certain diseases, molecular imaging plays an important role in the implementation of relevant animal therapeutic models in

vitro, such as cardiovascular imaging, imaging stem cells, oncologic applications [36, 37], neuroimaging applications [38–45] and drug discovery, using small-animal imaging [30, 31, 46, 47].

The preclinical application in SPECT leads to consequent applications in clinical cases, usually the same areas as PET. There are several reported cases study is scientific literature [48–50]. In oncology, it permits the detection of tumors at an early stage, since it is capable of detecting and analyzing the development state of cancer [4, 36, 51–53]. In cardiology, it allows the assessment of myocardial viability in coronary patients, allowing a more accurate selection of patients for revascularization procedures [54, 55], through the evaluation of myocardial perfusion [56–61]. In neurological and psychiatric disorders, SPECT has an important role in the study of Parkinson's disease [57–64], Alzheimer [39, 70–73], epilepsy [74], brain dementia [71] and movement disorders [69, 75–77].

Given the relevance of myocardial perfusion SPECT studies in this dissertation, general principles are next exposed, concerning radiotracers, image acquisition, image analysis and several diagnosis applications.

2.2. Myocardial Perfusion SPECT Study

The combined evaluation of myocardial perfusion and left ventricular function within a single study is carried out through electrocardiographically GSPECT, since it allows the quantification of degree and extent of the LV functional abnormalities [78]. However, it is not suitable for accurate RV function measurement because it is not properly visualized on the perfusion images.

This technique enables the quantitative or semi-quantitative assessment of the LV function simultaneously with the evaluation of the LV perfusion, which aid in the diagnosis, assessment of the risk and prognosis, determination of the myocardial viability and evaluation of the functional recovery after the revascularization procedure in patients with known or suspected coronary information over the perfusion data [79].

Similarly to SPECT clinical protocols exposed above, GSPECT studies require the injection of a perfusion tracer that is taken up by the myocardium. Delineation of the epicardial and endocardial edges on the perfusion image provides the definition of the LV myocardium and LV cavity [80]. LV function is based on the

quantitation of the changes in the LV volume, excursion of the endocardium and brightening of the myocardium from the end-diastolic image to the end-systolic image.

Besides there are more γ-camera imaging techniques available to measure the ventricular function, namely, first-pass radionuclide angiography (FPRNA) and equilibrium gated radionuclide angiography (ERNA), several factors contributed to the consistent growth of GSPECT popularity. It is simple and provides functional status information of a hypoperfused or normally perfused area. ^{90m}Tc-labeled perfusion tracers present favorable kinetics and consequently flexible acquisition protocols. Acquisition and processing time have shortened significantly due to continued improvements of multidetector γ-cameras. Computers and automation of computation image techniques has made SPECT a simple, practical and user friendly technique in clinical settings [81].

2.2.1. General principles

A γ-camera records the photons at multiple projection angles around the subject along 180º or 360º degrees. At each of the projection angles, one static image is acquired during an ungated image acquisition. Several dynamic images spanning the length of the cardiac cycle are acquired at equal intervals during ECG gated acquisition. This principle is illustrated in Figure 2.3. The number of frames can vary. An increased number of frames provides better temporal resolution, but each frame requires shorter duration and consequently the acquisition has to be prolonged to collect adequate counts.

A proper quality GSPECT study can only be achieved with an adequate count density, which is reached through gated data acquisition over many cardiac cycles. However, they may have different duration causing mix of counts from adjacent frames, known as temporal blurring, and compromise the quality of the study. Thereby, a range of acceptable beats or acceptance window, known as tolerance, is defined; it is expressed as the percentage of the mean R-R interval.

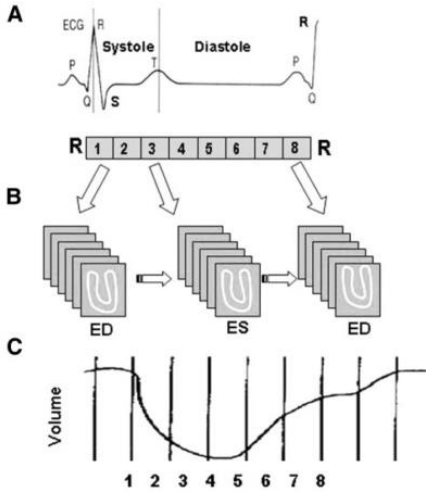

Figure 2.3. Principle of ECG-gated acquisition. Each cardiac cycle is represented by the R-R interval, divided into 8 frames of equal duration (A). Over multiple cardiac cycles, image data from each frame are acquired (B). Each data set represents a specific phase of cardiac cycle, which provides a volume curve representing endocardial volume for each of 8 frames (C). ED:end-diastole; ES: end-systole [79].

2.2.2. Radiotracers and clinical protocols

Usually, the radiotracers administered are ^{99m}Tc-sestamibi and ^{99m}Tc-tetrofosmin, since they have a short half-life without associated increase in the radiation burden and allow a higher dose results, with better count statistics in the images. Consequently, there are associated with lower statistical error and better image quality [82].

The clinical protocols employed can be a same-day or separate-day protocol, both illustrated in Fig. 2.4. Usually, stress study is gated as part of a low-dose rest/high-dose stress ^{99m}Tc or a rest ^{201}Tl/stress ^{99m}Tc sequence [83].

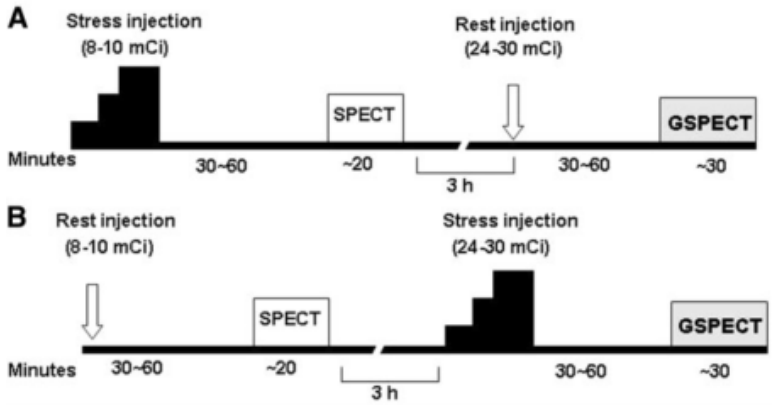

Figure 2.4. Myocardial perfusion imaging can be gated either using stress-rest (A) or rest-stress sequence(B), with ^{99m}Tc [79].

The perfusion pattern reflects the myocardial distribution of the tracer at the time of injection, representing the LV function at the time of acquisition. Depending on the health condition of the patient, post-stress gated images represent stress perfusion and rest function in healthy patient or patients with previous myocardial infarction, and a reduced function during the post-stress acquisition compared with the resting basal function in patients with severe ischemia. The standard GSPECT acquisition is generally completed within 20-30minutes. For viability assessment, the protocols consist of to inject the tracer at rest and gated acquisition is performed during infusion of an inotropic agent [79].

Patients with severe arrhythmia, such as atrial fibrillation, frequent premature ectopic beats and heart block should not perform GSPECT studies, i.e. patients whose heartbeat can be affected.

2.2.3. Image acquisition and reconstruction

Image acquisition is similar to a standard perfusion SPECT acquisition, but it is increased by the use of a 3-lead ECG that allows the mechanism for gating, providing the R wave. Its detection actives the gating device, that sends a signal to the acquisition computer, starting the acquisition. The frames are summed together, reconstructed and displayed in standard vertical long-axis, horizontal long-axis and short axis slices for perfusion analysis (see Fig. 2.5.). However, functional analysis requires raw data to be reconstructed frame by frame. Before reconstruction, it is fundamental to check raw projection data for potential sources of error and artifacts, since they propagate and compromise the accuracy of the measurements.

2.2.4. Image analysis

The definition of the normal limits and criteria for abnormalities are crucial for optimal interpretation [84], since visual analysis requires the reader to be familiar with the pattern of the normal LV contraction in different segments of the LV. An atlas is available in scientific literature, providing the reader with both image recognition and understanding of the basis for myocardial perfusion SPECT images interpretation [85]. Furthermore, the proper delineation of endocardial contour provides higher accuracy, but the edge detection is often inaccurate in patient with severe perfusion, large aneurysmal dilation, and significant structural distortion [86]. Accuracy is also affected in patients with a smaller heart [87–89].

(a)

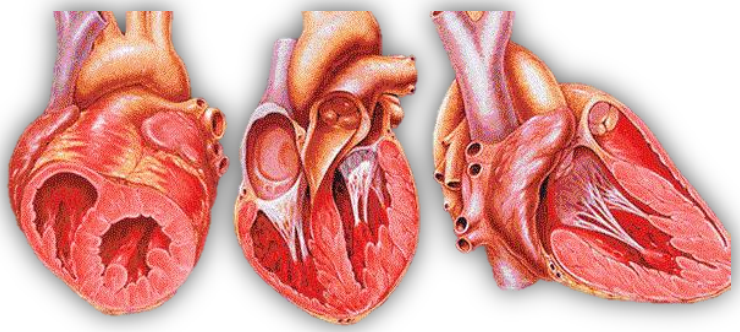

(b)

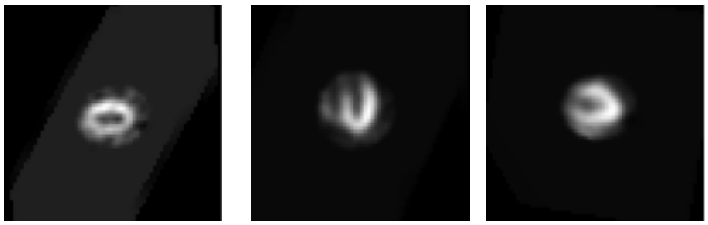

Figure 2.5. (a) From left to right, short axis, horizontal long axis and vertical long axis (adapted from [214]) and (b) correspondent myocardial perfusion SPECT slices, for perfusion analysis.

The use of computer techniques provides objective quantitative assessment in interpreting these studies [85–88]. There are commercially available software packages to analyze the reconstructed gated dataset, as QGS and Emory Cardiac Toolbox, developed at Cedars-Sinai Medical Center and Emory University, respectively [79, 86]. They provide LV volumes and LVEF measurements, both displayed on a segmental, circumferential model of the LV with each segment representing a particular region of the LV. Measurement of LV diastolic indices and LV mass are currently being developed.

The polar map approach is used for both representation of the patient's LV myocardial perfusion distribution and identification of hypoperfused segments. It consists of synthetizing the 3-dimensional maximal LV count distribution onto a single 2-dimensional polar map. The count distribution at the base of the LV corresponds to the intensity at the periphery and the count at the apex to the center of the polar map. Then, the patient's 3D LV myocardial perfusion tracer uptake ratio is compared with a statistically determined lower limit of normal LV volumes or LVEF [84], based on mean normal distribution and corresponding regional standard deviation (SD), allowing hypoperfusion detection. The extent of hypoperfusion is shown by a blackout or extent polar map, whose normalized counts of LV segments that fall below the lower limit of normal pattern are deemed to be hypoperfused [90]. Figure 2.6(a) illustrates the polar map approach.

The artery coronary mapping, used in visual assessment of perfusion, results from the division of the left ventricle into a variable number of segments. Usually, myocardial perfusion studies are displayed using 17 or 20 segments. The 20-segmented model, which is used in the experimental implementation presented in Chapter 5, divides the myocardial perfusion region into basal, mid-cavity and apical thirds, including 2 segments for the apical cap. This approach results in a 30% contribution from the base, 30% from the mid-cavity and 40% from the apex and apical cap [91]. The assignment of segments to coronary arterial territories is directly related with the coronary artery blood supply. As illustrated by Figure 2.6(b), segments 1, 2, 3, 7, 8, 13, 14, 19 and 20 are assigned to the left anterior descending coronary artery distribution; segments 4, 9, 10, 15 and 16 are assigned to the right coronary artery; segments 5, 6, 11, 12, 17 and 18 are assigned to the left circumflex artery [91].

(a) 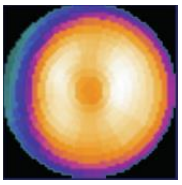 (b) 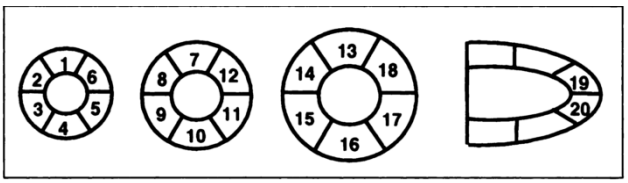

Figure 2.6. (a) Polar map representing LV normal perfusion distributions using Emory Cardiac Toolbox, for a stress sestamibi with attenuation correction. Regional tracer uptakes varies (adapted from [90]) (b) 20-segment model for apical, mid-cavity and basal locations of short axis, and long axis (from left to right) [78].

Quantitative programs have reduced subjectivity and demonstrated excellent inter- and intra-observer reproducibility, but repeatability on the same subject is affected by several factors, namely acquisition, data processing, quantification and physiologic variation [78, 94]. Besides, those software packages presents data that are not sufficiently intuitive to image analysis, since both statistical and visual information presented always require high professional experience from the clinical expert.

2.2.5. Clinical applications

Evaluation of myocardial perfusion GSPECT studies in patients with CAD provides additional information that cannot be obtained by perfusion imaging alone. While a normal perfusion study carries an excellent prognostic value, an abnormally low LVEF in the same patient may alert the physician for other comorbidities [81]. Nonischemic and ischemic dilated cardiomyopathy can be differentiated through

combined perfusion-function analysis. A common application is to classify a fixed perfusion defect as a soft-tissue attenuation artifact or an infarct.

Assessment of severity, risk stratification and prognosis [58, 95, 96], predicting future cardiac events after myocardial infarction, myocardial viability and follow-up after revascularization also benefits from GSPECT [90], due to its reproducibility and repeatability, objectiveness and extensively validation [98]. However, adequate patient selection, quality control, identification of technical limitations and application in appropriate clinical situations are important prerequisites for its optimal utilization.

Digital nuclear cardiology images coupled with the tremendous advances in computer hardware and software facilitates the development of total automatic image analysis for quantification of relevant parameters and computer-assisted decision support [99], as well as multidimensional and multimodality display.

2.3. Conclusions

Despite the satisfactory resolution and quality of images, research is ongoing, focused on developing better instrumentation and new software for improved performance, to reduce costs and make system more user-friendly. High technology prices and both technical and operational complexities serve as a barrier to expand the access to specialists and patients. Thus, despite the immense potential of this technology, these disadvantages require a clear definition of imaging modalities, usefulness in several fields of medicine.

In the last two decades, the greatest changes have been improving spatial resolution by decreasing the crystal size and there was also a significant progress in image quality by combining 3D reconstruction algorithms and attenuation correction, to enhance temporal resolution capabilities and get a maximum artifact-free imaging modalities, such as from dual-tracers imaging and the use of specialized collimators. Co-registration with images from complementary modalities has been employed in nuclear medicine, acting as an adjunct to interpret functional nuclear medicine images, as well as offers the ability to overcome some intrinsic limitations.

Multimodalities have been widely used in clinical environment and already had a valuable outcome on clinical oncology practice and cancer treatment. SPECT/CT systems applications are increasing slower due to its high cost. Although,

nuclear medicine can only benefit from such evolving integration, in which image registration plays a central role.

Due to the functional diagnosis that molecular imaging provides, SPECT will maintain its applications in clinical diagnosis, assessment of response to treatment and delivery of targeted therapies, namely in nuclear cardiac applications as myocardial perfusion GSPECT studies. Automatic analysis, quantitation and proper display algorithms for the assessment of perfusion and function from myocardial perfusion SPECT have been developed and demonstrated to run successfully in the vast majority of patients [81, 94]. Here, image registration plays a central role, since it permits the comparison of single scans with a normal database and the recognition of deficiencies in myocardial perfusion [100].

Chapter 3

Medical Image Registration

Modern medicine has been widely using imaging as a fundamental tool to assist diagnosis procedures, monitoring the evolution of pathologies and the planning of treatments and surgeries. However, the enhancement of digital medical images and its efficient analysis cannot be completely achieved without suitable semi- or full automated methods for image registration [101].

Computer techniques of image registration enable the fusion of different medical image modalities and the easier detection of changes between images acquired from different points of view, at different acquisition times or even against with atlas that includes anatomical and functional information. This task of image analysis can also stress changes in size, shape or image intensity over time, relate preoperative images and surgical planned outcomes [102] with the physical world during interventions and align patients with standardized atlas [103].

The aim of image registration techniques is to find the optimal transformation that best aligns the structures of interest in the input images. For this, the techniques establish the spatial correspondence among features in the images or minimize an error measure, or of a cost function. Additionally, optimization algorithms are usually needed to find the most suitable geometrical transformations and interpolators are employed to resample the images into the registered space.

Applications of image registration techniques in nuclear medicine include correlative image interpretation, attenuation correction, scatter correction, correction for limited resolution and improvement of the reconstruction accuracy in emission tomography. These techniques have also been used in the co-registration of functional studies, for the transformation of the images to standard spaces for their comparison against both normal cases and data from other modalities, in conformal radiotherapy treatment planning and in functionally guided procedures. Besides, such methods have been used to improve the interpretation of several functional studies based on static images, including brain, breast, chest, liver, kidneys and colon images, or to assist motion analysis as in cardiac and lung studies.

There have been previous reviews concerning medical image registration in general [73, 104–109], medical image classification [110], mutual-information-based registration methods [106], unsupervised registration methods [111], non-rigid image registration [112, 113], image registration for nuclear medicine images [100], image registration techniques for specific organs as breast [114], brain [115, 116] and cardiac images [117].

In this chapter, registration methods classification from several authors is reviewed. Then, techniques of image registration in general are described, namely geometric transforms, similarity measures, optimizers and interpolators. Finally, the main nuclear medicine images applications are referred.

3.1. Registration methods: classification

Depending on the authors, different image registration techniques classification criteria can be found in scientific literature. Image registration methods were classified into four categories: point methods, edge methods, moment methods and “similarity criterion optimization” methods [118]. On the other hand, it was proposed a classification based on: data dimensionality, origin of image properties, domain of the transformation, elasticity of the transformations, tightness of property coupling, parameter determination and type of interaction (interactive, semi-automatic and automatic) [110]. Still, registration techniques were divided into: stereotactic frame systems, point methods, curve and surface methods, moment and principal axes methods, correlation methods, interactive methods, and atlas methods [118].

The registration methods can also be classified according to the subjects and the image modalities involved. Hence, intra-subject and intra-modality applications refers to the image registration of the same subject in images acquired using the same imaging modality. Intra-subject and inter-modality registration concerns the image registration between images of the same subject but acquired using different imaging modalities, which is a common case that involves PET and SPECT images [119]. Inter-subject and intra-modality registration consists of aligning images of different subjects but acquired by the same imaging modality. Finally, inter-subject and inter-modality is related to the alignment of images from different subjects and acquired by different imaging modalities.

Table 3.1 depicts the classification of medical image registration methods [104], which takes into account data dimensionality, nature of the registration basis, both nature and domain of the transformation, type of interaction, optimization procedure, imaging modalities, subject and object involved.

Registration techniques based on voxel intensity are known as intensity based, while those based on the geometrical structures extracted from the images as feature or geometrical based. Furthermore, frequency or Fourier based registration techniques uses the image in the frequency domain or its Fourier transform properties. Feature space information or techniques based on the amount of image information are another classification proposed in literature [73].

3.2. Image registration techniques

Image registration techniques aim to find the optimal transformation that best aligns the structures of interest in the input images [120–122]. After the attribution of a common coordinate system, the images are transformed into this system. Therefore, registration techniques are based into geometric approaches, also known as feature-based methods, and intensity approaches. Feature-based methods start by establishing the correspondence between features in the input images and then compute the geometrical transformation that aligns these features. Intensity-based methods iteratively adjust the transformation that aligns the input images taking into account the image pixels intensity or voxels, through the minimization of a cost function. Usually, the cost function used consists of the similarity measure, i.e., the registration algorithms try to minimize an error measure [123]. Additionally, algorithms are needed to find the most suitable geometrical

Table 3.1 Classification of medical image registration methods (adapted from [73]).

Classification Criteria	Subdivision	
Dimensionality	Spatial dimension: 2D/2D, 2D/3D, 3D/3D	
	Temporal series	
Nature of the registration basis	Extrinsic	
	Invasive	Stereotactic frame
		Fiducial (screw markers)
	Non-invasive	Mould, frame, dental adapter, etc.
		Fiducials (skin markers)
	Intrinsic	
	Landmark based	Anatomical
		Geometrical
	Segmentation based	Rigid models (points, curves, surfaces, volumes)
		Deformable models (snakes, nets)
	Voxel property based	Reduction to scalar/vectors (moments, principal axes)
		Using full image content
	Non-image based (calibrated coordinate systems)	
Nature of transformation	Rigid (only rotation and translation)	
	Affine (translation, rotation, scaling and shearing)	
	Projective	
	Curved	
Domain of transformation	Local	
	Global	
Interaction	Interactive	Initialization supplied
		No initialization supplied
	Semi-automatic	User initializing
		User steering/correcting
		Both
	Automatic	
Optimization procedure	Parameters computed directly	
	Parameters searched (the transformation parameters are computed iteratively using optimization algorithms)	
Imaging modalities involved	Monomodal	
	Multimodal	
	Modality to model (register the coordinate system of the imaging equipment with a model coordinate system)	
	Patient to modality (register the patient with the coordinate system of the imaging equipment)	
Subject	Intra-subject	
	Inter-subject	
	Atlas	
Object	Head (brain, eye, dental, etc.)	
	Thorax (entire, cardiac, breast, etc.)	
	Abdomen (general, kidney, liver, etc.)	
	Limbs	
	Pelvis and perineum	
	Spine and vertebrae	

transformation, and interpolators are employed to resample the image data into the new common space.

Landmarks-based registration methods are based on the identification of the correspondence between landmarks, e.g. points, in the two input images which are small natural or artificial features. It involves identifying the corresponding landmarks between the images. These markers can be distinguished as extrinsic, anatomical and geometrical landmarks. External point landmarks must be visible and are well suited to validation studies. However, their routine application is impracticable, since patient studies may be realized on different days and the markers location must not vary in the same study. On the other hand, internal anatomical landmarks do not need marker preparation, but it is difficult to obtain a reliable and accurate localization, as well as presents a poor resolution. Then, they are not used in nuclear medicine, only to access validation of registration methods. Geometrical landmarks consist of corners and other geometric features that can be identified automatically, but also presents low resolution and low signal-to-noise levels in nuclear medicine images [100]. These problems can be partially overwhelmed using image registration algorithms based on different combinations of landmark-, surface-, attenuation- and intensity-based registration methods [124, 125].

Boundaries or surfaces are more distinct in medical images than the usual landmarks, leading to surface-based registration methods. It consists on the establishment of correspondence between boundaries or surfaces that are defined in the input images, presenting good results for inter-modality registration, where both images can have very different pixel or voxel values [100]. There are three approaches for representing a surface registration, namely feature, point and model-based methods. Although, the criteria for selecting one of these approaches is application-specific, as well as the size of the transformation to be computed [126].

Feature-based methods enable building explicit models of identifiable anatomical elements in each image as surfaces, curves and point landmarks, which can be aligned with their counterparts in the second image. The use of feature-based methods is recommended to images that contain enough distinctive and easily detectable features [15]. Figure 3.1 illustrates a typical feature-based registration algorithm. Hybrid registration using combined surface and volumetric-based registration methods enable the extraction of relevant geometrical information from

surface-based morph and its following diffusion into the volume [127]. Surface alignment has been employed for image-guided surgery [128].

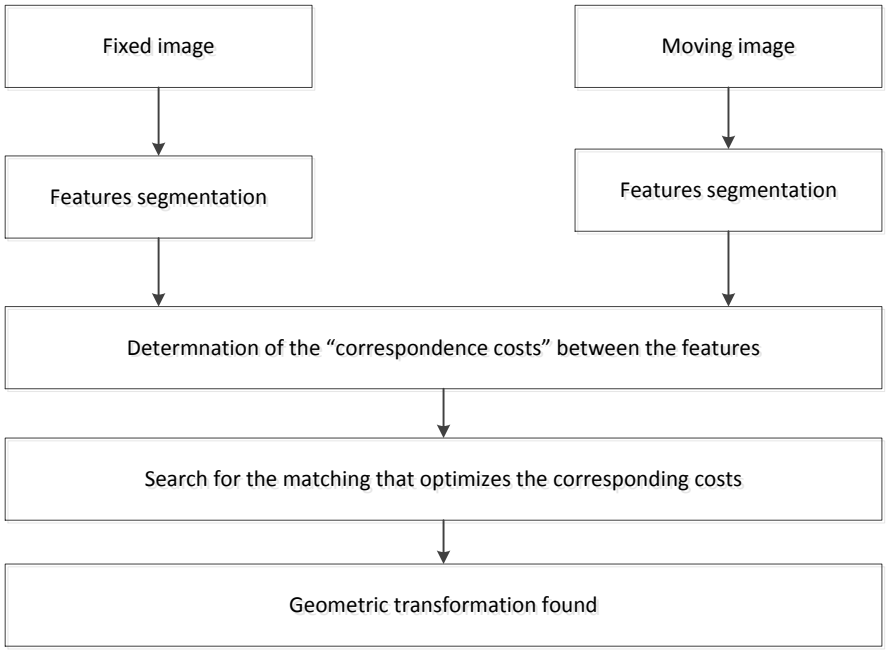

Figure 3.1. Diagram of a typical feature-based registration algorithm [73].

On the other hand, intensity based registration techniques align intensity patterns using mathematical or statistical criteria over the whole image, but do not consider anatomical information. Combining geometric features and intensity features in registration should result in more robust methods. Therefore, hybrid algorithms involving intensity-based and model-based criteria allows the establishment of more accurate correspondences [112]. Figure 3.2 presents the general framework of the registration methods based on the minimization of a cost function. Image registration algorithms using the intensities of the pixels in the two input images [129], without any requirement to segment or delineate the corresponding structures, such as voxel similarity-based registration, result in robust and accurate computations [130]. These methods tend to average the error caused by noise or random fluctuations.

Image pre-processing is generally used to ensure that a sensible solution is obtained, since it provides a better definition of object boundaries and volumes, as well as enables intensity mapping to modify the range of intensities that are used in

the matching algorithms. However, it is fundamental pre-processing algorithms not to be excessive and time-consuming [100].

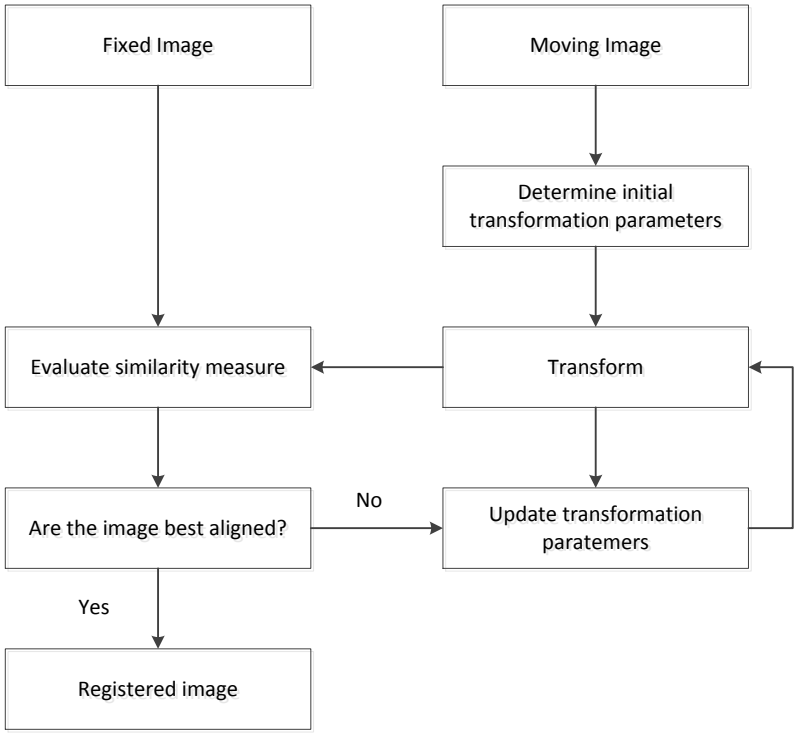

Figure 3.2. General scheme of the image registration methods based on the optimization of a cost function (adapted from [100]).

Rigid and affine registration can be determined in seconds. Contrarily, most non-rigid registration can take minutes or hours [112]. It is therefore commonly recommended to improve the speed of image registration techniques. It is common to employ coarse-to-fine methods, providing both faster initial estimates and gradually finer details. Another solution to reduce image registration time-consuming consists of sub-sample the image volume, involving spatial domain or histogram intensity values, to increase the sampling as the algorithm gets closer to the final solution [100].

3.2.1. Geometric transformations

The goal of image registration algorithms is to find the transform involved between the input datasets by means of geometrical transformations, whose number of parameters varies with the complexity of the transformation. The selection of the appropriate geometrical transformation model is crucial to the success of the registration process.

The geometrical transformation model can lead to rigid or non-rigid registrations. The simplest geometrical transformation model is based on a rigid transform that considers rotations and translations, which is applied to the complete data set. Affine transform models include translations, rotations, scaling and shearing in order that the straight lines of an image are transformed to straight lines in the other image, and the parallel lines are preserved parallel [105]. The most complex transformation model implies a higher number of degrees of freedom resulting in a non-rigid transformation. Fig. 3.3 illustrates these geometrical transformations.

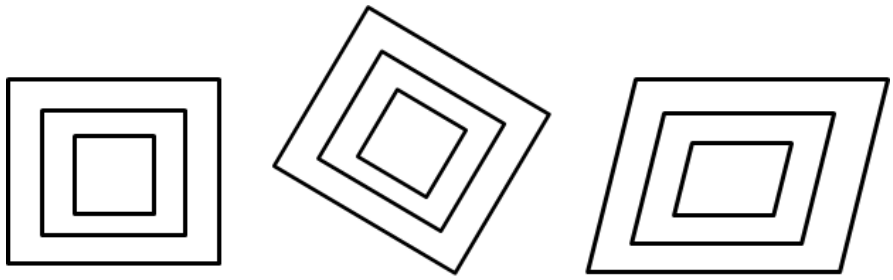

Figure 3.3. Types of geometrical transformations: identity transformation (left); rigid transformation (center) and affine transformation (right) (adapted from [100]).

Image registration algorithms based on non-rigid transformations are required, for example, when it is needed to establish the correspondence between images of one individual and an atlas [131] or computer models, and to accommodate the substantial anatomical variability across individuals [112, 113, 132, 133]. Non-rigid based registration algorithms have a higher number of degrees of freedom, when compared with rigid transformations [134, 135]. They are frequently used in image registration when the image acquisition parameters are not known [136] and usually include an initial rigid body or affine transformation that provides an initial solution for the transformation. A good pre-registration method is recommended to obtain a starting position and orientation closer to the optima non-rigid image registration solution. However, a higher number of parameters in the transformation model can introduce undesirable transformations. Then it is fundamental taking into account a regularization term [137–139]. Image registration using non-rigid transformation can be achieved using basis functions as a set of Fourier [140–143] or Wavelet basis functions [144].

Registration using splines consists of techniques based on the assumption that a set of control points maps their location in the target image into its corresponding counterpart in the source image, providing a smoothly varying displacement field

between the landmarks used. Therefore, spline-based geometrical transformations either interpolate or approximate the displacements at control points. Thin-plate splines (TPS) are based on radial basis functions and used in surface interpolation of scattered data [132, 133]. Each basis function contributes to the transformation, and each control point has a global influence on the transformation. The modeling of local deformations can be more difficult with these functions, which requires the use of free-form transformations based on locally controlled functions [145, 146]. B-splines deform an object through the manipulation of an underlying mesh of control points generating a smooth continuous transformation. Thin-Plate Spline Robust Point Matching (TPS-RPM) algorithms has been used for non-rigid registration, showing robustness when aligning models in presence of a large amount of outliers [47].

Elastic, deformable or curved registration methods enable modeling the deformation and resampling the stretch of an elastic material, through specific transforms. Their limitations are due to the highly localized deformations that cannot be modeled due to the deformation energy from stress. There are reviews of the most promising non-linear registration strategies currently used in medical imaging, as a novel curvature based registration technique that permits a faster image registration [149], the application of deformable registration in an automated hexahedral meshing of anatomical structures [150, 151], symmetric non-rigid registration [152] and Brownian Warps, a diffeomorphism registration algorithm [153]. Fluid registration and registration using optical flow are approaches that are equivalent to the equation of motion for incompressible flow.

3.2.2. Similarity measures

The characteristics of the image modalities and the nature of the misregistration must be taken into account to choose the similarity measure, as well as the type of registration, i.e. intra- or inter-modality.

Similarity measures can be classified into landmark, feature or intensity based metrics. Depending on the features used, some similarity metrics can be included in both classes. The similarity measure used for deformable image registration is composed of one term related to the pixel or voxel intensity or the matching between the structures in the images, and another one related to the deformation. Then, the cost function built is a trade-off between the pixel, or voxel,

intensity or matching between the structures and the constraints imposed on the deformation field.

Respecting landmarks measures, the similarity measure commonly employed consists of representing the average distance between the corresponding landmarks. Similarly, surfaces or edges measures quantifies an average distance between the corresponding surfaces, or between a surface extracted in one image and its corresponding set of points in the other image [109].

The simplest similarity measure compare intensity values between images directly [100]. To register intra-subject and intra-modality images, the correlation coefficient (CC) has been an adequate similarity measure, since it involves the multiplication of the corresponding image intensities assuming a linear relationship between the intensity values. It is possible to subtract the corresponding image intensities instead of multiply them [154], allowing the adjustment of the alignment by the sum of absolute differences (SAD), as exemplified in Figure 3.4 or the smallest sum of squared intensity differences (SSD) [155]. The SSD is very sensitive to a small number of voxels that have very large intensity differences between the images to be registered.

Ratio image uniformity (RIU) and variance of intensity ratios (VIR) work from a derived ratio image and are quantified as the normalized standard deviation of the voxels in the ratio image. These similarity measures are employed for intra-modality registration. Partitioned intensity uniformity (PIU) seeks to maximize the uniformity by minimizing the normalized standard deviation. It is usually used to register inter-modalities images [105].

Recent image registration algorithms have been demonstrating applicable techniques based on information theory to both inter- and intra-modality registration. Image registration can be described as trying to maximize the amount of shared information in two images, which means that information can be used as a registration metric [156]. The joint entropy measures the amount of information existing in combined images. It has been used for rigid and non-rigid image registration [49, 50]. Mutual information can be given by the difference between the sum of entropies of the individual images at overlap and the joint entropy of the combined images [157]. Hence, it is the measure of how one image explains the other. It makes no assumptions about the functional form or relationship between image intensities [157–161].

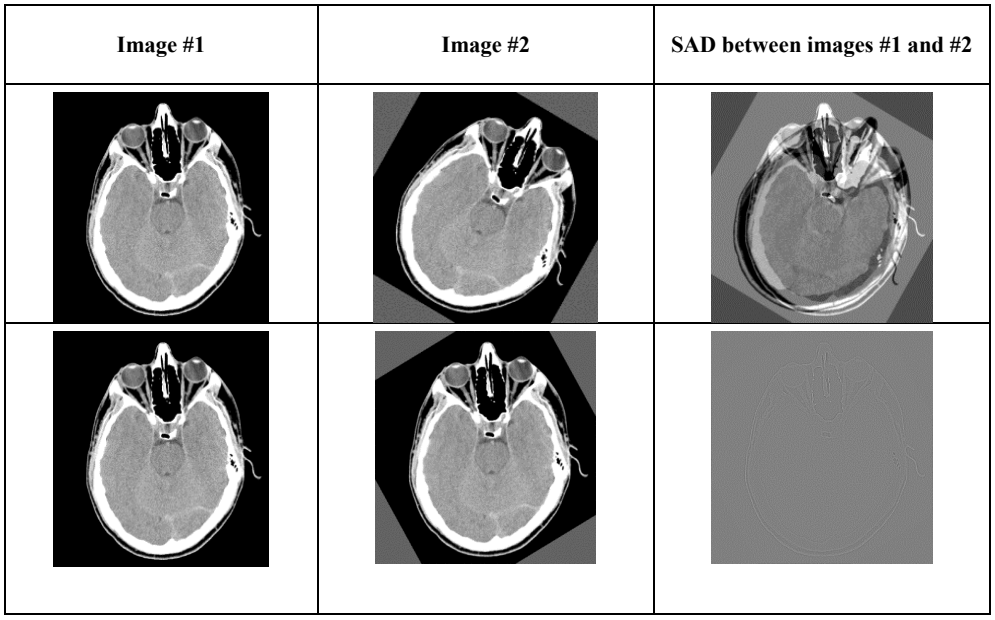

Figure 3.4. Application of the sum of absolute differences (SAD) to stress the differences between two images, before registration (up) and after registration (down). Before registration, or poor aligned images, the images give rise to large absolute differences, while the sum of absolute differences of well aligned images results in small differences.

Changes in overlap of very low intensity regions, such as due to noise, can disproportionally contribute to artifacts that affect the registration accuracy when based on mutual information, so it is commonly used associated with normalization methods [160, 161].

3.2.3. Optimization

All the registration algorithms require an iterative approach, whose initial estimation of the transformation is gradually refined by trial and error, to calculate the similarity measure value at each iteration. So, the optimization process consists of both estimating the transformation and evaluating the similarity measure till the algorithm converges to a point when no transformation can be found with better similarity measure value [105]. Hence, the optimization algorithm computes the value of the cost function or of the similarity measure employed to relate the matching of two registered images, searching for the subsequent alignment transformations that will stop when an optimal value is achieved. It is done by searching the transformation that increase or decrease the cost function until a maximum or minimum is found, depending on the type of the cost function used.

The optimization process is based on the fact that the quality of the matching of two images is balanced against some constraint. This constraint has the function of prohibiting implausible deformations and may be provided by some estimate of the energy required to physically induce the deformation [161].

One of the major difficulties is that the optimization algorithms can converge to an incorrect local optimum, because multiple optima can exist in the parameters space [162–164]. The erroneous optima can be due to interpolation artifact or local good matches between features or intensities and can be avoided by smoothing the original images. The starting position must be sufficiently close to the final position for the algorithm converge at the best answer, within its capture range [161]. To choose the solution that has the best function cost value, a multi-start optimization can be used to get the global optimal solution [61, 62]. Additionally, the images are initially registered at low resolution and then the transformation obtained is used as starting transformation in registration at the next higher resolution level [165, 166].

3.2.4. Interpolation

A process of interpolation is applied when it is intended to transform an image space into the space of another image. It is required to estimate the values of the transformed image [100]. Thus, its goal is to estimate the intensity at the new position [73] and depends on the motivation for registering the images. The accuracy and speed of the registration process can be improved through the use of suitable interpolation solutions.

Nearest neighbor, linear interpolation or trilinear interpolation are the simplest interpolation methods, and consist of curve fitting using linear polynomials. Any other interpolation method beyond the nearest neighbor interpolation is required to guarantee accuracy. However, the resultant image will be smoother than the original. When the interpolation complexity increases, according the number of polynomial variables augments, smoothing effects can accumulate, or even generate artifacts [100]. Recent interpolation methods between neighboring slices in grey-scale are based on B-splines [167], geometric multi-grid [168], using a modified control grid interpolation algorithm [169] or adaptive 2D autoregressive modeling and soft-decision estimation [170].

The interpolation error can introduce modulations in the similarity measure, since transformations involve pure translations of datasets with equal sampling spacing, and the period of the modulation is the same as the sampling spacing. Thus, interpolation methods must be used with practicable computational costs, firstly using a low cost interpolation as trilinear or nearest neighbor. It is a good practice to employ a more expensive interpolation in the last few iterations or even take advantage of the spatial-frequency dependence of the interpolation error, such as cubic B-splines or windowed sinc interpolators. It must be taken into account the level of smoothness and robustness of the similarity measure against artifacts, which may require a more robust interpolation solution to be used successfully in the optimization step.

3.3. Accuracy Assessments and Validation

Image registration methods must be validated, especially in medical applications, through a verification process based on the comparison of results obtained against a gold standard. Accuracy assessment and validation imply a very low failure rate and high accuracy, through the knowledge of a ground truth registration [171].

The target feature is any object that can be localized independently of the view. The disparity in the two corresponding positions of the target feature after registration provides an upper bound on the root mean square (RMS) of target registration error (TRE) [172]. This measure of error is recommended to be used as the quantity of choice to be reported in the validation process. It can be expected to vary with the registration problem, since it comprises different image modalities, anatomical structures and pathologies, and distinct positions within a view [161].

Several fiducial features can be employed as registration cues as a more desirable method for rigid-body registration, constituting a validation standard. It can be determined without referring other standard validations and is accomplished through the exploitation of establishing statistical relationships among fiducial localization error (FLE) and TRE [173] to translate self-consistency into accuracy [161].

The software industry has already developed standards, protocols and quality procedures [174]. Validation usually follows a sequence of measurements using

computer-generated models, known as software generated phantoms [175] and images of patients or volunteers against with the registration algorithms must demonstrate competence. Experimental validation of an image registration system must be extended to a clinical situation [176]. Visual assessment is also used as a standard and recently subjected to validation. Based on registration circuits, a self-consistency method [161] is considered where a set of three or more images are registered in pairs.

Registration validation methods have been concentrating more efforts for rigid registration than for non-rigid registration [161]. Their improvements are fundamental so novel registration models can be accepted as a clinical tool, which is not possible without a means of validation method.

3.4. Image registration software packages

Several registration methodologies have been developed [109], particularly for multimodality, cardiac and brain images registration, but also in whole-body oncological applications [177], which are commercialized with the nuclear imaging equipment or developed under their respective software, as Hermes Medical Solutions, GE Healthcare, Philips and Siemens, in a single unit depending on the specific clinical needs. The state-of-the-art of user friendly software oriented to medical image processing, segmentation and registration, respecting to the registration methods, rigid and non-rigid transformation as well as their main applications, optimization and interpolation algorithms is yet reduced, being the majority of the existing software directed to developers.

A system for PET–MRI registration capable of automatic scalp/brain segmentation replacing manual drawing operations and a fast and accurate image registration method is embedded in a commercially available scientific visualization package [178]. A parallel implementation uses *a priori* information about the nature of imaged objects to adapt the regularization of the deformations, giving higher weight to those points in images that contain more information. Its usability was improved through the implementation of a grid service that can be controlled by a graphics workstation embedded in the clinical environment [138]. The Functional Image Registration (FIRE) is an operating system and platform for independent multimodal image registration software, where several automatic algorithms were implemented, including principal axes matching and maximization of the mutual

information methods; a user interface was designed to support image manual registration [174].

Insight Toolkit (ITK) is an object-oriented software system, implemented in C++, for image processing, segmentation and registration. It is an open-source software used to academic research, once it is designed to be intuitive and easy to learn through a basic object-oriented and implementation methodology, although being a large and complex system, by exploring the examples available within the source directory. This cross-platform system provides developers an extensive suite of software tools for image analysis to employ leading-edge algorithms for registering and segmenting multidimensional data [179].

There are various registration software packages related with this toolbox. A well-known software based on ITK is Elastix [180]. It registers any type of images, but is frequently used to medical image registration. Supporting many transform models, similarity measures, optimization methods, interpolation methods, and multi-resolution schemes, it facilitates the construction of own user registration methods since their components can easily be plugged in. Advance Normalization Tools (ANTs) also depends on the ITK and extracts information from complex datasets that include imaging, being useful for managing, interpreting and visualizing multidimensional data. It has been considered an emerging tool supporting standardized multimodality image analysis [181]. A software developed in Objective-C oriented to MacOS called OsiriX provides multidimensional image navigation and image display to interpretation of large sets of multidimensional and multimodality images [182]. The image processing and visualization tools VTK, also based on ITK, have graphic capabilities provided by Open Graphics Library (OpenGL) graphic standard. It is thought to simplify the navigation through large datasets, such as to do complex and specific tasks [182].

NiftyReg belongs to the NifTK platform, developed at University College of London, and is capable of perform rigid, affine and non-linear registration of nifty or analyze images. Specifically oriented to groupwise and longitudinal registration, Groupwise and Longitudinal Image Registration Toolbox (GLIRT) is useful for unbiased analysis of a large set of MRI brain images, including improved unbiased groupwise registration guided with the sharp group-mean image, and hierarchical feature-based groupwise registration with implicit template.

3D-Doctor supports greyscale and color MRI, CT and PET images in several formats and provides segmenting tools, 3D modeling export, measurements and quantitative analysis, 3D advanced processing tools. Through registration and fusion tools, the end-user can visualize re-sliced images automatically or semi-automatically using a user-defined axis.

Automated Image Registration (AIR) is a library that allows automated intra and inter-subject registration of 2D and 3D images, such as mono and multimodality registration.

Frequently used on academic research, Matlab Image Registration Toolkit (MIRT) is a software package for 2D and 3D non-rigid image registration, supporting mutual information (MI), residual complexity (RC), sum of squared differences (SSD), sum of absolute differences (SAD) and correlation coefficient (CC) as similarity measures, as well as parametric and non-parametric transformation models, namely free form deformation (FFD) and curvature regularization. To the optimization step, it presents implicit Euler method (gradient-based) and regulates with penalized Laplacian of the displacements both for parametric and non-parametric transformation models. Multi-resolution and groupwise registration is possible. However, compared with ITK, Matlab is heavier so the application will have a higher processing time.

Amide is a Medical Image Data Examiner (AMIDE) that has been developed to be user-friendly to display and analyze multimodality volumetric medical images. It enables the user to freely shift, rotate, view, and analyzes data sets while the program automatically handles the interpolation needed. It is compatible with UNIX, Macintosh OS X and Microsoft Windows platforms [183].

Based on Matlab, Statistical Parametric Mapping (SPM) is a software package designed for the analysis of brain imaging data sequences as series of images from different cohorts or time-series from the same subject [184]. It enables the construction and assessment of spatially extended statistical processes, used to test hypotheses about functional imaging data. However, this software has lost its popularity to BioImageSuite [185]. This software has extensive capabilities for cardiac, abdominal and neuro-imaging analysis providing functionality for image visualization and registration, surface editing, cardiac 4D multi-slice editing, diffusion tensor image processing and mouse segmentation and registration. Moreover, it can be integrated with other biomedical image processing software.

3.4.1. Registration methods available in ITK

The ITK registration framework is based on a data flow via pipeline, where each component applies a specific operation at the inputs, being its outputs equally treated by another element, consisting of a sequence of pointers with specific attributes that are linked each other to perform various operations on a dataset.

Table 2.2. Available registration functions in ITK-4.3, relevant for this report understanding [179].

Funtion	Class	Description
Transform	B-Spline	Uses as template parameters the type for coordinates representation, the dimension of the space, and the order of the B-spline.
Transform	Versor Rigid 3D	Implements a rigid transformation in 3D space, exposing six parameters, three for the versor components and three for the translational components. The center coordinates are not modified during the optimization performed in a registration process.
Transform	Affine	Represents an affine transform composed of rotation, scaling, shearing and translation. The transform is specified by a N × N matrix and a N ×1 vector where N is the space dimension. Only defined when the input and output space have the same dimension.
Metric	Mattes Mutual Information	The marginal and joint probability density function (PDF) is evaluated at discrete positions or bins uniformly spread within the dynamic range of the images. Entropy values are then computed by summing over the bins.
Interpolation	B-Spline	Represents the image intensity using B-spline basis functions. When an input image is first connected to the interpolator, B-spline coefficients are computed using recursive filtering (assuming mirror boundary conditions). Intensity at a non-grid position is computed by multiplying the B-spline coefficients with shifted B-spline kernels within a small support region of the requested position.
Interpolation	Linear	Assumes that intensity varies linearly between grid positions. Unlike nearest neighbor interpolation, the interpolated intensity is spatially continuous. However, the intensity gradient will be discontinuous at grid positions.
Optimizer	LBFGS	Limited memory Broyden, Fletcher, Goldfarb and Shannon minimization.
Optimizer	Regular Step Gradient Descent	Advances parameters in the direction of the gradient where a bipartition scheme is used to compute the step size.
Optimizer	Versor Rigid 3D Transform Optimizer	Specialized version of the regular step gradient descent optimizer for versor rigid 3D transform parameters, where the current rotation is composed with the gradient rotation to produce the new rotation versor. The translational part of the transform parameters are updated as usually done in a vector space.

It has: (1) a fixed image and a moving image as input data, (2) a transform component that represents the spatial mapping of points from the fixed image space to points to points in the moving image space, (3) a metric component that provides a measure of how well the fixed image is matched by the transformed moving image, comparing the intensity values in the fixed image against the correspondent in the moving image, (4) an interpolator used to evaluate the moving image intensities at non-grid positions, (5) and an optimization method, used to optimize the metric value relative to the defined space by the transform parameters, which means that it finds the maximum or minimum value, depending on the similarity criterion indicating the transformation that better corresponds to the involve images.

ITK provides a variety of transforms from translations, rotations and scaling to general affine and kernel transforms, using `itk::Transforms` to encapsulate the mapping of points and vectors from an input space to an output space.

3.5. Registration in Nuclear Medical Imaging

Nuclear image modalities provide a physiological diagnose through the use of radiotracers to map the metabolism and fluid flow on tissues or organs [186]. Nuclear medicine benefits from such evolving integration and image registration plays a central role in this integration [25, 29, 32, 50].

In oncology, the completion of the medical Positron Emission Tomography (PET) examination, most of the times hybrid Positron Emission Tomography/Computed Tomography (PET/CT) [76, 187] enables the detection of tumors at early stages, since it is capable of detecting the development state of cancer and, subsequently, a proper choice to carry out the treatment and the evaluation of the therapeutic response.

In cardiology, several studies have been developed, particularly in the study of chronic ischemia [119, 188–191], myocardial perfusion [10, 37, 80, 88, 92, 95, 120, 121, 179, 194–198], atherosclerosis rate [191, 198], post-transplantation [197] and cardiac nervous system. Registration of cardiac images is a more complex task than the registration of images of static organs, since it is a non-rigid moving organ inside a moving body, and exhibits few accurate landmarks [117]. Non-rigid registration is a key requirement for the application of cardiac function biomechanical models, through the creation of a generic cardiac model that is instantiated by linear elastic registration with cardiac images of a subject acquired in different modalities [112].

As regards the neurological and psychiatric disorders, molecular imaging has the ability to reveal no detectable lesions by other imaging methods [199] and provides information on the physiological and biochemical properties and subsequent functional integrity determination of brain damage's adjacent regions [200]. The pre-surgical evaluation of epilepsy [100, 156], guided biopsy in brain tumors [201], evaluation of primary brain tumors, dementia diagnosis and selection of stroke patients for surgical treatment [200] are the main nuclear medicine clinical cases. They also allows the study of Parkinson's disease [191, 200], Alzheimer [70, 72], and movement disorders [202]. Monitoring changes in the individual by acquiring series of imaging scans is a common practice since it is particularly useful in dementia where fluid registration is a cue to visualize patterns of regional atrophies [112].

A generic application of non-rigid registration is the segmentation or labeling task [112]. It achieves good correspondences between structurally equivalent regions in two images. Fully automatic multimodality image registration algorithms, namely CT-PET, MR-CT, MR-PET and MR-SPECT registrations, requiring no user interaction, are already available [203] through the detection of the head contour on MR or CT images using a gradient threshold method, followed by segmentation into a set of connected components [204].

3.6. Conclusions

Most current algorithms for medical image registration use rigid body transformations or affine transformations, but they are restricted to parts of the body where tissue deformation is small compared with the desired registration accuracy. Algorithms based on optimizing a similarity measure and information theory based can be applied automatically to a variety of imaging modality combinations without the need of pre-segmenting the images and can be extended to non-affine transformations. However, it is recommended to pre-register the input images with an image registration technique based on rigid transformation and then finalize the process using another image registration technique based on deformable transformations.

Inter-modality registration is still unusual in the clinical environment, but this kind of image registration is being widely used in medical research, especially in neurosciences, where it is used in functional studies, in cohort studies and to quantify changes in structures during ageing and diseases development. However, its

clinical use has logistical difficulties due to the need of acquire and register a large number of images in a reduced time interval, requiring advanced computational infrastructures, as well as production of multimedia electronic records.

Due to the functional diagnosis that molecular imaging provides, SPECT and PET image registration computer techniques applications in clinical diagnosis, assessment of response to treatment and delivery of targeted therapies are actually being exploited. Image registration has potential to aid the medical diagnosis, surgery and therapy. Some examples are the combination of functional and high anatomical information. It contributes to a better localization and determination of abnormalities, the planning of their treatment and surgeries. Besides, differences are directly quantified, providing a more objective evidence of the intervention effects or response to therapy in serial studies.

Chapter 4

Image processing, segmentation and quantitative analysis

Human perception is highly based on pictorial information through the sense of vision. Imaging is present in a great number of technical applications, through the entire electromagnetic spectrum: imaging based on gamma-ray and radio band are used in nuclear medicine and astronomical observations; x-ray imaging enables medical diagnosis and industry applications; ultraviolet band imaging is applied in lithography, industrial inspection, microscopy and biological imaging. Other imaging modalities are applied in geological and marine exploration through ultrasound systems, as well as transmission electron microscopes explores the world at micro- and nano-scale, without forget the applications based on visible and infrared bands imaging.

Hereafter, digital image processing methods are fundamental to improve pictorial information for human interpretation and enable storage, transmission and representation of image data for autonomous machine perception.

At this chapter, it is pretended to expose an overview of the components contained in a typical image processing systems, focusing on segmentation and quantitative image analysis techniques used in the experimental implementation of this dissertation, such as the image classification methods employed.

4.1. General Principles of Digital Image

An image consists of a two-dimensional function $f(x,y)$, where x and y are spatial coordinates and f represents the amplitude of any pair of coordinates, i.e., the intensity of the image at that point. It is a positive scalar quantity whose physical meaning is determined by the source of the image; it is proportional to the energy radiated by the physical source. A digital image is a set of finite number of elements called picture elements, image elements or pixels, generated from a physical process.

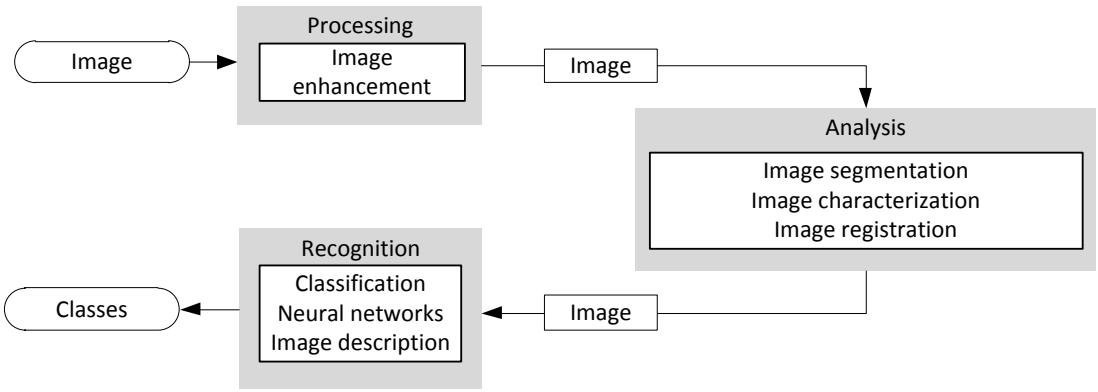

Figure 4.1. Digital image general framework.

The fundamentals steps in digital image processing are present in Figure 4.1. It is started by image acquisition, which generally involves image pre-processing techniques, to overcome the noise inherent to acquisition systems. Image enhancement and restoration enable the image manipulation through specific methods that are image oriented. The main objective at this step is to obtain images more suitable than the originals for the pretended purpose.

Note that enhancement is subjective, regarding the human preferences of a good enhancement result, and restoration is objective, since it is based on mathematical or probabilistic models of image degradation. Color image processing, image representation based on wavelets and compression are also part of the image processing system. Morphological processing consists of tools that enable the extraction of image components to represent and describe shapes and has an important role in segmentation.

Segmentation methods are one of the most difficult tasks in digital image processing, since the successful solution requires the correct identification of the objects or regions of interest. Segmentation results are then used as entry to

representation and description, which can be boundary or region-based depending on the features or image attributes that are intended to be extracted.

The assignment of an object's labels based on its descriptors constitutes the process of recognition. Using pattern recognition algorithms, it is possible to determine classes through classification or neural networks and classify images under study as belonging to a given class [205].

4.2. Image processing

4.2.1. Image intensity normalization

Spatial resolution is defined as the measure of the smallest discernible detail in an image, consisting of the number of pixels per unit distance. On the other hand, intensity resolution represents the smallest discernible change in the intensity level. The number of bits is used to quantize intensity resolution into intensity levels, for instance 256 levels has 8 bits of intensity resolution. The most commonly used is 8, 10, 12 or 16 bits.

Image intensity normalization is the process that changes the range of pixel intensity values, also known as contrast-stretching transformation function or dynamic range expansion. Frequently, it is used to achieve consistency in dynamic range for a set of data. Similarly, it permits to expand a narrow range of input levels into a wide range of output levels, resulting in an image of higher contrast, as illustrated in Fig. 4.2.

(a) 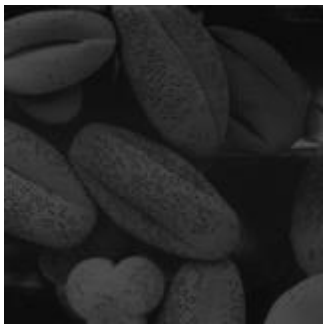 (b)

Figure 4.2. Image intensity normalization of (a) identity image results in (b) higher contrast image [206].

Considering a n-dimensional input gray-scale image $f(x,y)$, and the output normalized image $g(x,y)$, the linear normalization of a grayscale digital image is

performed according to the equation 4.1. Non-linear image intensity normalization is employed when the pretended intensity normalization function is a non-linear equation [206].

$$g(x,y)=\frac{max\{g(x,y)\}-min\{(g(x,y)\}}{max\{f(x,y)\}-min\{f(x,y)\}}\ (f(x,y)-min\{f(x,y)\})\ +\ min\{g(x,y)\} \qquad (4.1)$$

4.2.2. Image resampling

It is possible to enlarge an image as it is pretended. It is needed to create the grid with the intended size. If the pixel spacing defined is the same as the original, then the shrunken image fits exactly over the original image. Note that the pixel spacing in the shrunken grid will be less than the pixel spacing in the original image. Image interpolation is used to assign point intensities in the overlay grid [207].

4.2.3. Image interpolation

Tasks as zooming, shrink, rotating and perform geometric corrections uses image interpolation as basic tool. It is the process of using known data to estimate values at unknown locations [208].

The nearest neighbor interpolation consists of assigning to each new location the intensity of its nearest neighbor in the original image. Still a simple process, it introduces undesirable artifacts, such as distortion of edges. To overcome this problem, more suitable approaches are employed. They are bilinear and bi-cubic interpolation, which uses four and sixteen nearest neighbors, respectively, to estimate the intensity of a given location. Bi-cubic interpolation allows a better preservation of fine details, besides the higher processing time, which is justifiable for medical image processing.

(a) (b)

Figure 4.3. Image interpolation results: (a) application of nearest neighbor interpolation and (b) using bilinear interpolation [206].

Figure 4.3. presents images that were zoomed from 128 x 128 to 1024 x 1024 pixels using nearest neighbor interpolation and using bilinear interpolation, which clearly shows better improvements for bilinear interpolation technique.

More complex interpolation techniques, such as splines and wavelets can be used to obtain better results [209]. A B-spline interpolation consists of a basis spline function that has minimal support with respect to a given degree, smoothness and domain partition, i.e., any spline function of a given degree can be expressed as a linear combination of B-splines of that degree. Spline interpolation is preferred over polynomial interpolation since its error can be less if using a low degree. Moreover, it avoids the problem of Runge's phenomenon, consisting of oscillation at the edges on an interval that occurs when using polynomial interpolation of high degree [207].

4.2.4. Image averaging

Nuclear medicine images can contain noise, deterioration factors, spatial resolution and image reconstruction techniques, as well as they are dependent on the behavior of the patient respecting the clinical protocol.

(a) 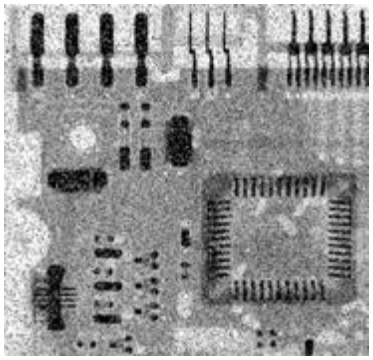 (b) 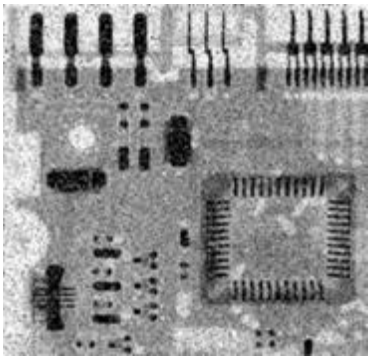

Figure 4.4. Noise reduction of (a) X-ray image of circuit board corrupted by salt-and-pepper noise, using a 3 x 3 averaging mask, resulting in image (b) [206].

Therefore, it is fundamental to reduce the noise content. Smoothing filters are usually employed, which masks yields the standard average of the pixels under the mask. A $m\,x\,n$ mask would have a normalizing constant equal to $1/mn$. If all coefficients are equal, the averaging mask is also called a box filter [175]. An example of its application is shown in Figure 4.4.

4.2.5. Morphological Image Processing

Object shape description and its structure properties are defined as morphology. Mathematical morphology is used to extract image properties. Its methods are used for image processing, namely morphological filtering, thickening or thinning [179].

Morphological operations require, as input data, both the processed image and a structural element, whose shape and dimension is arbitrary and can be represented as a binary image of a given size. The structural element is applied to all pixels of binary image and its origin is combined with a single binary pixel. Consequently, the entire structural element is wrapped and a subsequent alteration of the corresponding pixels of binary images occurs.

Erosion and dilation are the simplest morphological operations used to image processing. Erosion consists of turning on the corresponding pixel to the origin of the structure element B if the entire structure element falls with foreground area of a set A; it "contracts" the boundary of A. Dilation consists of turning on the corresponding pixel to the origin of the structure element B, if the entire structure element overlaps the foreground area of a set A by at least one element; it "expands" the set A.

Morphological opening is the dilation of the erosion of a set A by a structuring element B. It is used for smoothing contours, breaking narrows isthmuses and removes small islands or sharp peaks. On the other hand, morphological closing of a set A by a structuring element B is defined as the erosion of the dilation of that set. It is employed when is intended to smooth contours, fuses narrow breaks and long thin golfs, eliminating small holes too. These morphological operations are illustrated in Figure 4.5.

They are frequently combined to remove small objects or holes, respectively, and are one of the basic operations of morphological noise removal [180]. Hit or miss transform, boundary extraction, connected components, convex hull, thinning, thickening, skeletons, pruning, holes filling, border clearing or top- and bottom-hat operations are examples of morphological operations. Top-hat is the difference between the input and the output of an opening operation; it enhances the thin sharp positive variations. On the other hand, bottom–hat is the difference between the output of a closing operation and the correspondent input image [206].

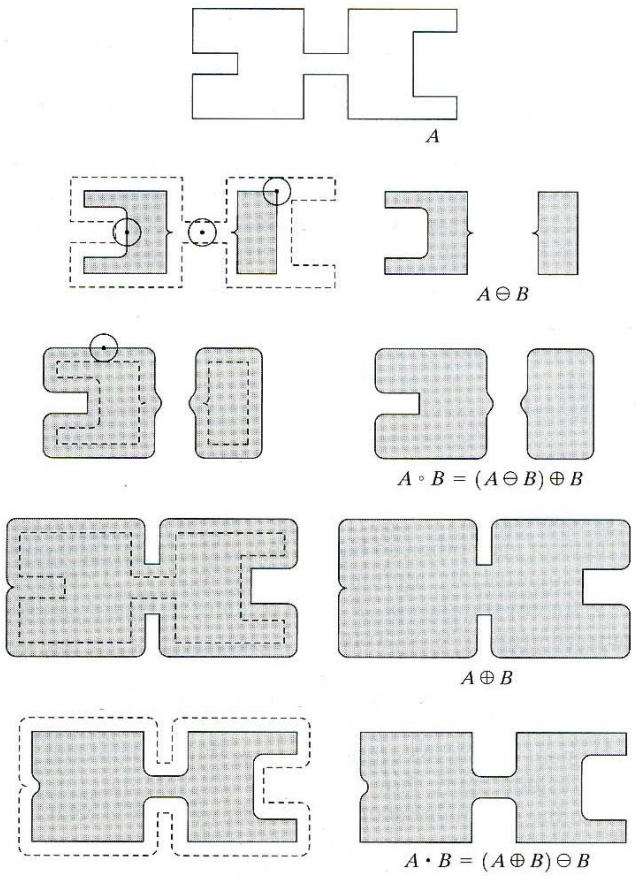

Figure 4.5. Morphologic operations results of opening and dilation using object A (top row). The structuring element is the small circle, whose dot is its center. Opening operation consists of the application of erosion (second row) followed by dilation (third row). Closing operation consists of the application of dilation (forth row) followed by erosion (fifth row).

4.3. Image segmentation

Image segmentation is defined as the process of partitioning an image into multiple sets of pixels, known as segments, and allows the simplification or change in the representation of an image into regions of interest. The level of the subdivision depends on the problem being solved.

It subdivides an image into its constituent regions, or objects, or a set of contours, through the attribution of a label to each pixel. The pixels of a segmented region are similar with respect to some computed property sharing the same label, but adjacent regions are significantly different.

Image segmentation algorithms are generally classified as intensity- or region-based. The first approach consists of partitioning an image based on abrupt changes

in intensity, such as edges, while the second category relies on regions that are similar according to a set of pre-defined criteria.

The several applications of image segmentation cover areas as industry, biology, video surveillance, recognition, traffic control system, biology and microscopy, content-based image retrieval, machine vision, and medical imaging. It is a fundamental tool to locate tumors and other pathologies, measure tissue volumes, diagnosis and study of anatomical structure, surgery planning, virtual surgery simulation and intra-surgery navigation.

Some techniques were tested in the experimental implementation presented in this dissertation, namely Otsu method, k-means clustering, region growing and shape detection, to compare these approaches in myocardial perfusion SPECT images. These methods are explained next.

4.3.1. Otsu thresholding

Thresholding is the simplest and one of the most used methods of image segmentation due to its intuitive properties and simplicity of implementation, whereupon a threshold value separates the objects intended to be extracted from the background. Then, being T the select threshold, any point (x, y), for which $f(x, y) > T$, is called an object point. Otherwise, it belongs to the background, called a background point. Depending on the threshold values, the type of thresholding varies, i.e. if the method only depends on gray-level values, it is a global thresholding, but if it also depends on some local property, it is called a local thresholding; a dynamic or adaptive threshold is employed if the threshold value depends on spatial coordinates.

Otsu method is based on thresholding and it is used to automatically perform clustering-based image thresholding or the reduction of a grey level image to a binary image (see Figure 4.6). It assumes that the image to be threshold has a bi-modal histogram, so it calculates the optimum thresholding that separates those two classes. First, it selects the initial threshold T and segments the two groups of pixels. The algorithm computes the histogram and the probabilities of each intensity level and sets up both initial class probability and respective mean. It updates the threshold T considering the mean intensities previously calculated. Then, the process is repeated until the difference between two successive threshold values is less than

a prescribed tolerance. The optimum threshold is the one that minimizes the intra-class variance and maximizes the inter-class variance.

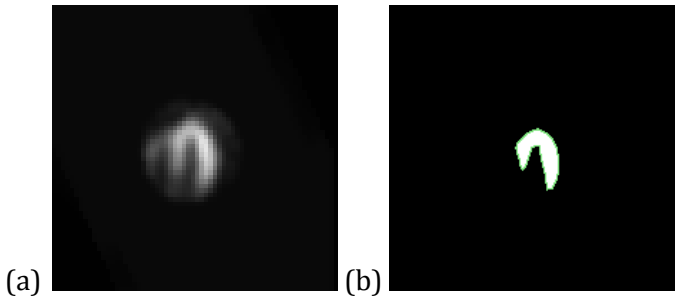

Figure 4.6. Application of Otsu thresholding method on a clear bi-modal image (a), resulting in a well segmented image (b).

The Otsu threshold can be extended to multiple thresholding levels, which is the process of segmenting a gray level image into several distinct regions. It enables the determination of more than one threshold, segmenting the image into one background and several objects, each one at different intensity levels. It can be obtained good results with images that have modal intensity levels well defined.

4.3.2. K-Means Clustering

K-Means clustering algorithm is a segmentation method that classifies the input data points into multiple classes based on the distance from each other. The algorithm assumes data features from a vector space and finds the subsequent clusters, through their centroids. Accordingly, it is a method of vector quantization that aims partitioning n observations into k clusters, whose observation belongs to the cluster with the nearest mean. The main applications of this method are vector quantization, cluster analysis and feature learning. It is exemplified in Figure 4.7.

This method relies on convergence to a local minimum, which may produce counterintuitive results. Furthermore, an inappropriate choice of the number of clusters k may yield poor results, if the number of clusters in the data set is quite different. Unfortunately, the facts of both the Euclidean distance being used as metric and variance as measure of cluster scatter are features that makes k-means as efficient as limited.

Several variations of this algorithm have been developed due to overcome computational complexity and time consuming. Some examples are the following methods: Jenks natural breaks optimization, k-medians clustering, k-medoids, fuzzy

C-means clustering, Gaussian mixture models with expectation-maximization algorithm, kd-trees, spherical k-means or even minkowski metric weighted k-means.

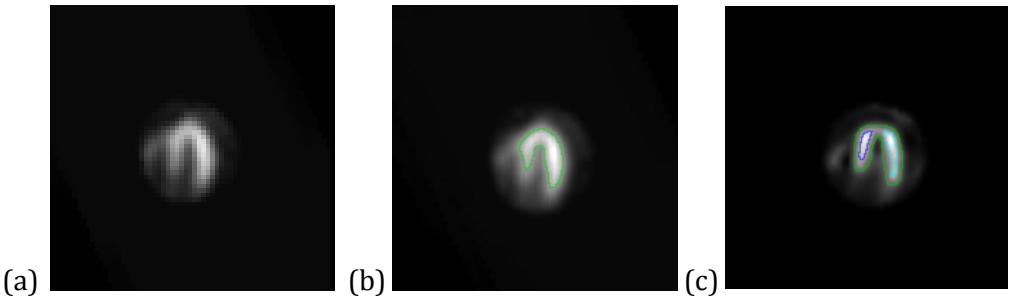

Figure 4.7. (a) HLA myocardial perfusion slice. (b) Segmentation using k-means (3 clusters). (c) Segmentation using k-means (5 clusters). Note that an inappropriate choice of the number of clusters k may yield poor results, if the number of clusters in the data set is quite different.

4.3.3. Region growing

Region growing is an unsupervised region-based image segmentation method that groups pixels or sub-regions based on both predefined similarity and stopping criteria. The algorithm starts with a single pixel or set of pixels defined as seed points, from which the segmented region grows according to pre-defined conditions of similarity between the seeds and their neighboring pixels. The selection of similarity criteria depends on the problem under study and the type of available data. The formulation of a proper stopping rule, that stops the region growing from the seeds when no more pixels satisfy the inclusion criteria, is one of the major difficulties of this method (see Figure 4.8).

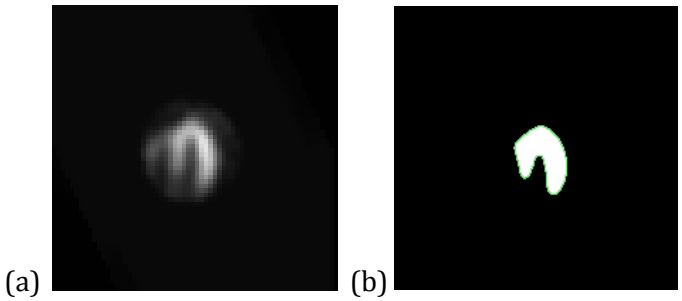

Figure 4.8. Segmentation of (a) HLA myocardial perfusion slice using region growing method, resulting in image (b). The difficult definition of the stopping criteria can result in lack of accuracy.

Image segmentation methods based on region growing can separate regions with the same properties, but requires high power and time consuming.

4.3.4. Level set methods

Level set method is based on implicit representation of the interface. It is a numerical technique for tracking interfaces and shapes, since it can perform numerical computations involving curves and surfaces on a fix grid without having to parameterize these objects. It enables segmentation of time-varying shapes.

The main advantages of the level set methods are the fact that topological changes are handled smoothly with no user intervention required, as well as corners and cusps, using methods borrowed from hyperbolic conservation laws. Moreover, the method is easily extended to higher dimensions [175].

The fast marching method is related to the level set method, but solves a given problem much more quickly. It also uses an implicit representation for an evolving interface, but the embedding function carries much more information. This method requires the entire evolution of the interface to be encoded in the embedding function. This enables a faster solvation of the problem with one single pass over the mesh, contrasting with the level set method where each time steps requires an additional pass over the mesh to evolve the level set function in time.

The fast marching method needs an initialization that must be selected closed to where the exact solution is assigned, consisting of all the nodes that are immediately adjacent to the initial interface. Higher degree of accuracy can be reached using a bi-cubic interpolation function. It is not just used to obtain accuracy for the distance to the zero level set, but also for sub-grid resolution of the shape of the interface and sub-grid resolution of the level set function.

Therefore, re-initialization is employed to reconstruct the level set function to be the signed distance function, i.e., it fixes the level set function when the velocity field does not preserve the level set function as a signed distance function. An alternative is to adjust the velocity field in the first place.

The fast marching method has made a contribution to several application, like crack propagation, shape reconstruction, image processing, medical imaging, computer graphics and visualization and robotic navigation [179].

4.4. Image Quantitative Analysis

Image analysis can be defined as the extraction of meaningful information from images. Shape descriptors are used in a great number of image processing applications due to their capacity of characterization of the regions of interest. The reason for a permanent interest for newly created shape descriptors relies on the demand for more efficient shape classification procedures.

4.4.1. Labeling

Extracting and labeling of various disjoint or connected point in an image is fundamental to automated image analysis applications. The algorithm starts by scanning a binary or grayscale image, pixel-by-pixel, from both left to right and top to bottom. A label is attributed to each pixel, and groups the pixels into components based on pre-defined pixel connectivity. The equivalent label pairs are stored in an equivalent matrix, or into equivalence classes, and a unique label is assigned to each class. Finally, a second image scan replaces the labels previously assigned by the label assigned of its equivalence class. Then, all connected component pixels share the same label. The labeled objects, or even only their boundaries, are often displayed with different gray levels or colors, as illustrated in Figure 4.9.

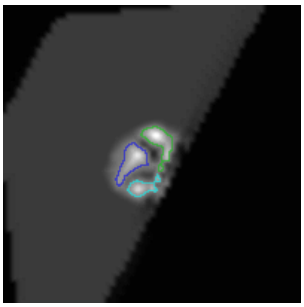

Figure 4.9. Identification of three objects through different color labels.

4.4.2. Extraction of geometric dimensions

After segmentation and connected components labeling, the objects of interest may be described through shape parameters, namely elementary geometrical parameters. The parameters used in the present dissertation will be now exposed.

The perimeter can be obtained from the chain code of the object boundary, taking into account the length of the chain code and considering that all steps in diagonal directions are longer by a factor of 2. For an 8-neighborhood chain code the perimeter is given by the equation 4.2, where n_e and n_o are respectively the number of even and odd chain code steps.

$$perimeter = n_e + \sqrt[2]{n_o} \tag{4.2}$$

Perimeter results directly from the construction of the boundary line with equidistant samples and is well approximated to the number of sampling points times the mean distance between the points. Note this shape perimeter is sensitive to noise, so comparison of perimeters from different images must be realized carefully. However, it does not depend on the orientation of the objects on the image plane.

Roundness, or circularity of a region, is a geometric feature that is invariant under translation, rotation and scaling. Given an object R, the circularity is given by function 4.3, where A represent the object area, i.e, the number of pixels within the object, and P its perimeter. It results in the maximum value of 1 for a perfect round region and a value in the range between 0 and 1 for all other shapes. This shape descriptor also offers information on how regular an object is, because the inverse of this measurement defines the compactness factor (see eq. 4.3).

$$CR = \frac{4\pi A}{P^2} \tag{4.3}$$

Equivalent spherical radius of an irregularly-shaped object is the equivalent radius of a hypersphere of the same size than the label object, which value depends on the image spacing.

Elongation is a basic shape descriptor with a clear intuitive meaning. Its standard measure is area-based because all points belonging to the shape are involved in its computation. It is derived from the shape orientation definition which is based on the axis of the last second moment of inertia. Therefore, it is the ratio of the largest principal moment to the second largest principal moment. Its value is greater or equal to 1.

4.5. Image classification

Machine learning and pattern recognition, or image classification, are the hot topics since the last two decades with the ever increasing amount of data becoming available. Smart data analysis is an essential tool for technological progress. Machine learning or pattern recognition applications concern the construction and study of systems that can learn from data. Web page ranking, collaborative filtering, automatic translation of documents, face recognition, speech recognition, optical character recognition and entity recognition are examples of machine learning applications.

The main challenge of image classification deals with representation of data instances and respective representation, as well as with generalization that provides the system to perform classification on unseen data, i.e., the ability to perform accurately on new examples or tasks after having experienced a learning data set. The training set has generally unknown distribution and the learner must build its distribution model to produce accurate predictions.

These algorithms can be organized based on two properties: the desired outcome or the type of input available during the training machine. Furthermore, they can be grouped into generative and discriminative models. Some examples of classification algorithms are decision tree learning, association rule learning, artificial neural networks, inductive logic programming, support vector machines, clustering, reinforcement learning, representation learning, similarity and metric learning, sparce dictionary learning and Bayesian networks.

4.5.1. Bayesian classifier

Pattern classification is the act of assigning a class label to an object, physical process or event, based on measurements that are obtained from that object. The definition of relevant classes depends on the nature of the application. Probability theory is commonly used for pattern recognition design, whose pattern-generating mechanism is represented within a probabilistic framework, illustrated in Figure 4.10.

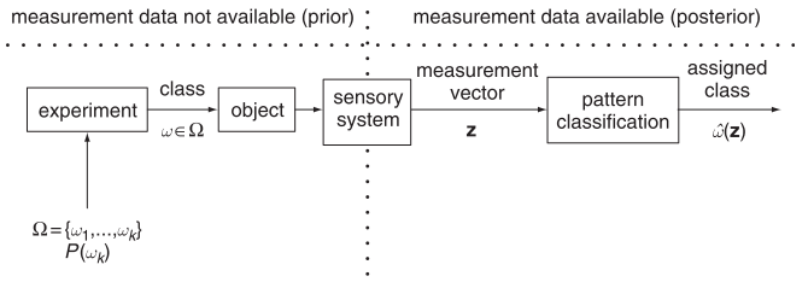

Figure 4.10. Statistical pattern classification [181].

Bayesian network is based on a stochastic experiment defined by a set of $\Omega = \{\omega_1, \ldots, \omega_k\}$ of k classes, which are assumed as mutually exclusive. The probability $P(\omega_k)$ of having a class ω_kk is called the *prior probability* and represents the knowledge about the class of an object before the measurements of that objects are available. The sensory system produces a *measurement vector* z with dimension *N*, each one containing the object from the same class. The conditional probability density function of the measurement vector z is given by $P(\mathrm{z}|\omega_k)$ and means the density of z coming from an object with known class ω_k. If z comes from an object with unknown class, its density is given by $P(\mathrm{z})$; it is the unconditional density of z. The pattern classifier casts the measurement vector in the class that will be assigned to the object. This is accomplished by the so-called decision function that maps the measurement space onto the set of possible classes.

When an object is classified, both a uniform cost function and a zero cost function are obtained when the classification is correct. Since Bayes classifier is based on (1) the damage, or loss of value, when an object is erroneously classified, then it can be quantified as a cost or loss and (2) the expectation of the cost, i.e., it can be employed as an optimization classifier. Their uses for Bayes classification requires the specification of the conditional probability densities [181].

Bayes' formula is an important method for computing conditional probabilities and it is often used to compute posterior probabilities of given observations.

4.6. Evaluation

Every image analysis algorithms must be validated through performance analysis, whose evaluation depends on the type of image analysis problem. There are different categories, namely image classification or abnormality detection problems and image segmentation problems.

Metrics to evaluate the performance of image classification involves the relative frequency of correct and incorrect decisions. True and false positives and negatives are commonly used in this context, i.e. true positive (TP), false positive (FP), true negative (TN) and false negative (FN), whose positive and negative refers to the decision made by the algorithm and true and false to how the algorithm decision agrees with the actual clinical state, as Table 4.1 synthetizes.

Derived from these metrics, additional performance metrics are defined: accuracy, sensitivity or recall and specificity, precision, and F-measure. Their definition and formulas are synthetized in Table 4.2. They can be stated as a fraction between 0 and 1 and consequently as a percentage.

Table 4.3. Confusion matrix (adapted from [182]).

		Algorithm decision	
		Abnormality present	Abnormality not present
Clinical decision	Abnormality present	**True positive**	**False negative**
	Abnormality not present	**False positive**	**True negative**

Image segmentation problems are evaluated using performance metrics based on the identification of regions that share some semantic label, such as abnormality, or on the identification of all basic regions in the image. The set of obtained results is then counted and the resulting number of correct or incorrect results is more complex than the measurement of classification problems.

Table 4.4. Definition of performance metrics and respective mathematical formulas.

Metric	**Definition**	**Formula**
Accuracy	Measure of the global performance concerning correct decision.	$\frac{TP+TN}{TP+TN+FP+FN}$
Sensitivity, Recall or True Positive Fraction	Measure how often the algorithm reports that an abnormality exists in the instances where it actually exists.	$\frac{TP}{TP+FN}$
Specificity or False Positive Fraction	Measure how often the algorithm reports normal when no abnormality exists.	$\frac{TN}{TN+FP}$
Precision	Fraction of detections that are relevant.	$\frac{TP}{TP+FP}$
F-measure	Combines precision and recall by their harmonic mean (F_{β}). The traditional measure is the F_1 measure, where P and R are weighted evenly.	$F_{\beta=\frac{(1+\beta^2)(P.R)}{\beta^2 P+R}}$

Commonly, results of image segmentation are compared with a ground truth, whose segmented regions are classified as correct segmentation, over-segmentation, under-segmentation, missed region and noise region. Its evaluation is based on measures that consider distance between two contours, as Hausdorff distance, mean absolute contour distance or degree of overlapped areas.

The Dice's coefficient is widely used to evaluate the performance of automatic segmentation algorithms results based on its overlapped area with its ground truth, i.e. it measures the extent of spatial overlap between two binary images. Thus, it gives more weighting to instances where the two images agree. Its values range between 0 and 1, respectively corresponding to no overlap or perfect agreement [183]. It can be obtained as a percentage value, through equation 4.4.

$$D = \frac{2(A \cap G)}{A \cap G + A \cup G} \times 100 \tag{4.4}$$

Free-response ROC (FROC) curve is used when the objective is counting all instances of abnormalities in an image, representing the space of tradeoffs between the sensitivity and the generalized specificity of an algorithm. Similarly to ROC curve, the area under FROC curve is also considered to evaluation [182].

4.7. Conclusions

This chapter has provided the general principles of digital image processing. Image processing techniques as image intensity normalization, image resampling and image interpolation are employed in the experimental implementation that will be explained in Chapter 5, as pre-processing image techniques. Morphological techniques also constitute a powerful set of tools for extracting features of interest in an image. The more significant advantage in terms of implementation is the fact that dilation and erosion are primitive operations that are the basis for a broad class of morphological algorithms, namely top-hat and bottom-hat.

Image segmentation is an essential preliminary step in the majority of automatic pattern recognition and scene analysis problems. The specific characteristics of a problem decide the best segmentation technique to be applied, since its basic goal is to partitioning the image into mutually exclusive regions to which there are attached meaningful labels.

Computer vision, machine intelligence and pattern recognition still be in relatively early stages. There methods require the definition of useful shape descriptors and methods for their automation. Furthermore, they reduce the coordinate pairs in the shape vector representation to produce some compact or even single-parameter measure of the approximate shape. Nowadays, they are majority based on heuristic approaches.

Chapter 5

Developed implementation, results and discussion

In this chapter, computational techniques of medical image analysis, mainly of image registration, are integrated in a computational solution to automatically compute a set of features from myocardial perfusion SPECT images and use them to statistical analysis and classify the images as from subjects with myocardial perfusion associated diseases or not. The image registration algorithms used, including the transformation, similarity measure, optimization and interpolator algorithms, will be described and discussed, as well as the segmentation steps. Using the features subset obtained from segmentation method, image classification methods are employed, significantly improving diagnostic performance.

The developed computational solution can be divided into the following steps: (1) formation of a template image; (2) segmentation of the template LV and computation of related geometric dimensions; (3) data registration, i.e. alignment of the gated myocardial perfusion SPECT images' slices under study with the pre-built template image; (4) statistical analysis and image classification. These steps are minutely explained next and the experimental results obtained at each step will be discussed.

With this implementation it is not intended to replace physicians' judgment, but assist them in clinical decision, such as complementing medicine teaching of cardiology.

5.1. Implementation

The computational solution was fully implemented in C++ and tested on a notebook PC with Intel® Pentium® CPU P6200 2.13GHz processor, RAM 4.0GB, NVIDIA® GFORCE® with CUDA® 315M graphic, Samsung SSD 840 Series with 100 GB and a TOSHIBA MK3252GSX with 300 G and under Microsoft Windows 7 NT operating system (32-bits). Computational techniques of image segmentation, processing and classification were implemented using the free open source toolkits Insight Toolkit (ITK) 4.3.

5.2. Material and methods

5.2.1. Dataset

Data used in the preparation of this dissertation were provided by *Hospital Lusíadas Porto, Porto, Portugal*. The control group contains female and male stress and rest gated myocardial perfusion SPECT images. The dataset is formed by 180 3-D images from 48 patients with healthy cardiac condition and 72 3-D images from 12 patients with associated cardiac diseases. Data was provided in DICOM multi-frame image format.

The image acquisition system was a single head e-cam SPECT camera (SIEMENS-Germany) equipped with a low-energy high resolution collimator. The data from the SPECT studies was acquired in 64 × 64 image matrix for 32 projections over 180◦ arc, 25s per projection, from 45◦ right anterior oblique (RAO) to the 45◦ left posterior oblique (LOP). These images were reconstructed using the filtered back projection algorithm and a low pass Butterworth filter (cut off: 0.4-order: 5). Thereafter, semi quantitative analysis of LV myocardium perfusion has been done by Cedars-Sinai Software (20 segment model).

5.2.2. Template myocardial SPECT image

The template myocardial SPECT image is built as a consistent reference against with it will be compared the images to be classified. Its formation requires three distinguished steps, namely (1) image registration of healthy patients' images,

(2) segmentation of LV, (3) coronary artery mapping and (4) registration of image obtained in step 1 with the coronary artery mapping image obtained in step 3.

The template image is composed of 12 slices for each cardiac axis, there being a template image for stress and rest clinical protocol. The stress template myocardial SPECT is the result of 16 healthy patients and rest template image corresponds to the registration of 6 patients' exams (these patients are the same of the stress dataset used for building the template image). This difference is due to the fact that the patients firstly realize the stress protocol and the rest protocol is not always necessary, there being a few number of rest protocol images.

At the end, there are built three template images per clinical protocol (rest or stress), one for each axis (SA, VLA and HLA), consisting of the registration of myocardial SPECT images from healthy patients containing the coronary artery mapping, performing a total of six template myocardial perfusion SPECT images.

5.2.2.1. Healthy myocardial SPECT image registration

To build the 3-D template SPECT image, an image from the dataset was selected to be the reference image. Then, the data of the control group was automatically registered with the reference image. The result of the registration process was defined as the template image. Note that the template image is built just once. The full algorithm is presented in Figure 5.1.

Cardiac structures have different dimensions for each patient, and more significantly depending on the patient genre, i.e., as the image is from a female or male patient. Then, it is fundamental that the moving image pass through a cubic B-Spline interpolator to set the origin, spacing, direction and size features of the fixed image. A rescale intensity image filter is used next to normalize both images intensities.

Hereafter, the registration method is implemented. It is divided into a pre-registration method based on rigid transforms and a registration method based on deformable transforms, both using multi-resolution registration technique, since it is faster and efficient.

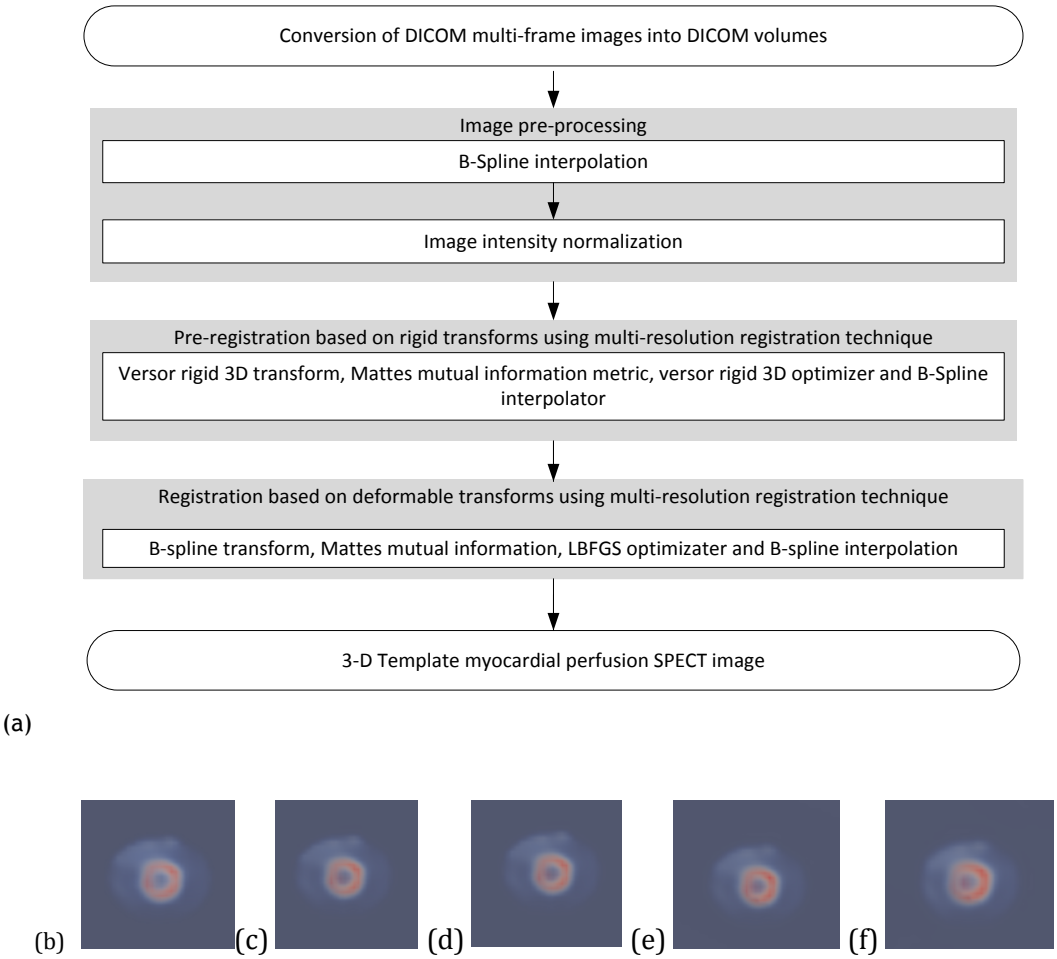

Figure 5.1. Algorithm framework and images' examples obtained at each step: (a) algorithm framework implemented to generate a template myocardial perfusion SPECT image; (b) input 3-D image; (c) B-spline interpolation 3-D result; (d) rescale intensity image filter 3-D result; (e) image pre-registration 3-D result; (f) image registration 3-D result.

The pre-registration method consists of an initial translational pre-registration step. A centered transform initializer uses the center of mass given by the image intensities of input images. Then, it is applied a rigid 3D transform consisting of a 3D rotation and a 3D translation, specified by a versor and a vector, respectively. The similarity measure used is the Mattes mutual information, based on information theory, which consists of measuring how much information in one random variable tells about another variable using one set of intensity sample to evaluate the marginal and joint probability density function at discrete positions. The optimizer that searches for the best geometric transformation is the versor rigid 3D transform optimizer that implements a gradient descent optimizer for the transformation parameter space. The employed interpolator is the cubic B-Spline interpolator. The main parameters defined to properly perform this pre-registration

algorithm described are presented in Table 5.1. These values were experimentally obtained, through trial and error.

After obtaining the pre-registered image, a final registration step based on deformable transformation is applied, to register it with the reference image.

Table 5.1. Main parameters' values defined in the pre-registration algorithm of healthy myocardial SPECT images.

Function	Parameters	Values
Metric	Number of histogram bins	128
Metric	Number of spatial samples	25000
Optimizer	Translation scale	100000
Optimizer	Number of iterations	100
Optimizer	Maximum step length	0.05
Optimizer	Minimum step length	0.005, if multi-resolution level = 0. 0.00005, if multi-resolution level > 0.
Multi-resolution registration	Number of levels	3

The registration method starts with a B-Spline transform that encapsulates a deformable transform of points from one n-dimensional space to another n-dimensional space. The Mattes mutual information is also used as similarity measure. The optimizer used here is a LBFGSB optimizer, which minimizes a nonlinear function $f(x)$ of n variables subject to simple bound constraints. Then, it is employed a B-Spline intensity interpolator. The main parameters defined to perform properly the registration algorithm described are presented in Table 5.2. These values were experimentally obtained, through trial and error.

5.2.2.2. Segmentation of the LV and computation of related geometric dimensions

The LV segmentation is implemented in 2D. The first step is to extract the DICOM volume's slices obtained in the previous registration step. Due to the image acquisition system, DICOM images have low resolution. It is partially improved passing the template image by a resample image filter that sets the default pixel value to 10 and an output spacing factor of 0.3.

Next, the images are post-processed using mean spatial filtering, to reduce the noise of the images, followed by morphological operations. Opening and closing operations were used to implement a top hat followed by a bottom hat. The obtained image is added to the slice, and then the bottom hat is subtracted. This

step improves the gradient magnitude of the template SPECT image's slices. Posteriorly, k-means clustering using 3 clusters is employed.

Table 5.2. Main parameters' values defined in the registration algorithm of healthy myocardial SPECT images.

Function	Parameters	Values
Metric	Number of histogram bins	128
Metric	Number of spatial samples	(Number of pixels of the fixed region * 20.0)/ 50.0
Metric	Translation scale	100000
Optimizer	Number of iterations	100
Optimizer	Relaxation factor	0,9
Optimizer	Cost function convergence factor	1e9, if multi-resolution level = 0. 1e14, if multi-resolution level > 0.
Optimizer	Projected Gradient Tolerance	1e-9, if multi-resolution level = 0. 1e-14, if multi-resolution level > 0.
Optimizer	Number of iterations	200
Optimizer	Number of Evaluations	400
Optimizer	Number of Corrections	50
Interpolator	Number of grid nodes in one dimension	10
Interpolator	Spline order	3
Multi-resolution registration	Number of levels	3

Here, the LV is already segmented. A label map filter is applied and the contour of each object is obtained. Object related geometric dimensions are computed, specifically perimeter, equivalent spherical radius, roundness, elongation and number of pixels. Each geometric dimension is written into a vector. So, five vectors are obtained, constituting the set of features from myocardial perfusion SPECT images that has been initially proposed to aim. Figure 5.2 illustrates this algorithm.

5.2.2.3. Coronary artery mapping

The next step consists of generating the coronary artery mapping of the template image previously obtained, which posterior alignment with images under study will allow the clinical expert to observe the localization of cardiac abnormalities.

To perform this task, the 20 segment-based coronary artery mapping was manually drawn for the apical, medial and basal region of the template myocardial perfusion SPECT image of each axis

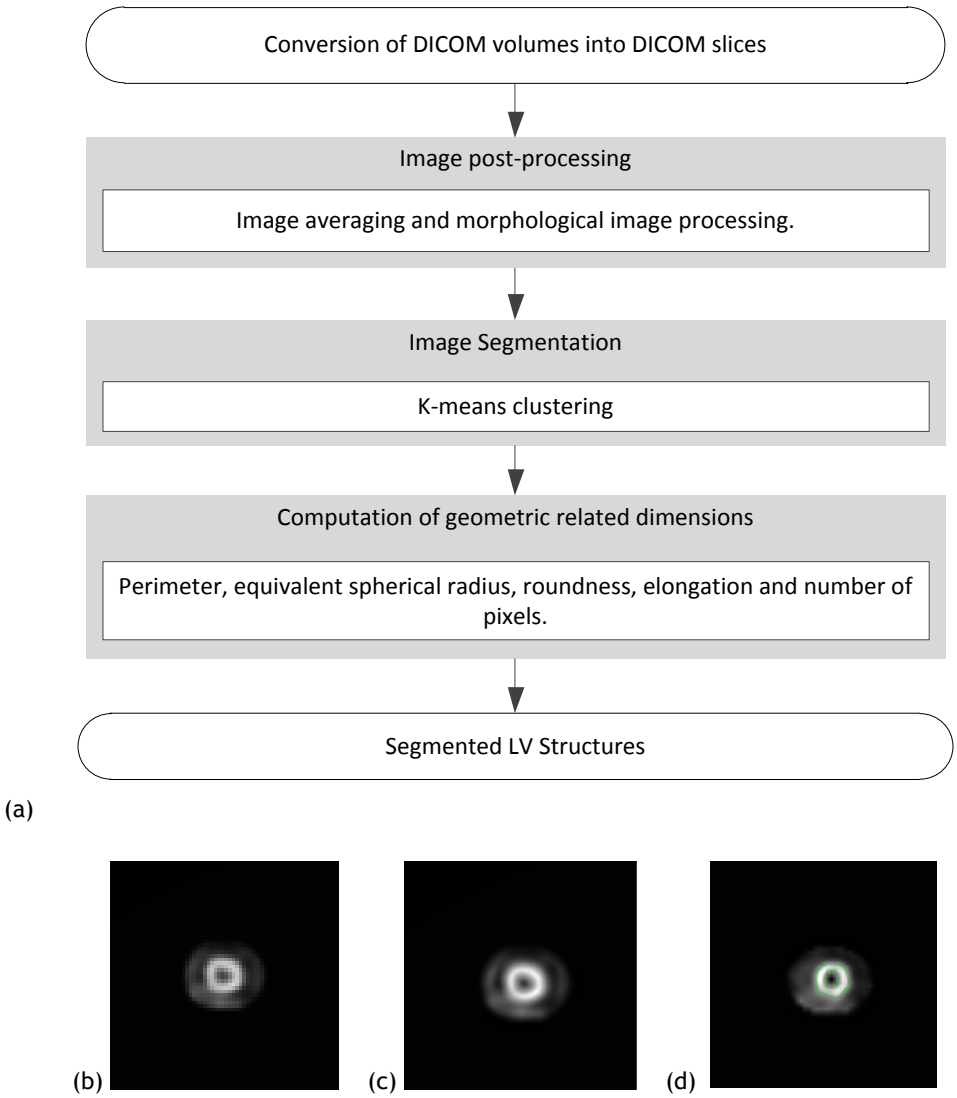

Figure 5.3. Segmentation algorithm: (a) segmentation algorithm framework; (b) input 3-D image (c) 3-D image result of image averaging followed by morphological processing techniques; (d) example slice of segmented myocardial perfusion using k-means 3 clusters.

5.2.2.4. Registration of coronary artery mapping

This is the last step required to build the template coronary artery mapping of myocardial perfusion SPECT image. Similar algorithms to those described in section 5.2.2.1 were used to align the coronary artery mapping image slices, obtained in the previous step, with the template image obtained in section 5.2.2.1. Accordingly, it is also divided into a pre-registration method based on rigid transforms and a registration method based on deformable transforms, both using multi-resolution registration technique. The registration algorithm was implemented bi-dimensionally, since the input images are the 2-D segmented images previously

obtained. The algorithm employed and registration components are synthesized in Figure 5.3.

Here, the pre-registration method starts with the same centered transform initializer used in section 5.2.2.1. Then, it is applied an affine transform, a linear transformation that maps lines into lines. As previously, the similarity measure employed is the Mattes mutual information. According the transform method employed, a regular descent optimizer is used. These components are combined with a linear interpolator. The main parameters defined to perform this pre-registration method are presented in Table 5.3. These values were experimentally obtained, through trial and error.

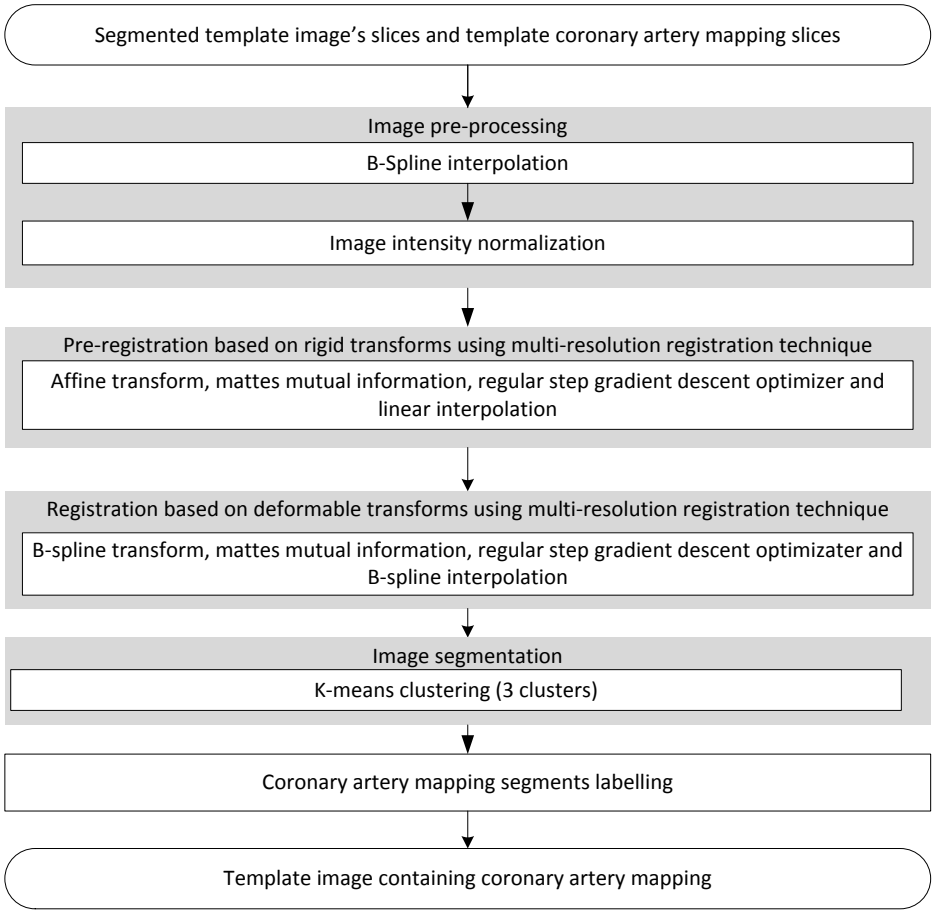

(a)

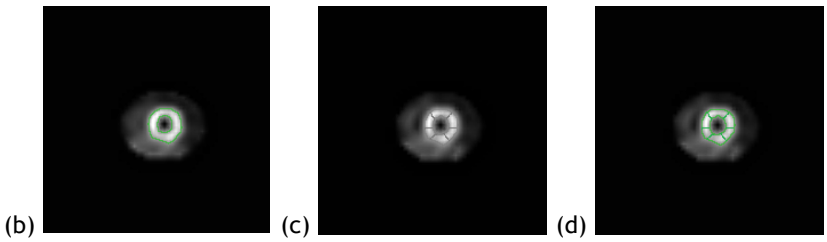

(b) (c) (d)

Figure 5.2. Pre-registration algorithm used to align the template image's slices with the corresponding coronary artery mapping; (b) Image to be aligned; (c) Pre-registration between the input image and the coronary artery map obtained; (d) Coronary artery mapping registration final output.

The pre-registration algorithm's output is the image under study with the coronary artery mapping. Therefore, a final registration step based on deformable transformation is applied, to register it with the coronary artery mapping of the template image.

The final registration algorithm is based on multi-resolution registration approach. It is compound by the B-Spline transform, the Mattes mutual information metric, the regular step gradient descent optimizer and the B-Spline intensity interpolator. The main parameters used to perform the method were experimentally obtained, presented in Table 5.3, through trial and error.

Table 5.3. Main parameters' values defined in the pre-registration algorithm used for aligning the template myocardial perfusion SPECT images with the coronary artery mapping.

Function	Parameters	Values
Metric	Number of histogram bins	128
Metric	Number of spatial samples	50000
Metric	Translation scale	100000
Optimizer	Number of iterations	200
Optimizer	Relaxation factor	0,8
Optimizer	Maximum step length	0.5, if multi-resolution level = 0.
Optimizer	Minimum step length	0.05, if multi-resolution level = 0. 0,0005, if multi-resolution level > 0.
Multi-resolution registration	Number of levels	3

Table 5.4. Main parameters' values defined in the registration algorithm used for aligning the template myocardial perfusion SPECT images with the coronary artery mapping.

Function	Parameters	Values
Metric	Number of histogram bins	50
Metric	Number of spatial samples	(Number of pixels of the fixed region * 60.0)/ 100.0
Metric	Translation scale	100000
Optimizer	Number of iterations	200
Optimizer	Relaxation factor	0.9
Optimizer	Maximum step length	10
Optimizer	Minimum step length Tolerance	0.1
Optimizer	Number of iterations	200
Interpolator	Number of grid nodes in one dimension	7
Interpolator	Spline order	3
Multi-resolution registration	Number of levels	3

5.2.3. Myocardial SPECT image segmentation and registration

The computational techniques explained before, used to segment the LV and its registration with the template image, are also used to register the image under study with the template image. The complete algorithm is summarized in Fig. 5.4.

The first step consists of defining the first and last slice of interest, to segment and register only the slices with relevant information. The empirical analysis of image datasets has proved the first and last fifths of DICOM volumes do not contain relevant information. Accordingly, the algorithm was programmed to consider the first slice of the second fifth of the volume as the first slice to be analyzed and the last slice of the forth fifth of the volume as the last slice.

Secondly, the image under study is segmented based on k-means clusters using 3 clusters and respective geometric dimensions are computed, using the algorithm described in section 5.2.2.2. This step enables clinical professionals analyzing the myocardial perfusion of the patient, providing a better visual evaluation of myocardial perfusion extent.

Note since the algorithms of image processing, registration and segmentation had already been exemplified through images previously and the following framework applies the same techniques, there is no need of exemplifying the next processes.

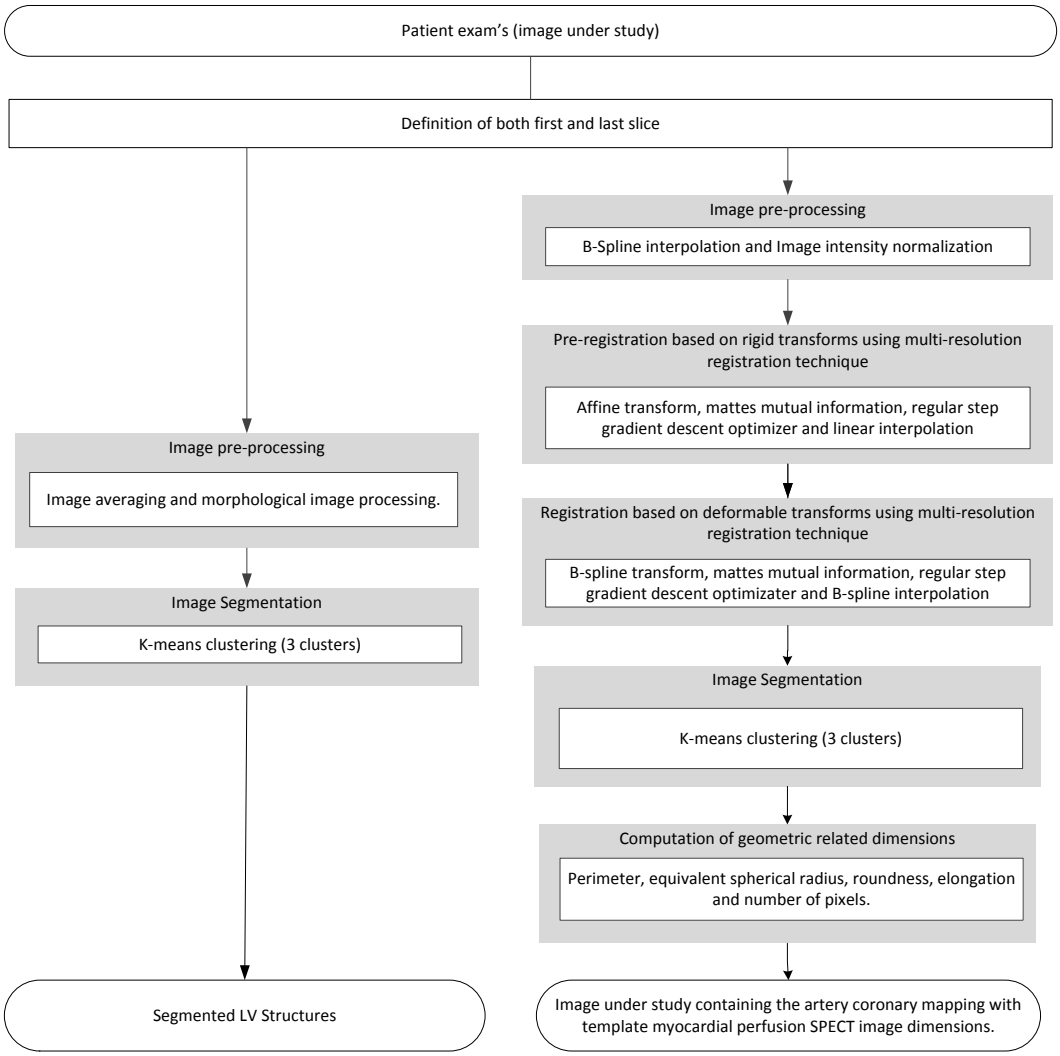

Figure 5.3. Segmentation and registration of patient's exam. Image segmentation provides an accurate visual analysis and image registration of the patient's exam with the template image enables a correct computation of related geometric dimensions according to the normal heart size. Note that the template image slices is chosen according the clinical protocol and axis of the image under study.

As referred before, due to different hearts size between patients and depending on the genre, the computation of cardiac geometric related dimensions would lead to a lack of pattern from healthy and unhealthy geometric dimensions of myocardial perfusion region. It is predictable that healthy myocardial perfusion patients have higher geometric dimensions and unhealthy patients have small myocardial perfusion regions. However, a bigger LV can have considerable geometric dimensions but be unhealthy as well as a smaller structure, very common in women, can be healthy with smaller geometric dimensions.

For this reason, it is fundamental the image under study to be registered with the coronary artery mapping slices. It is done using the same algorithm of section 5.2.2.4. The cardiac structure under study is interpolated considering the origin,

spacing and image size of the template image. Note that the template image slices are chosen according the clinical protocol and axis of the image under study. This step eases clinical professionals in the detection of the myocardial perfusion defects and their location.

Since the output of segmentation process is 2-D and the selection of the adequate coronary artery mapping slice is subjected to observer variability, the middle template coronary artery mapping was chosen to be registered with all patients' slices, aiming geometric related dimensions of each cardiac structure to have the same properties of template image pattern. This registration has enabled a more consistent result in the definition of the normal pattern. Therefore, the registered image is segmented using k-clustering using 3 clusters, since the computation of the maximum perfusion region is not required and it is a reliable segmentation of myocardial perfusion region. Finally, geometric dimensions are computed. This step enables image classification and consequently provides a computer aided diagnosis to support medical decision making.

This algorithm provides a proper segmentation and classification of the patient's gated myocardial perfusion SPECT images under study. The segmented image as well as the computed geometric dimensions are then used to statistical analysis and image classification, described below.

5.2.4. Statistical analysis and image classification

The steps described till section 5.2.3 permit computing a set of features from the template myocardial perfusion SPECT image as well as from the images under study. Here, they are used to statistical analysis and posterior classification of the images. At this section, the implemented algorithm for performing statistical analysis and image classification, which is based on Bayesian frameworks, is described. Figure 5.5 illustrates the classification algorithm.

Per set of slices previously segmented, the mean of each geometric dimension is computed and written into a sample vector. So, here there are five sample vectors containing the mean values of the related geometric dimensions of every set of segmented slices. They are defined as measurement vectors, used as input data to perform the statistical analysis.

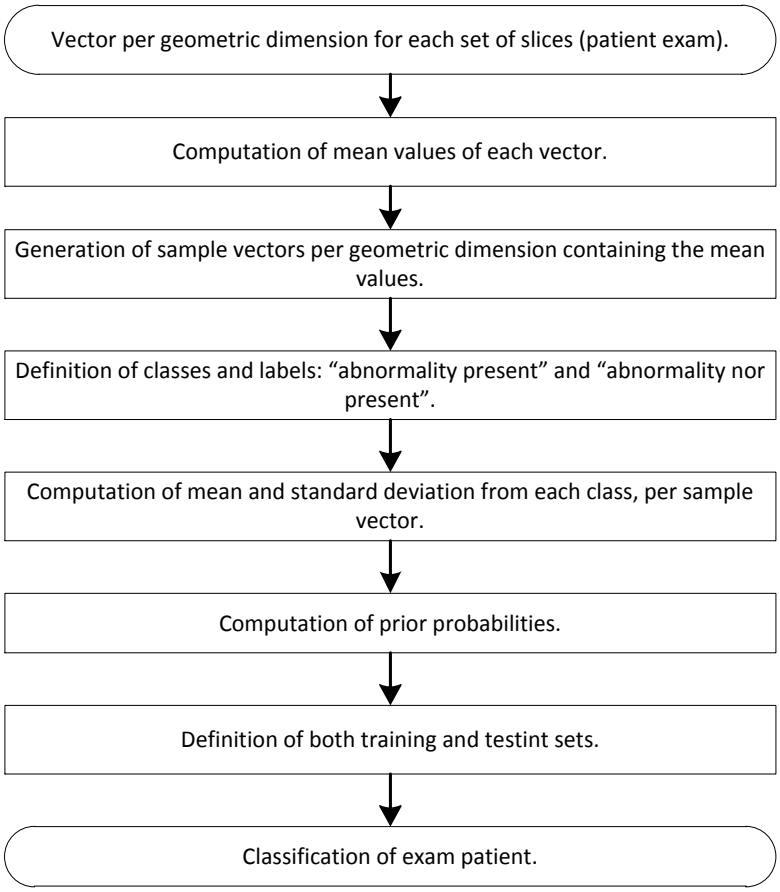

Figure 5.4. Algorithm used to perform statistical analysis and image classification.

As required from Bayesian framework, there are defined two classes and respective labels, corresponding to (1) myocardial perfusion SPECT images features from healthy patients and (2) myocardial perfusion SPECT images features from unhealthy patients. Then, the sample vectors containing myocardial perfusion features from healthy patients are attributed into the first class and, similarly, the sample vectors containing myocardial perfusion features from unhealthy patients are attributed to class 2. The classifier computes mean and standard deviation are computed for both classes, per geometric dimension. These vectors are defined as reference and their prior probabilities are computed.

Both training and testing sets have to be defined. The training set consists of pre-defined sample vectors of 10 patients and the testing set contains the sample vectors related to every geometric dimension that it is intended to classify. Therefore, the classifier evaluates the geometric dimensions of each cardiac axis per patient and clinical protocol, since stress and rest exams can be done in different days.

The algorithm output is the classification of each geometric dimension, based on the Bayes' theory. Here, the health professional has a mathematical validation of its clinical diagnostic as a clinical decision support system.

5.3. Results

At this section, the obtained results will be exposed. The built template image is shown in section 5.3.1. Segmentation algorithm presented before was validated using Dice's Coefficient, whose results are presented in section 5.3.2. Classification results are presented in section 5.3.3.

5.3.1. Template myocardial perfusion SPECT

As explained at section 5.2.2, the first step of the presented computational solution was to build a template myocardial perfusion SPECT image, using computational image registration techniques. In order to validate the proposed image registration method, visual evaluation of the template SPECT image was performed by a clinical professional. Both stress and rest segmented template myocardial SPECT slices, using k-means clustering, are shown in Figure 5.6 and Figure 5.7.

The manual 20-segments coronary artery mapping has been aligned with the template image slices to generate the manual coronary artery mapping template images. Figure 5.8. shows basal, middle and apex regions for SA slices and middle region for both HLA and VLA, for stress clinical protocol, while Figure 5.9. presents the equivalent results for rest studies.

(a)

(b)

(c)

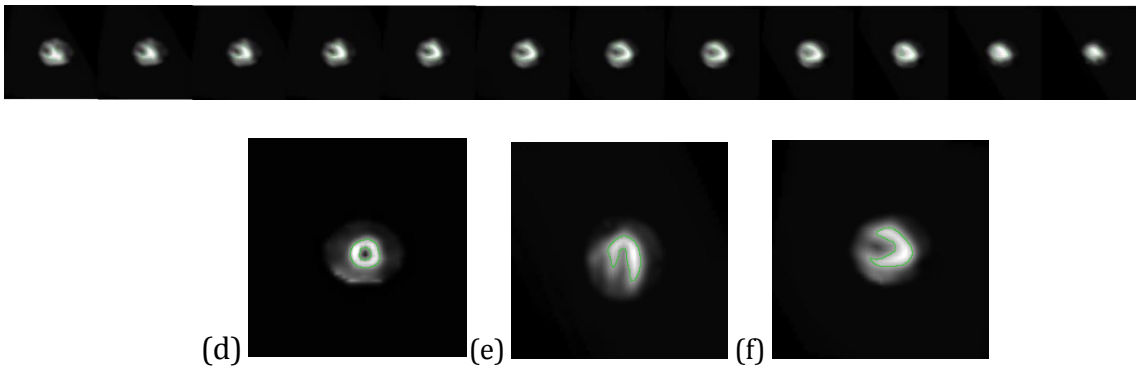

Figure 5.5. Segmented template stress SPECT image obtained using computer image registration techniques: (a) SA ; (b) HLA ; (c) VLA; (d) Zoomed SA example slice; (e) Zoomed HLA example slice; (f) Zoomed VLA example slice.

(a)

(b)

(c)

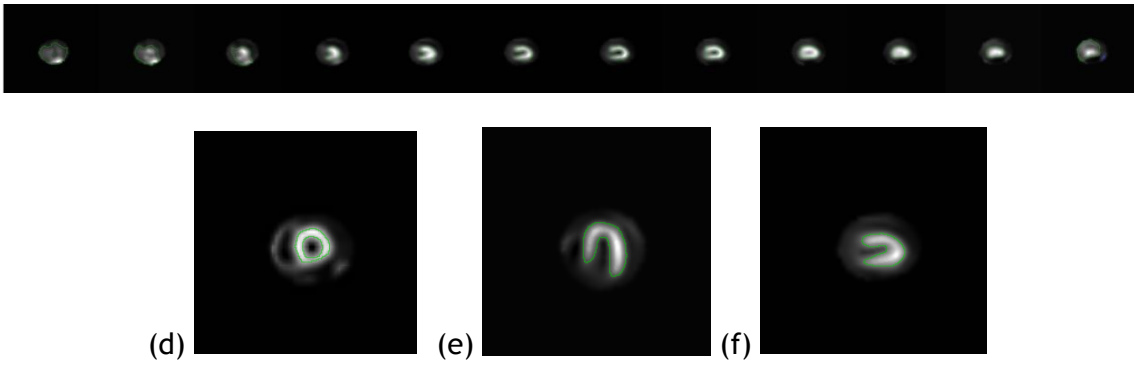

Figure 5.6. Segmented template rest SPECT image obtained using computer image registration techniques: (a) SA ; (b) HLA ; (c) VLA; (d) Zoomed SA example slice; (e) Zoomed HLA example slice; (f) Zoomed VLA example slice.

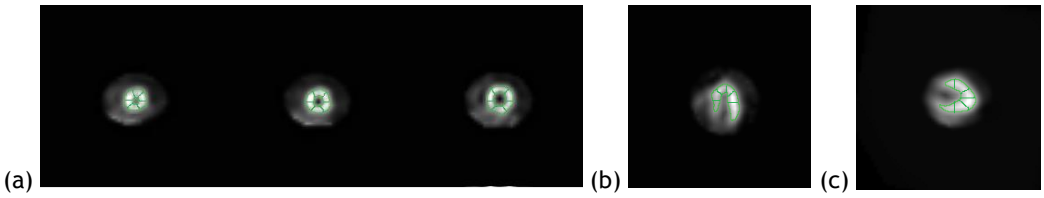

Figure 5.7. 20-segments coronary artery mapping template SPECT for stress studies: (a) SA ; (b) HLA ; (c) VLA.

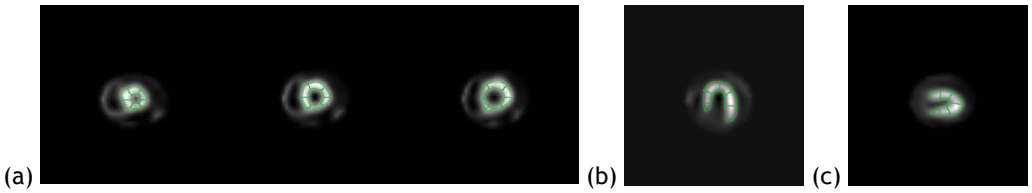

Figure 5.8. 20-segments coronary artery mapping template SPECT for rest studies: (a) SA ; (b) HLA ; (c) VLA.

5.3.2. Segmentation validation

In this section, the performance of the proposed approach is evaluated. Firstly, the validation of the segmentation method was reached through the definition of a gold standard based on a student manual segmentation of 40 slices of a stress myocardial perfusion SPECT image. These slices were segmented using different segmentation methods, namely an automatic segmentation method available on ITK SNAP 3.0, based on snake segmentation, and here developed four automatic algorithms: Otsu multiple threshold with 3-levels, k-means clustering using 3 clusters, region growing and shape detection. Dice's coefficient was computed using MATLAB, whose results are shown in Table 5.5.

Table 5.5. Dice's coefficient computation between manual segmentation and five automated methods.

	ITKSNAP	Otsu Multiple-threshold	K-means Clustering	Region Growing	Shape Detection
	0.0284	0.0000	0.6137	0.0000	0.0000
	0.1846	0.6406	0.6708	0.0688	0.4314
	0.4091	0.7061	0.7962	0.6390	0.6794
	0.3826	0.7425	0.8508	0.7585	0.6007
	0.4864	0.7678	0.8284	0.8152	0.4424
	0.4493	0.6688	0.8618	0.7739	0.4467
	0.4115	0.6426	0.7901	0.7583	0.4049
	0.5749	0.6740	0.7633	0.7475	0.5012
	0.5472	0.7741	0.7389	0.8330	0.7629
	0.4565	0.8639	0.7972	0.7995	0.7666
	0.4306	0.8063	0.8332	0.8141	0.6488
	0.4018	0.6113	0.8268	0.6188	0.5083

(continues)

Table 5.5. Dice's coefficient computation between manual segmentation and five automated methods (continuation).

	ITKSNAP	Otsu Multiple-threshold	K-means Clustering	Region Growing	Shape Detection
	0.2090	0.6005	0.7322	0.2203	0.4506
	0.1995	0.0967	0.8437	0.0000	0.0000
	0.5720	0.6974	0.8079	0.7854	0.5578
	0.6780	0.6681	0.8652	0.8069	0.2416
	0.6994	0.6622	0.8983	0.8389	0.3032
	0.6996	0.6088	0.8802	0.8838	0.3650
	0.7015	0.5910	0.7994	0.8961	0.4020
	0.7264	0.6302	0.7877	0.8840	0.5086
	0.6768	0.6303	0.8232	0.8808	0.4587
	0.6112	0.6527	0.8155	0.8699	0.5753
	0.5808	0.6640	0.8002	0.8522	0.6823
	0.5867	0.7424	0.7151	0.8013	0.7651
	0.5569	0.8663	0.6251	0.7535	0.6929
	0.4914	0.7781	0.6791	0.7680	0.5121
	0.0094	0.6742	0.6516	0.0000	0.0000
	0.0735	0.7556	0.8705	0.9476	0.3960
	0.3150	0.7416	0.9147	0.9380	0.5469
	0.4763	0.6659	0.9051	0.9245	0.5361
	0.5161	0.6550	0.9165	0.9203	0.4625
	0.4831	0.6134	0.9109	0.9084	0.4066
	0.5455	0.6449	0.8948	0.9057	0.4462
	0.5615	0.5814	0.8755	0.8868	0.4035
	0.5901	0.6311	0.8494	0.9037	0.4339
	0.6362	0.6592	0.8005	0.9008	0.4240
	0.6748	0.7386	0.8334	0.9124	0.2805
	0.6884	0.6976	0.7444	0.8057	0.0661
	0.5020	0.8291	0.7256	0.2000	0.0690
	0.0742	0.7321	0.7918	0.0000	0.0420
Mean	**0.4725**	**0.6602**	**0.8032**	**0.7005**	**0.4305**

Secondly, the same slices used above were manual segmented by a clinical professional and evaluated similarly. Dice's coefficient results are shown in Table 5.6.

Table 5.6. Dice's coefficient computation between a manual segmentation of a clinical expert and five automated methods.

	ITKSNAP	Otsu Multiple-threshold	K-means Clustering	Region Growing	Shape Detection
	0.0000	0.0313	0.0302	0.4678	0.0000
	0.1314	0.0544	0.0761	0.0000	0.0044
	0.2564	0.2996	0.3190	0.2831	0.3204
	0.5449	0.6683	0.7054	0.6923	0.5938
	0.6248	0.4664	0.6845	0.5970	0.3506
	0.6958	0.5050	0.6061	0.5806	0.2353

(continues)

Table 5.6. Dice's coefficient computation between a manual segmentation of a clinical expert and five automated methods (continuation).

	ITKSNAP	Otsu Multiple-threshold	K-means Clustering	Region Growing	Shape Detection
	0.7504	0.4386	0.7545	0.8584	0.4834
	0.6209	0.7359	0.9179	0.8579	0.6378
	0.5732	0.7025	0.6836	0.6871	0.5504
	0.5269	0.5220	0.5507	0.5784	0.4433
	0.5303	0.4470	0.5386	0.5381	0.2381
	0.4434	0.3708	0.6807	0.4678	0.2555
	0.3956	0.1366	0.6247	0.5351	0.0212
	0.3342	0.0574	0.4719	0.3191	0.1339
	0.7093	0.4945	0.4123	0.6701	0.1913
	0.7330	0.5700	0.5546	0.6887	0.2883
	0.7004	0.7401	0.7084	0.7775	0.3754
	0.7028	0.6575	0.8940	0.8578	0.4093
	0.6938	0.6722	0.8868	0.8646	0.5095
	0.6718	0.7584	0.8653	0.9174	0.4796
	0.6586	0.7700	0.8512	0.9159	0.5692
	0.6645	0.8151	0.9732	0.9117	0.6461
	0.6228	0.7405	0.9219	0.8414	0.6462
	0.4995	0.7054	0.8191	0.6867	0.4022
	0.4667	0.7440	0.6509	0.4872	0.3502
	0.0486	0.5472	0.5668	0.7097	0.5088
	0.0722	0.0096	0.4296	0.3395	0.1662
	0.1241	0.4549	0.5084	0.4911	0.4833
	0.2741	0.7876	0.6916	0.6603	0.5809
	0.4196	0.8257	0.8357	0.8392	0.4741
	0.4887	0.7703	0.9023	0.9333	0.4189
	0.5152	0.7015	0.9838	0.8439	0.3712
	0.3507	0.6384	0.9265	0.9773	0.3560
	0.4669	0.5515	0.9465	0.9010	0.3422
	0.5314	0.4755	0.8251	0.8939	0.2650
	0.5424	0.5153	0.8785	0.7838	0.1053
	0.6479	0.5190	0.8496	0.8815	0.3794
	0.6157	0.2533	0.6607	0.8664	0.3998
	0.6618	0.3074	0.8459	0.6427	0.2499
	0.0654	0.0000	0.8489	0.4302	0.0874
Mean	**0.4844**	**0.5115**	**0.6970**	**0.6819**	**0.3673**

It can be observed the Dice's coefficient presents higher values for k-means algorithm. Thus, the segmentation of template myocardial SPECT slices using k-means (3 clusters), shown in Figure 5.6-7, provides a more valuable computation of valuable myocardial perfusion region's related geometric dimensions, namely

perimeter, equivalent spherical radius, roundness, elongation and number of pixels. Mean values of each geometric dimension per axis are shown in Table 5.7, for stress and rest template image.

Table 5.7. Geometric dimensions of the segmented objects.

Clinical protocol	Axis	Perimeter	Equivalent Spherical Radius	Roundness	Elongation	Number of Pixels
Stress	SA	234.44	25.60	0.72	1.08	504.55
	HLA	223.98	26.53	0.77	1.44	558.23
	VLA	273.27	34.09	0.80	1.14	892.23
Rest	SA	217.66	25.39	0.78	1.39	525.47
	HLA	238.65	31.85	0.85	1.55	776.60
	VLA	247.85	32.93	0.87	1.40	935.65

5.3.3. Bayesian classifier evaluation

The classification algorithm used the geometric related dimensions obtained from segmentation step. Tables 5.8, 5.9 and 5.10 present the geometric dimensions obtained from the segmented structures and both Bayesian classification and clinical diagnosis.

Table 5.8. HLA geometric dimensions of segmented structures and respective Bayesian classification results and comparison with clinical diagnosis.

Patient Number	Stress						Rest						Final Algorithm Classification	Clinical Diagnosis
	Perimeter	Equivalent Spherical Radius	Roundness	Elongation	Number of Pixels	Algorithm Classification	Perimeter	Equivalent Spherical Radius	Roundness	Elongation	Number of Pixels	Algorithm Classification		
1	337.73	40.17	0.75	1.27	1237.54	Normal	388.47	38.82	0.65	1.74	299.44	Normal	Normal	Normal
2	318.62	38.70	0.76	1.25	1151.23	Abnormal	339.19	34.50	0.66	1.51	251.00	Abnormal	Abnormal	Abnormal
3	301.45	36.88	0.77	1.22	1039.89	Abnormal	364.93	37.30	0.67	1.57	283.29	Abnormal	Abnormal	Abnormal
4	349.54	43.49	0.78	1.32	1449.00	Normal	380.58	40.07	0.68	1.66	316.44	Normal	Normal	Normal
5	310.40	37.66	0.76	1.17	1093.92	Abnormal	310.60	34.26	0.69	1.58	247.07	Abnormal	Abnormal	Abnormal
6	349.90	40.82	0.74	1.37	1274.73	Normal							Normal	Normal
7	336.04	40.57	0.76	1.17	1261.00	Normal							Normal	Normal
8	324.71	39.39	0.76	1.23	1190.45	Normal							Normal	Normal
9	341.60	41.23	0.76	1.27	1310.23	Normal							Normal	Normal
10	314.44	38.33	0.77	1.24	1125.73	Abnormal							Abnormal	Normal
11	335.70	40.36	0.76	1.22	1260.07	Normal							Normal	Normal
12	318.75	38.42	0.76	1.27	1130.00	Abnormal							Abnormal	Normal
13	330.90	39.15	0.75	1.16	1173.00	Normal							Normal	Normal
14	347.31	40.27	0.73	1.43	1237.27	Normal							Normal	Normal
15	335.14	39.23	0.74	1.50	1170.89	Normal							Normal	Normal
16	319.41	38.87	0.77	1.17	1152.55	Normal							Normal	Normal
17	348.08	41.51	0.75	1.28	1328.80	Normal	369.16	39.50	0.67	1.69	308.24	Normal	Normal	Normal
22	401.53	47.30	0.74	1.37	1777.59	Normal	359.73	36.33	0.66	1.39	283.35	Normal	Normal	Normal
23	349.97	42.04	0.76	1.30	1381.87	Abnormal	392.79	40.79	0.67	1.62	331.78	Normal	Abnormal	Abnormal
24	363.68	42.97	0.74	1.31	1429.69	Abnormal	365.69	37.60	0.67	1.59	285.37	Abnormal	Abnormal	Abnormal

(continues)

Table 5.8. HLA geometric dimensions of segmented structures and respective Bayesian classification results and comparison with clinical diagnosis (continuation).

Patient Number	Stress						Rest						Final Algorithm Classification	Clinical Diagnosis
	Perimeter	Equivalent Spherical Radius	Roundness	Elongation	Number of Pixels	Algorithm Classification	Perimeter	Equivalent Spherical Radius	Roundness	Elongation	Number of Pixels	Algorithm Classification		
25	329.51	40.53	0.77	1.31	1276.54	Normal	365.69	37.60	0.67	1.59	285.37	Abnormal	Abnormal	Abnormal
26	368.82	43.04	0.74	1.29	1442.60	Normal	356.21	38.10	0.67	1.72	290.12	Normal	Normal	Normal
27	368.44	42.62	0.73	1.37	1402.56	Normal	410.10	42.02	0.66	1.69	345.27	Normal	Normal	Normal
29	364.38	43.77	0.76	1.23	1499.87	Normal	356.46	36.51	0.71	1.53	265.74	Normal	Normal	Normal
31	324.42	38.78	0.75	1.22	1148.85	Normal	374.63	38.74	0.67	1.73	300.46	Normal	Normal	Normal
33	366.21	42.49	0.73	1.50	1381.55	Normal	397.11	40.09	0.65	1.77	316.30	Normal	Normal	Normal
35	346.40	41.42	0.75	1.30	1310.30	Normal	395.90	40.61	0.66	1.64	329.60	Normal	Normal	Abnormal
36	366.21	42.49	0.73	1.50	1381.55	Normal	389.09	39.71	0.66	1.66	317.30	Normal	Normal	Normal
37	333.76	40.92	0.77	1.36	1279.60	Normal	379.19	39.24	0.67	1.67	310.35	Normal	Normal	Normal
38	354.38	41.58	0.74	1.25	1360.35	Normal	376.00	38.86	0.67	1.59	303.82	Normal	Normal	Normal
39	340.86	40.54	0.75	1.23	1283.33	Normal	383.55	40.36	0.68	1.60	325.98	Normal	Normal	Abnormal
40	339.75	40.94	0.76	1.23	1312.09	Normal	340.64	38.30	0.76	1.74	281.56	Normal	Normal	Normal
42	359.38	43.75	0.76	1.26	1532.59	Normal	388.19	40.83	0.68	1.65	332.71	Normal	Normal	Normal
43	354.01	41.87	0.75	1.31	1373.94	Normal	388.48	39.97	0.67	1.69	316.23	Normal	Normal	Normal
44	337.00	40.00	0.75	1.30	1248.07	Normal	376.36	38.28	0.67	1.70	294.24	Normal	Normal	Normal
45	313.91	38.16	0.76	1.18	1132.00	Abnormal	370.16	39.18	0.68	1.71	307.28	Normal	Abnormal	Abnormal
46	351.56	41.73	0.75	1.34	1350.73	Normal	407.26	41.25	0.66	1.76	335.68	Normal	Normal	Normal
47	365.11	43.50	0.75	1.40	1476.71	Normal							Normal	Normal
48	342.93	42.53	0.78	1.48	1402.47	Normal							Normal	Normal
49	355.48	41.85	0.74	1.54	1334.09	Normal							Normal	Normal
50	349.36	41.00	0.74	1.50	1290.92	Normal	341.52	37.32	0.69	1.68	280.53	Abnormal	Abnormal	Abnormal
51	329.60	39.49	0.75	1.31	1192.36	Abnormal	340.05	37.44	0.69	1.62	281.84	Abnormal	Abnormal	Abnormal

(continues)

Table 5.8. HLA geometric dimensions of segmented structures and respective Bayesian classification results and comparison with clinical diagnosis (continuation).

Patient Number	Stress						Rest						Final Algorithm Classification	Clinical Diagnosis
	Perimeter	Equivalent Spherical Radius	Roundness	Elongation	Number of Pixels	Algorithm Classification	Perimeter	Equivalent Spherical Radius	Roundness	Elongation	Number of Pixels	Algorithm Classification		
52	362.61	42.84	0.79	1.34	1315.22	Normal							Normal	Normal
53	336.66	41.16	0.88	1.47	1125.60	Normal	373.77	39.55	0.76	1.85	285.08	Normal	Normal	Normal
54	320.30	37.83	0.74	1.28	1095.00	Abnormal	318.52	34.76	0.69	1.42	256.25	Abnormal	Abnormal	Abnormal
55	340.95	38.08	0.87	1.25	969.55	Normal	379.38	41.20	0.73	1.81	317.59	Normal	Normal	Abnormal
56	336.95	40.83	0.82	1.44	1193.05	Normal	356.33	39.14	0.74	1.78	291.63	Normal	Normal	Normal
57	352.33	42.82	0.82	1.22	1310.34	Normal							Normal	Normal
58	339.18	40.54	0.80	1.41	1169.05	Normal							Normal	Normal
59	349.92	41.69	0.80	1.44	1239.16	Normal							Normal	Normal
60	338.46	40.41	0.80	1.25	1163.38	Normal	356.03	39.28	0.74	1.64	292.59	Normal	Normal	Normal

Table 5.9 VLA geometric dimensions of segmented structures and respective Bayesian classification results and comparison with clinical diagnosis.

Patient Number	Stress						Rest						Final Algorithm Classification	Clinical Diagnosis
	Perimeter	Equivalent Spherical Radius	Roundness	Elongation	Number of Pixels	Algorithm Classification	Perimeter	Equivalent Spherical Radius	Roundness	Elongation	Number of Pixels	Algorithm Classification		
1	508.82	52.15	0.65	1.23	2074.92	Normal	298.45	25.90	0.55	1.47	509.92	Normal	Normal	Normal
2	479.70	51.78	0.68	1.23	2040.71	Normal	257.06	23.02	0.56	1.38	404.00	Abnormal	Abnormal	Abnormal
3	301.45	36.88	0.77	1.22	1039.89	Abnormal	278.67	25.96	0.59	1.47	514.27	Abnormal	Abnormal	Abnormal
4	491.78	55.74	3.18	1.65	2148.14	Normal	290.05	25.80	0.56	1.40	510.80	Normal	Normal	Normal
5	427.92	47.11	0.69	1.26	1715.54	Abnormal	265.61	23.06	0.55	1.39	406.38	Abnormal	Abnormal	Abnormal
6	519.66	53.00	0.64	1.19	2139.15	Normal							Normal	Normal
7	469.64	51.70	0.69	1.14	2036.50	Normal							Normal	Normal

(continues)

Table 5.9 VLA geometric dimensions of segmented structures and respective Bayesian classification results and comparison with clinical diagnosis (continuation).

Patient Number	Stress						Rest						Final Algorithm Classification	Clinical Diagnosis
	Perimeter	Equivalent Spherical Radius	Roundness	Elongation	Number of Pixels	Algorithm Classification	Perimeter	Equivalent Spherical Radius	Roundness	Elongation	Number of Pixels	Algorithm Classification		
8	468.67	52.65	0.71	1.25	2111.82	Normal							Normal	Normal
9	482.12	49.98	0.65	1.36	1904.25	Normal							Normal	Normal
10	485.64	53.01	0.73	1.23	1996.31	Normal							Normal	Normal
11	492.10	53.69	0.73	1.26	2049.46	Normal							Normal	Normal
12	484.49	52.32	0.68	1.11	2087.53	Normal							Normal	Normal
13	482.09	50.62	0.66	1.18	1954.09	Normal							Normal	Normal
14	476.58	49.97	0.66	1.19	1902.36	Normal							Normal	Normal
15	501.54	53.10	0.67	1.27	2157.92	Normal							Normal	Normal
16	512.68	56.21	0.79	1.47	2099.23	Normal							Normal	Normal
17	348.08	41.51	0.75	1.28	1328.80	Abnormal	298.45	25.90	0.55	1.47	509.92	Normal	Abnormal	Normal
22	521.26	52.83	0.64	1.24	2127.64	Normal	285.06	25.46	0.56	1.36	168.78	Normal	Normal	Normal
23	474.92	50.42	0.67	1.12	1935.67	Normal	279.90	24.90	0.56	1.38	164.75	Abnormal	Abnormal	Abnormal
24	530.08	51.73	0.62	1.23	2042.73	Normal	274.98	24.26	0.55	1.44	160.04	Abnormal	Abnormal	Abnormal
25	475.79	52.00	0.69	1.21	2056.75	Normal	269.66	23.78	0.55	1.36	156.50	Abnormal	Abnormal	Abnormal
26	473.87	49.95	0.66	1.21	1898.09	Normal	290.63	25.65	0.56	1.39	171.28	Normal	Normal	Normal
27	496.35	51.22	0.65	1.31	1995.27	Normal	303.37	26.30	0.54	1.47	175.92	Normal	Normal	Normal
29	512.61	54.32	0.67	1.16	2260.87	Normal	234.17	21.02	0.56	1.31	138.52	Normal	Normal	Normal
31	492.72	52.95	0.72	1.17	1993.82	Normal	291.87	26.61	0.61	1.48	176.04	Normal	Normal	Normal
33	550.17	55.24	0.63	1.38	2330.62	Abnormal	290.16	25.66	0.56	1.45	171.17	Normal	Abnormal	Normal
35	538.86	55.01	0.64	1.20	2165.03	Abnormal	278.36	24.23	0.55	1.32	160.04	Normal	Abnormal	Abnormal
36	550.17	55.24	0.63	1.38	2330.62	Abnormal	272.21	23.90	0.55	1.26	157.51	Normal	Abnormal	Normal

(continues)

Table 5.9 VLA geometric dimensions of segmented structures and respective Bayesian classification results and comparison with clinical diagnosis (continuation).

Patient Number	Stress						Rest						Final Algorithm Classification	Clinical Diagnosis
	Perimeter	Equivalent Spherical Radius	Roundness	Elongation	Number of Pixels	Algorithm Classification	Perimeter	Equivalent Spherical Radius	Roundness	Elongation	Number of Pixels	Algorithm Classification		
37	485.82	50.81	0.66	1.28	1965.00	Normal	276.95	24.91	0.57	1.30	165.23	Abnormal	Abnormal	Normal
38	517.84	53.95	0.66	1.20	2222.94	Normal	269.60	23.85	0.56	1.31	157.49	Normal	Normal	Normal
39	459.06	49.96	0.68	1.18	1904.00	Abnormal	272.68	24.28	0.56	1.30	160.38	Normal	Abnormal	Abnormal
40	464.82	52.64	0.71	1.13	2114.00	Abnormal	271.60	24.11	0.56	1.28	159.25	Normal	Abnormal	Normal
42	488.79	52.18	0.72	1.20	1933.30	Normal	279.34	25.05	0.56	1.41	165.93	Normal	Normal	Normal
43	492.38	53.24	0.73	1.21	2019.77	Normal	274.66	24.33	0.56	1.32	160.95	Normal	Normal	Normal
44	492.38	53.24	0.73	1.21	2019.77	Normal	286.08	25.02	0.55	1.52	165.68	Normal	Normal	Normal
45	417.66	46.56	0.70	1.25	1649.82	Abnormal	275.08	25.50	0.58	1.38	169.56	Abnormal	Abnormal	Abnormal
46	460.77	49.16	0.67	1.17	1840.67	Abnormal	288.82	25.32	0.55	1.39	168.95	Normal	Abnormal	Normal
47	467.12	52.06	0.70	1.19	1950.75	Normal							Normal	Normal
48	494.45	54.37	0.69	1.22	2259.19	Normal							Normal	Normal
49	506.97	53.03	0.70	1.28	2001.19	Normal							Normal	Normal
50	524.33	52.89	0.64	1.21	2129.54	Normal	290.90	25.75	0.56	1.46	508.31	Normal	Normal	Abnormal
51	444.27	53.38	0.70	1.44	2026.66	Abnormal	279.81	24.89	0.56	1.45	472.46	Abnormal	Abnormal	Abnormal
52	505.41	53.17	0.66	1.17	2154.58	Normal							Normal	Normal
53	488.75	51.80	0.67	1.08	2051.17	Normal	294.92	26.38	0.60	1.37	495.99	Normal	Normal	Normal
54	502.57	53.96	0.68	1.17	2219.37	Normal	244.83	22.03	0.57	1.34	369.31	Abnormal	Abnormal	Abnormal
55	427.57	46.11	0.73	1.43	1511.17	Normal	287.00	26.50	0.58	1.33	535.00	Normal	Normal	Normal
56	490.36	52.51	0.67	1.17	2104.20	Normal	299.45	26.54	0.60	1.57	501.25	Normal	Normal	Normal
57	487.73	52.36	0.72	1.30	1949.30	Normal							Normal	Normal
58	489.04	52.19	0.67	1.13	2073.14	Normal							Normal	Normal

(continues)

Table 5.9 VLA geometric dimensions of segmented structures and respective Bayesian classification results and comparison with clinical diagnosis (continuation).

Patient Number	Stress						Rest						Final Algorithm Classification	Clinical Diagnosis
	Perimeter	Equivalent Spherical Radius	Roundness	Elongation	Number of Pixels	Algorithm Classification	Perimeter	Equivalent Spherical Radius	Roundness	Elongation	Number of Pixels	Algorithm Classification		
59	495.31	54.25	0.74	1.26	2091.85	Normal							Normal	Normal
60	472.95	51.18	0.68	1.10	1996.91	Normal	292.74	26.53	0.61	1.34	502.08	Normal	Normal	Normal

Table 5.10. SA geometric dimensions of segmented structures and respective Bayesian classification results and comparison with clinical diagnosis.

Patient Number	Stress						Rest						Final Algorithm Classification	Clinical Diagnosis
	Perimeter	Equivalent Spherical Radius	Roundness	Elongation	Number of Pixels	Algorithm Classification	Perimeter	Equivalent Spherical Radius	Roundness	Elongation	Number of Pixels	Algorithm Classification		
1	397.03	30.32	0.48	1.22	225.54	Normal	384.64	25.74	0.42	1.20	507.80	Normal	Normal	Normal
2	454.49	34.16	0.47	1.13	264.03	Normal	355.12	24.15	0.43	1.26	445.65	Abnormal	Abnormal	Abnormal
3	385.89	28.96	0.48	1.16	207.52	Abnormal	398.84	26.47	0.42	1.08	534.07	Normal	Abnormal	Abnormal
4	507.49	37.63	0.47	1.21	301.12	Normal	425.40	29.02	0.43	1.28	660.29	Normal	Normal	Normal
5	296.01	23.55	0.50	1.11	160.15	Abnormal	333.98	23.03	0.43	1.23	403.36	Abnormal	Abnormal	Abnormal
6	404.03	30.17	0.55	1.33	212.87	Normal							Normal	Normal
7	455.60	33.55	0.46	1.18	253.50	Normal							Normal	Normal
8	459.33	34.05	0.47	1.17	262.51	Normal							Normal	Normal
9	400.45	31.51	0.53	1.28	224.27	Normal							Normal	Normal
10	401.58	30.46	0.48	1.09	225.26	Normal							Normal	Normal
11	412.60	31.69	0.48	1.15	233.35	Normal							Normal	Normal
12	417.43	30.67	0.46	1.20	225.12	Normal							Normal	Normal
13	409.49	31.54	0.63	1.37	219.02	Normal							Normal	Normal
14	415.96	31.50	0.55	1.29	222.99	Normal							Normal	Normal

(continues)

Table 5.10. SA geometric dimensions of segmented structures and respective Bayesian classification results and comparison with clinical diagnosis (continuation).

Patient Number	Stress						Rest						Final Algorithm Classification	Clinical Diagnosis
	Perimeter	Equivalent Spherical Radius	Roundness	Elongation	Number of Pixels	Algorithm Classification	Perimeter	Equivalent Spherical Radius	Roundness	Elongation	Number of Pixels	Algorithm Classification		
15	460.35	32.56	0.45	1.43	243.57	Normal							Normal	Normal
16	416.10	32.37	0.49	1.19	243.04	Normal							Normal	Normal
17	406.27	31.33	0.48	1.22	234.72	Normal	384.64	25.74	0.42	1.20	507.80	Normal	Normal	Normal
22	512.05	37.26	0.46	1.29	297.46	Normal	418.45	27.82	0.42	1.13	596.82	Normal	Normal	Normal
23	418.13	31.84	0.48	1.16	237.11	Normal	394.41	26.24	0.42	1.18	530.12	Normal	Normal	Abnormal
24	398.16	29.60	0.47	1.26	213.05	Normal	384.87	25.85	0.42	1.21	510.13	Abnormal	Abnormal	Abnormal
25	489.31	36.09	0.46	1.26	279.47	Normal	416.92	27.67	0.42	1.22	586.65	Normal	Normal	Abnormal
26	426.14	32.14	0.48	1.13	241.15	Normal	394.00	26.51	0.45	1.27	499.79	Normal	Normal	Normal
27	342.76	26.95	0.49	1.08	187.99	Abnormal	392.91	27.18	0.51	1.39	480.51	Normal	Abnormal	Normal
29	502.02	34.66	0.45	1.29	268.89	Normal	389.55	26.95	0.50	1.38	476.40	Normal	Normal	Normal
31	406.96	30.26	0.47	1.13	223.17	Normal	395.34	26.44	0.42	1.14	531.85	Normal	Normal	Normal
33	480.71	34.55	0.46	1.45	267.20	Normal	401.91	26.49	0.42	1.24	539.00	Normal	Normal	Normal
35	453.11	33.50	0.47	1.21	257.81	Normal	410.73	27.53	0.42	1.14	585.41	Normal	Normal	Abnormal
36	480.71	34.55	0.46	1.45	267.20	Normal	399.12	27.02	0.43	1.17	563.41	Normal	Normal	Normal
37	390.25	31.03	0.50	1.20	221.87	Abnormal	387.20	26.09	0.42	1.17	184.19	Normal	Abnormal	Normal
38	495.26	36.15	0.46	1.20	285.89	Normal	405.51	27.42	0.46	1.23	193.51	Normal	Normal	Normal
39	401.02	30.04	0.47	1.15	219.09	Abnormal	373.65	25.27	0.43	1.21	176.94	Abnormal	Abnormal	Abnormal
40	405.33	31.68	0.49	1.11	232.24	Normal	362.77	24.48	0.42	1.17	455.82	Abnormal	Abnormal	Normal
42	444.57	32.54	0.47	1.16	249.22	Normal	406.77	26.98	0.42	1.19	558.18	Normal	Normal	Normal
43	443.78	32.31	0.46	1.09	245.97	Normal	409.70	27.63	0.45	1.29	544.99	Normal	Normal	Normal
44	371.28	28.71	0.52	1.15	202.48	Normal	409.52	27.44	0.42	1.23	573.38	Normal	Normal	Normal
45	397.18	29.97	0.48	1.21	216.50	Abnormal	395.63	26.67	0.42	1.31	546.47	Normal	Abnormal	Abnormal

(continues)

Table 5.10. SA geometric dimensions of segmented structures and respective Bayesian classification results and comparison with clinical diagnosis (continuation).

Patient Number	Stress						Rest						Final Algorithm Classification	Clinical Diagnosis
	Perimeter	Equivalent Spherical Radius	Roundness	Elongation	Number of Pixels	Algorithm Classification	Perimeter	Equivalent Spherical Radius	Roundness	Elongation	Number of Pixels	Algorithm Classification		
46	426.22	31.48	0.47	1.24	233.52	Normal	378.90	26.90	0.42	1.13	492.34	Normal	Normal	Normal
47	475.62	34.92	0.46	1.30	268.97	Normal							Normal	Normal
48	467.22	33.92	0.46	1.33	260.68	Normal							Normal	Normal
49	458.93	34.75	0.48	1.19	260.06	Normal							Normal	Normal
50	381.71	30.46	0.50	1.14	217.35	Abnormal	371.37	25.25	0.43	1.20	486.38	Abnormal	Abnormal	Abnormal
51	380.53	30.35	0.50	1.18	220.38	Abnormal	379.45	25.45	0.42	1.19	495.80	Normal	Abnormal	Abnormal
52	477.98	34.26	0.45	1.33	262.77	Normal							Normal	Normal
53	438.73	33.75	0.48	1.19	258.05	Normal	377.68	25.36	0.42	1.19	489.27	Normal	Normal	Normal
54	391.61	29.76	0.48	1.11	216.34	Abnormal	336.69	23.21	0.43	1.19	410.33	Abnormal	Abnormal	Abnormal
55	343.54	27.08	0.50	1.19	190.48	Abnormal	414.23	27.34	0.42	1.12	574.06	Normal	Abnormal	Normal
56	401.75	32.49	0.54	1.28	229.94	Normal	408.87	27.66	0.46	1.23	546.06	Normal	Normal	Normal
57	345.04	26.43	0.48	1.10	185.56	Abnormal							Abnormal	Normal
58	513.18	37.91	0.50	1.23	292.25	Normal							Normal	Normal
59	419.75	32.31	0.52	1.19	233.25	Normal							Normal	Normal
60	472.95	33.81	0.45	1.30	255.53	Normal	404.75	26.83	0.42	1.14	551.06	Normal	Normal	Normal

The classification algorithm was evaluated using the classes "abnormality present" and "abnormality not present". Considering that healthy patients must have healthy stress and rest myocardial perfusion SPECT images, while unhealthy patient have at least one of the exams with abnormal values, the confusion matrix obtained from classification results is presented in Table 5.11, containing the counting results of true positive (TP), false positive (FP), true negative (TN) and false negative (FN).

Table 5.11. Confusion matrix obtained from Bayesian classifier results.

		Algorithm decision	
		Abnormality present	Abnormality not present
Clinical decision	Abnormality present	30	13
	Abnormality not present	6	104

Additionally, the evaluation was completed by computing five parameters: sensitivity, specificity, precision, accuracy and mean error rate. From the table shown above, it is possible to calculate these parameters, which results can be observed in Table 5.12.

Table 5.12. Performance measures of the proposed classification method.

Measure	Performance values
Sensitivity	0.698
Specificity	0.945
Precision	0.833
Accuracy	0.876
Mean error rate	0.124

5.4. Discussion

The goal of this research was to perform a consistent and feasible registration of cardiac SPECT data sets to construct a template image and proceed to the LV segmentation. The final goal was to obtain geometric dimensions of a normal LV perfusion and perform a statistical analysis, to automatically classify patients as having a cardiac disease or not.

This dissertation proposes an automatic registration image method, developed for cardiac SPECT images, that builds a template image using a pre-registration method based on rigid transformation followed by a final registration

method based on deformable transformations. These sequential registration steps are fundamental to correct global deformations first and then solve local deformations.

Due to the high difference between the structures dimensions when dealing with male or female patients, it was hard to choose the components that could produce consistent results, namely the interpolator. In fact, linear interpolators were introducing undesirable deformations into the registered images. Therefore, a B-spline interpolator presented best results since it approximate shapes through curve fitting and interactive curve design.

Although metrics based on the information theory are more popular in deformable registration algorithms, their applications in several registration algorithms based on rigid transformations demonstrate that it is very permutable and adaptable to several transformations. For these reason, Mattes mutual information was used in the proposed registration algorithm. The template myocardial perfusion SPECT and its coronary artery mapping were visually validated.

Since cardiac SPECT images are not in the same intensity range and simultaneously they are characterized by weak boundaries, applying conventional techniques such as binary thresholding or gradient magnitude based segmentation techniques was not enough effective to produce acceptable results. As observed in section 5.3.2, beyond the approximated Dice's coefficient results of region growing, the employment of K-means clustering technique, using 3 clusters, has shown better results, with mean values of 0.80 and 0.69, respectively, both for comparison based on a student generated gold standard and clinical professional manual segmentation. These values are reasonable, but must be optimized to obtain the Dice's coefficient closer to the maximum value and, obviously, a more reliable segmentation.

The proposed method consists of a simple and efficient segmentation technique, starting by an image enhancement based on image averaging and morphological operations, simultaneously eliminating noise and making boundaries stronger. According the results shown in Table 5.6 and Table 5.7, k-means clustering is used to segment LV structure, which results are not distorted by hypertrophied right ventricle myocardium, retention of tracer in the lung(s) or breast activity. In fact, LV is well recognized in all slices and separated from right ventricle, as Figures 5.6-9 demonstrates. The boundaries of the segmented objects were well recognized,

through object labeling, as well as the related geometric dimensions and statistical analysis.

Mean values of each geometric dimension per axis are shown in Table 5.7., for stress and rest template image. These values are lower than from those shown in Tables 5.8-10. This is due to the fact that the template geometric dimensions consider all the template slices, from basal to apical region, while the other measures result from the segmentation of a set of slices already registered with the middle template coronary artery mapping slice, incrementing the mean geometric dimensions obtained. It does not considerably affect the classification results, since all slices were aligned with the same slice, resulting in a consisted proportion between the original patients' exams and the final geometric dimensions, as well as the defined classes use geometric dimensions of segmented structures obtained using the same methodology.

In section 5.3.3, the evaluation of Bayesian classification has indicated that the algorithm have a reasonable capacity of detect an abnormality where it actually exists, approximately equal to 70%. In the other hand, the false positive fraction, or the ability of the algorithm report healthy exam where there is no abnormality, rounds 95%. These values can be explained by the lower number of diseased patients, of which the test dataset used was composed, meaning a less consisted mean and standard deviation values, computed by the classification algorithm, when comparing with the number of healthy patients that constituted the training phase. Additionally, precision and accuracy parameters have demonstrated the capacity of 83% and 88%, respectively, presenting a relatively good classification performance concerning correct decisions and relevant detections.

However, a mean error rate of 12,4% leads to the necessity of optimize the entire algorithm, especially image registration of patient's exam and the template image, since it was visually evaluated, being more subjected to observer variability. This mean error rate is generally due to more extreme cases, which issue of deficient myocardial perfusion of bigger hearts or healthy perfusion of small hearts was not completely overwhelmed. Since a slightly misregistration can introduce undesirable deformations in the exam patient, LV geometric dimensions are affected and, consequently, the classifier is induced into a wrong report. Accordingly, the image registration technique here developed must be optimized to overcome this issue.

Respecting computer time-consuming, per patient and clinical protocol, i.e., per set of HLA, VLA and SA images in a single clinical study (stress or rest), the mean processing time was approximated to 8 minutes. However, this value is affected by the reduced processor power of the computer used to develop this computational solution.

5.5. Conclusions

To the best of our knowledge, there is no template SPECT image reported in scientific literature, so there was the need of build it. A pre-registration technique based on rigid transformation followed by a registration technique based on deformable transformations was developed, resulting in both stress and rest template myocardial perfusion SPECT images, for SA, HLA and VLA. The coronary artery mapping was manually performed and registered with the template myocardial perfusion SPECT image, aiming to ease the identification of extent and location of the myocardial perfusion defects.

Segmenting the LV structure is a crucial and challenging task in nuclear medicine imaging analysis which is required to detect cardiac abnormalities. An automatic method using k-means clustering technique (three clusters) was validated through the Dice's coefficient. The obtained results shown well segmented structures with all of the data set used, including coronary artery mapping regions, but must be optimized to augment the Dice's coefficient closer to the maximum value. However, this method has already shown a robust behavior for noisy and low-resolution data, with capabilities to overcome nearby interfering activities.

The results have shown the computational solution effective, especially due to the registration of female and male cardiac SPECT images, which can have very different structures dimensions. The proposed method demonstrates reasonable robustness against the two major difficulties in SPECT image processing, noise and low level details, through an automatic computational technique. Hence, the classifier here employed has demonstrated good specificity and accuracy values but image registration algorithm has to be optimized, since it is fundamental to augment sensitivity value and reduce the mean error ratio, as well as the computer processing time.

Chapter 6

Final considerations

6.1. Final conclusions

Most current algorithms for medical image registration use rigid body transformations or affine transformations, but they are restricted to parts of the body where tissue deformation is small compared with the desired registration accuracy. Some examples are the combination of functional and high resolution anatomical information as an aid to diagnosis with better localization and determination of extent of abnormalities, planning treatment and surgeries.

The higher incidence of heart diseases in world population, and consequently one of the major death factors worldwide, requires medical diagnosis to be faster and more efficient. Therefore, an automatic method to analyze normal myocardial perfusion SPECT images, through registration methods, is fundamental to summarize their features and ease a correct diagnosis, enhancing the monitoring of changes due to disease progression and response to treatments.

For this reason, it was build both template stress and rest myocardial perfusion SPECT images and their coronary artery mapping. Pre-processing image techniques, specifically image intensity normalization and B-spline interpolation were fundamental to normalize the images to be registered. Then, pre-registration based on rigid transforms and registration based on deformable transforms, both using multi-resolution registration techniques, were applied as registration

framework, since they solve global and local deformations sequentially through a faster and efficient algorithm. These methods enabled the formation of a template myocardial perfusion SPECT image and its coronary artery mapping.

Segmentation algorithm validation was performed using Dice's coefficient. The comparison of segmented images using ITK automatic segmentation method, Otsu method (3 levels), k-means (3 clusters), region growing and level set methods, against two different gold standards demonstrated k-means as the most robust method. Besides this segmentation method, post-processing image techniques were used. Noise and low level details were overwhelmed and LV segmentation was not distorted by hypertrophied right ventricle myocardium or retention of tracer in the lung(s) or breast activity. However, Dice's coefficient values of 0.80 and 0.69 means the segmentation methods needs to be optimized.

Hereafter, the computational solution presented, consisting on (1) the segmentation of medical patient's exams, (2) respective registration with template SPECT image, (3) computation of related geometric dimensions, (4) statistical analysis and its classification based on Bayesian theory, demonstrated reasonable robustness. Sensitivity value of 70% and mean error ratio of 12,4% leads to the necessity of optimize the registration and classification methods used. Precision and accuracy parameters have demonstrated the capacity of 83% and 88%, such as specificity presented a performance measure of 95%. Thus, it was presented a good classification performance concerning correct decisions and relevant detections.

6.2. Future works

The continuous development and optimization of this computational solution with higher values of classifier evaluation is the priority objective. It is pretended to realize more extensive experimentation of different registration components and respective parameter values, to optimize registration methods. Additionally, image dataset must be augmented to a bigger number of patients, with higher inter-variability.

Besides the optimization of registration and segmentation techniques used and the reduction of computer processing-time, there are several aspects that can be introduced in this computational solution such as: (1) computation of 3-D coronary artery mapping of template myocardial perfusion and 3-D registration with

patient's exams, (2) generating more relevant information as detect the myocardial perfusion disease, (3) informing the clinical professional about the defect percentage of myocardial perfusion for each exam, when compared to template myocardial perfusion uptake ratio, (4) integrate image registration results with electrocardiographic signals, (5) modeling the registered images in 3-D to provide a better visual evaluation and (6) develop a user guide interface.

Therefore, it is pretended to contribute to a mathematical grounded and effective diagnosis, monitoring of disease development such as planning of treatments or surgeries. This computational solution will become both physician and medical activity easier and more efficient, through the development, optimization, test, use, comparison and validation of the developed algorithms.

References

1. ZANZONICO, Pat. Basic sciences of nuclear medicine. Heidelberg: Springer, 2011.

2. MUEHLLEHNER, Gerd; KARP, Joel S. Positron emission tomography. Physics in medicine and biology, 2006, 51.13: R117.

3. JASZCZAK, Ronald Jack. The early years of single photon emission computed tomography (SPECT): an anthology of selected reminiscences. Physics in medicine and biology, 2006, 51.13: R99.

4. PIMLOTT, Sally L.; SUTHERLAND, Andrew. Molecular tracers for the PET and SPECT imaging of disease. Chemical Society Reviews, 2011, 40.1: 149-162.

5. MEYER, Jeffrey H.; ICHISE, Masanori. Modeling of receptor ligand data in PET and SPECT imaging: a review of major approaches. Journal of Neuroimaging, 2001, 11.1: 30-39.

6. KHALIL, Magdy M., et al. Molecular SPECT imaging: an overview. International journal of molecular imaging, 2011, 2011.

7. JASZCZAK, RONALD J.; COLEMAN, R. EDWARD. Single photon emission computed tomography (SPECT) principles and instrumentation. Investigative radiology, 1985, 20.9: 897-910.

8. RAHMIM, Arman. PET vs. SPECT: in the context of ongoing developments. Iranian Journal of Nuclear Medicine, 2006, 14.1: 1-20.

9. RAHMIM, Arman; ZAIDI, Habib. PET versus SPECT: strengths, limitations and challenges. Nuclear medicine communications, 2008, 29.3: 193-207.

10. HUTTON, Brian F.; BUVAT, Irene; BEEKMAN, Freek J. Review and current status of SPECT scatter correction. Physics in medicine and biology, 2011, 56.14: R85.

11. SPANOUDAKI, Virginia C.; ZIEGLER, Sibylle I. PET & SPECT Instrumentation. In: Molecular Imaging I. Springer Berlin Heidelberg, 2008. p. 53-74.

12. DEPUEY, E. Gordon. Advances in SPECT camera software and hardware: currently available and new on the horizon. Journal of nuclear cardiology, 2012, 19.3: 551-581.

13. PETERSON, Todd E.; FURENLID, Lars R. SPECT detectors: the Anger Camera and beyond. Physics in medicine and biology, 2011, 56.17: R145.

14. BRANDERHORST, Woutjan, et al. Targeted multi-pinhole SPECT. European journal of nuclear medicine and molecular imaging, 2011, 38.3: 552-561.

15. KHERUKA, S. C., et al. A study to improve the image quality in low-dose computed tomography (SPECT) using filtration. Indian journal of nuclear medicine: IJNM: the official journal of the Society of Nuclear Medicine, India, 2011, 26.1: 14.

16. O'CONNOR, Michael K.; KEMP, Brad J. Single-photon emission computed tomography/computed tomography: basic instrumentation and innovations. In: Seminars in nuclear medicine. WB Saunders, 2006. p. 258-266.

17. ROSENTHAL, M. S., et al. Quantitative SPECT imaging: a review and recommendations by the Focus Committee of the Society of Nuclear Medicine Computer and Instrumentation Council. Journal of nuclear medicine: official publication, Society of Nuclear Medicine, 1995, 36.8: 1489-1513.

18. RITT, Philipp, et al. Absolute quantification in SPECT. European journal of nuclear medicine and molecular imaging, 2011, 38.1: 69-77.

19. HINES, Horace, et al. National Electrical Manufacturers Association recommendations for implementing SPECT instrumentation quality control. Journal of Nuclear Medicine, 2000, 41.2: 383-389.

20. VANDENBERGHE, Stefaan, et al. Iterative reconstruction algorithms in nuclear medicine. Computerized Medical Imaging and Graphics, 2001, 25.2: 105-111.

21. ZANZONICO, Pat. Routine quality control of clinical nuclear medicine instrumentation: a brief review. Journal of Nuclear Medicine, 2008, 49.7: 1114-1131.

22. SERET, Alain; FORTHOMME, Julien. Comparison of different types of commercial filtered backprojection and ordered-subset expectation maximization SPECT reconstruction software. Journal of nuclear medicine technology, 2009, 37.3: 179-187.

23. Erwin, W. SPECT / CT Instrumentation and Clinical Applications. University of Texas, M. D. Aderson Cancer Center. Online. Available in <http://www.aapm.org/meetings/amos2/pdf/35-9913-56574-574.pdf>. Access at June 21th, 2013.

24. BOUCHARA, Frédéric; RAMDANI, Sofiane. Statistical behavior of edge detectors. Signal, Image and Video Processing, 2007, 1.3: 273-285.

25. JACENE, Heather A., et al. Advantages of Hybrid SPECT/CT vs SPECT alone. Open Med Imag J, 2008, 13.2: 67-79.

26. YANG, Feng, et al. Emerging inorganic nanomaterials for pancreatic cancer diagnosis and treatment. Cancer treatment reviews, 2012, 38.6: 566-579.

27. DEFRISE, M. A short reader's guide to 3D tomographic reconstruction. Computerized Medical Imaging and Graphics, 2001, 25.2: 113-116.

28. PFLUGER, Thomas, et al. Quantitative Comparison of Automatic and Interactive Methods for MRI–SPECT Image Registration of the Brain Based on 3-Dimensional Calculation of Error. Journal of Nuclear Medicine, 2000, 41.11: 1823-1829.

29. STOKKING, Rik, et al. Normal fusion for three-dimensional integrated visualization of SPECT and magnetic resonance brain images. Journal of Nuclear Medicine, 1997, 38.4: 624-629.

30. AZMAN, S., et al. A nuclear radiation detector system with integrated readout for SPECT/MR small animal imaging. In: Nuclear Science Symposium Conference Record, 2007. NSS'07. IEEE. IEEE, 2007. p. 2311-2317.

31. BRETON, E., et al. Dual SPECT/MR imaging in small animal. Nuclear Instruments and Methods in Physics Research Section A: Accelerators, Spectrometers, Detectors and Associated Equipment, 2007, 571.1: 446-448.

32. BHARGAVA, P., He, G., Samarghandi, A., & Delpassand, E. S. Pictorial review of SPECT/CT imaging applications in clinical nuclear medicine. American journal of nuclear medicine and molecular imaging, 2012, 2(2), 221–31.

33. CHOW, Patrick L., et al. A method of image registration for small animal, multi-modality imaging. Physics in medicine and biology, 2006, 51.2: 379.

34. FRANC, Benjamin L., et al. Small-animal SPECT and SPECT/CT: important tools for preclinical investigation. Journal of Nuclear Medicine, 2008, 49.10: 1651-1663.

35. CHERRY, Simon R. Multimodality imaging: Beyond pet/ct and spect/ct. In: Seminars in nuclear medicine. WB Saunders, 2009. p. 348-353.

36. BRANDON, David, et al. The role of single-photon emission computed tomography and SPECT/computed tomography in oncologic imaging. In: Seminars in oncology. WB Saunders, 2011. p. 87-108.

37. KAUR, Sukhwinder, et al. Recent trends in antibody-based oncologic imaging. Cancer letters, 2012, 315.2: 97-111.

38. PURI, Basant K., et al. SPECT neuroimaging in schizophrenia with religious delusions. International Journal of Psychophysiology, 2001, 40.2: 143-148.

39. MATSUDA, Hiroshi. Role of neuroimaging in Alzheimer's disease, with emphasis on brain perfusion SPECT. Journal of Nuclear Medicine, 2007, 48.8: 1289-1300.

40. GODAU, Jana, et al. Neuroimaging: Current role in detecting pre-motor Parkinson's disease. Movement Disorders, 2012, 27.5: 634-643.

41. MAEHARA, Taketoshi. Neuroimaging of epilepsy. Neuropathology, 2007, 27.6: 585-593.

42. GRACELY, Richard H.; AMBROSE, Kirsten R. Neuroimaging of fibromyalgia. Best practice & research Clinical rheumatology, 2011, 25.2: 271-284.

43. DEL CASALE, A., et al. Functional neuroimaging in obsessive-compulsive disorder. Neuropsychobiology, 2011, 64.2: 61-85.

44. BORGHESANI, Paul R., et al. Neuroimaging in the clinical diagnosis of dementia: observations from a memory disorders clinic. Journal of the American Geriatrics Society, 2010, 58.8: 1453-1458.

45. MILLER, Bruce L.; GEARHART, Rosalie. Neuroimaging in the diagnosis of frontotemporal dementia. Dementia and geriatric cognitive disorders, 1999, 10.Suppl. 1: 71-74.

46. BOOIJ, Jan, et al. Imaging of striatal dopamine transporters in rat brain with single pinhole SPECT and co-aligned MRI is highly reproducible. Nuclear medicine and biology, 2003, 30.6: 643-649.

47. GOETZ, Christian, et al. SPECT low-field MRI system for small-animal imaging. Journal of Nuclear Medicine, 2008, 49.1: 88-93.

48. BAILEY, Dale L.; WILLOWSON, Kathy P. An evidence-based review of quantitative SPECT imaging and potential clinical applications. Journal of Nuclear Medicine, 2013, 54.1: 83-89.

49. BHARGAVA, Peeyush, et al. Pictorial review of SPECT/CT imaging applications in clinical nuclear medicine. American journal of nuclear medicine and molecular imaging, 2012, 2.2: 221.

50. MARIANI, Giuliano, et al. A review on the clinical uses of SPECT/CT. European journal of nuclear medicine and molecular imaging, 2010, 37.10: 1959-1985.

51. LU, Wentong, et al. Gold nano-popcorn-based targeted diagnosis, nanotherapy treatment, and in situ monitoring of photothermal therapy response of prostate cancer cells using surface-enhanced Raman spectroscopy. Journal of the American Chemical Society, 2010, 132.51: 18103-18114.

52. RAYLMAN, Raymond R., et al. Quantification of radiotracer uptake with a dedicated breast PET imaging system. Medical physics, 2008, 35.11: 4989-4997.

53. AMBROSINI, Valentina, et al. PET/CT imaging in different types of lung cancer: an overview. European journal of radiology, 2012, 81.5: 988-1001.

54. WU, Yen-Wen, et al. Comparison of contrast-enhanced MRI with 18F-FDG PET/201Tl SPECT in dysfunctional myocardium: relation to early functional outcome after surgical revascularization in chronic ischemic heart disease. Journal of Nuclear Medicine, 2007, 48.7: 1096-1103.

55. HACHAMOVITCH, Rory, et al. Comparison of the short-term survival benefit associated with revascularization compared with medical therapy in patients with no prior coronary artery disease undergoing stress myocardial perfusion single photon emission computed tomography. Circulation, 2003, 107.23: 2900-2907.

56. BOUDRAA, A., et al. Automated detection of the left ventricular region in gated nuclear cardiac imaging. Biomedical Engineering, IEEE Transactions on, 1996, 43.4: 430-436.

57. MILLER, D. Douglas, et al. Correlation of pharmacological 99mTc-sestamibi myocardial perfusion imaging with poststenotic coronary flow reserve in patients with angiographically intermediate coronary artery stenoses. Circulation, 1994, 89.5: 2150-2160.

58. BAXTER, Caroline G.; BOON, Nicolas A.; WALKER, James D. Detection of Silent Myocardial Ischemia in Asymptomatic Diabetic Subjects The DIAD study. Diabetes care, 2005, 28.3: 756-757.

59. ARAUJO, Luis I., et al. Noninvasive quantification of regional myocardial blood flow in coronary artery disease with oxygen-15-labeled carbon dioxide inhalation and positron emission tomography. Circulation, 1991, 83.3: 875-885.

60. ZHAO, Xiclo-Ming, et al. Nitrogen-13-ammonia and PET to detect allograft coronary artery disease after heart transplantation: comparison with coronary angiography. Journal of nuclear medicine: official publication, Society of Nuclear Medicine, 1995, 36.6: 982-987.

61. BONOW, R. O., et al. Identification of viable myocardium in patients with chronic coronary artery disease and left ventricular dysfunction. Comparison of thallium scintigraphy with reinjection and PET imaging with 18F-fluorodeoxyglucose. Circulation, 1991, 83.1: 26-37.

62. CATAFAU, Ana M.; TOLOSA, Eduardo. Impact of dopamine transporter SPECT using 123I-Ioflupane on diagnosis and management of patients with clinically uncertain parkinsonian syndromes. Movement Disorders, 2004, 19.10: 1175-1182.

63. BOOIJ, Jan; KNOL, Remco JJ. SPECT imaging of the dopaminergic system in (premotor) Parkinson's disease. Parkinsonism & related disorders, 2007, 13: S425-S428.

64. MATSUI, Hideaki, et al. Excessive daytime sleepiness in Parkinson disease: a SPECT study. SLEEP-NEW YORK THEN WESTCHESTER-, 2006, 29.7: 917.

65. CONTIN, Manuela, et al. Dopamine transporter gene polymorphism, spect imaging, and levodopa response in patients with Parkinson disease. Clinical neuropharmacology, 2004, 27.3: 111-115.

66. SIDEROWF, A., et al. [99mTc] TRODAT-1 SPECT imaging correlates with odor identification in early Parkinson disease. Neurology, 2005, 64.10: 1716-1720.

67. SURASI, Devaki Shilpa, et al. Dopamine Transporter SPECT Imaging in Parkinson Disease and Dementia. PET Clinics, 2013, 8.4: 459-467.

68. SEIBYL, John P. SPECT and PET in Atypical Parkinsonism. PET Clinics, 2010, 5.1: 65-74.

69. KÄGI, Georg; BHATIA, Kailash P.; TOLOSA, Eduardo. The role of DAT-SPECT in movement disorders. Journal of Neurology, Neurosurgery & Psychiatry, 2010, 81.1: 5-12.

70. BUCKNER, Randy L., et al. Molecular, structural, and functional characterization of Alzheimer's disease: evidence for a relationship between default activity, amyloid, and memory. The Journal of Neuroscience, 2005, 25.34: 7709-7717.

71. RYDING, E. SPECT measurements of brain function in dementia; a review. Acta Neurologica Scandinavica, 1996, 94.s168: 54-58.

72. FUNG, Glenn; STOECKEL, Jonathan. SVM feature selection for classification of SPECT images of Alzheimer's disease using spatial information. Knowledge and Information Systems, 2007, 11.2: 243-258.

73. OLIVEIRA, Francisco PM; TAVARES, Joao Manuel RS. Medical image registration: a review. Computer methods in biomechanics and biomedical engineering, 2014, 17.2: 73-93.

74. LA FOUGERE, C., et al. PET and SPECT in epilepsy: a critical review. Epilepsy & Behavior, 2009, 15.1: 50-55.

75. BADIAVAS, Kosmas, et al. SPECT imaging evaluation in movement disorders: far beyond visual assessment. European journal of nuclear medicine and molecular imaging, 2011, 38.4: 764-773.

76. GERASIMOU, George P., et al. Molecular imaging (SPECT and PET) in the evaluation of patients with movement disorders. Nuclear Medicine Review, 2006, 9.2: 147-153.

77. MASCALCHI, Mario; VELLA, Alessandra; CERAVOLO, Roberto. Movement disorders: role of imaging in diagnosis. Journal of magnetic resonance imaging, 2012, 35.2: 239-256.

78. SHARIR, Tali, et al. A new algorithm for the quantitation of myocardial perfusion SPECT. II: validation and diagnostic yield. Journal of Nuclear Medicine, 2000, 41.4: 720-727.

79. PAUL, Asit K.; NABI, Hani A. Gated myocardial perfusion SPECT: basic principles, technical aspects, and clinical applications. Journal of nuclear medicine technology, 2004, 32.4: 179-187.

80. JOLLY, Marie-Pierre. Automatic segmentation of the left ventricle in cardiac MR and CT images. International Journal of Computer Vision, 2006, 70.2: 151-163.

81. GERMANO, Guido, et al. Automatic quantification of ejection fraction from gated myocardial perfusion SPECT. Journal of Nuclear Medicine, 1995, 36.11: 2138.

82. CHUA, Terrance, et al. Gated technetium-99m sestamibi for simultaneous assessment of stress myocardial perfusion, postexercise regional ventricular function and myocardial viability: correlation with echocardiography and rest thallium-201 scintigraphy. Journal of the American College of Cardiology, 1994, 23.5: 1107-1114.

83. HILTON, Thomas C., et al. Technetium-99m sestamibi myocardial perfusion imaging in the emergency room evaluation of chest pain. Journal of the American College of Cardiology, 1994, 23.5: 1016-1022.

84. ROZANSKI, Alan, et al. Development and application of normal limits for left ventricular ejection fraction and volume measurements from 99mTc-sestamibi myocardial perfusion gates SPECT. Journal of nuclear medicine: official publication, Society of Nuclear Medicine, 2000, 41.9: 1445-1450.

85. FATHALA, Ahmed. Myocardial perfusion single photon computed tomography: An Atlas. Journal of the Saudi Heart Association, 2011, 23.2: 107-122.

86. HOSNTALAB, Mohammad, et al. Automatic left ventricle segmentation in volumetric SPECT data set by variational level set. International journal of computer assisted radiology and surgery, 2012, 7.6: 837-843.

87. SANTORO, Giovanni M., et al. Relation between ST-segment changes and myocardial perfusion evaluated by myocardial contrast echocardiography in patients with acute myocardial infarction treated with direct angioplasty. The American journal of cardiology, 1998, 82.8: 932-937.

88. GALLAGHER, K. P., et al. Significance of regional wall thickening abnormalities relative to transmural myocardial perfusion in anesthetized dogs. Circulation, 1980, 62.6: 1266-1274.

89. ROSS, J. Myocardial perfusion-contraction matching. Implications for coronary heart disease and hibernation. Circulation, 1991, 83.3: 1076-1083.

90. GARCIA, Ernest V., et al. The increasing role of quantification in clinical nuclear cardiology: the Emory approach. Journal of nuclear cardiology, 2007, 14.4: 420-432.

91. CERQUEIRA, Manuel D., et al. Standardized myocardial segmentation and nomenclature for tomographic imaging of the heart a statement for healthcare professionals from the cardiac imaging committee of the Council on Clinical Cardiology of the American Heart Association. Circulation, 2002, 105.4: 539-542.

92. ROSS, J. Myocardial perfusion-contraction matching. Implications for coronary heart disease and hibernation. Circulation, 1991, 83.3: 1076-1083.

93. BEHLOUL, Faiza, et al. Neuro-fuzzy systems for computer-aided myocardial viability assessment. Medical Imaging, IEEE Transactions on, 2001, 20.12: 1302-1313.

94. GERMANO, Guido; KAVANAGH, Paul B.; BERMAN, Daniel S. An automatic approach to the analysis, quantitation and review of perfusion and function from myocardial perfusion SPECT images. The International Journal of Cardiac Imaging, 1997, 13.4: 337-346.

95. HACHAMOVITCH, Rory, et al. Incremental prognostic value of myocardial perfusion single photon emission computed tomography for the prediction of cardiac death differential stratification for risk of cardiac death and myocardial infarction. Circulation, 1998, 97.6: 535-543.

96. ITO, Hiroshi, et al. Lack of myocardial perfusion immediately after successful thrombolysis. A predictor of poor recovery of left ventricular function in anterior myocardial infarction. Circulation, 1992, 85.5: 1699-1705.

97. SHAW, Leslee J.; ISKANDRIAN, Ami E. Prognostic value of gated myocardial perfusion SPECT. Journal of nuclear cardiology, 2004, 11.2: 171-185.

98. SHARIR, Tali, et al. Prediction of myocardial infarction versus cardiac death by gated myocardial perfusion SPECT: risk stratification by the amount of stress-induced ischemia and the poststress ejection fraction. Journal of Nuclear Medicine, 2001, 42.6: 831-837.

99. FICARO, Edward P.; CORBETT, James R. Advances in quantitative perfusion SPECT imaging. Journal of nuclear Cardiology, 2004, 11.1: 62-70.

100. HUTTON, Brian F., et al. Image registration: an essential tool for nuclear medicine. European journal of nuclear medicine and molecular imaging, 2002, 29.4: 559-577.96.

101. RAO, Anil, et al. Spatial transformation of motion and deformation fields using nonrigid registration. Medical Imaging, IEEE Transactions on, 2004, 23.9: 1065-1076.

102. FOX, Jana L., et al. Does registration of PET and planning CT images decrease interobserver and intraobserver variation in delineating tumor volumes for non-small-cell lung cancer?. International Journal of Radiation Oncology* Biology* Physics, 2005, 62.1: 70-75.

103. GANSER, Klaus A., et al. A deformable digital brain atlas system according to Talairach and Tournoux. Medical Image Analysis, 2004, 8.1: 3-22.

104. MAINTZ, J. B.; VIERGEVER, Max A. A survey of medical image registration.Medical image analysis, 1998, 2.1: 1-36.

105. HILL, Derek LG, et al. Medical image registration. Physics in medicine and biology, 2001, 46.3: R1.

106. PLUIM, Josien PW; MAINTZ, JB Antoine; VIERGEVER, Max A. Image registration by maximization of combined mutual information and gradient information. In: Medical Image Computing and Computer-Assisted Intervention–MICCAI 2000. Springer Berlin Heidelberg, 2000. p. 452-461.

107. ZITOVA, Barbara; FLUSSER, Jan. Image registration methods: a survey.Image and vision computing, 2003, 21.11: 977-1000.

108. OLIVEIRA, Francisco PM, et al. Towards an efficient and robust foot classification from pedobarographic images. Computer methods in biomechanics and biomedical engineering, 2012, 15.11: 1181-1188.

109. HUTTON, Brian F.; BRAUN, Michael. Software for image registration: algorithms, accuracy, efficacy. In: Seminars in nuclear medicine. WB Saunders, 2003. p. 180-192.

110. VAN DEN ELSEN, Petra A.; POL, E.-JD; VIERGEVER, Max A. Medical image matching-a review with classification. Engineering in Medicine and Biology Magazine, IEEE, 1993, 12.1: 26-39.

111. ZHANG, Hui; FRITTS, Jason E.; GOLDMAN, Sally A. Image segmentation evaluation: A survey of unsupervised methods. computer vision and image understanding, 2008, 110.2: 260-280.

112. CRUM, William R.; HARTKENS, Thomas; HILL, D. L. G. Non-rigid image registration: theory and practice. 2014.

113. HOLDEN, Mark. A review of geometric transformations for nonrigid body registration. Medical Imaging, IEEE Transactions on, 2008, 27.1: 111-128.

114. GUO, Yujun, et al. Breast image registration techniques: a survey. Medical and Biological Engineering and Computing, 2006, 44.1-2: 15-26.

115. TOGA, Arthur W.; THOMPSON, Paul M. The role of image registration in brain mapping. Image and vision computing, 2001, 19.1: 3-24.

116. GHOLIPOUR, Ali, et al. Brain functional localization: a survey of image registration techniques. Medical Imaging, IEEE Transactions on, 2007, 26.4: 427-451.

117. MAKELA, Timo, et al. A review of cardiac image registration methods. Medical Imaging, IEEE Transactions on, 2002, 21.9: 1011-1021.

118. MAURER, Calvin R.; FITZPATRICK, J. Michael. A review of medical image registration. Interactive image-guided neurosurgery, 1993, 17.

119. DECLERCK, Jérôme, et al. Automatic registration and alignment on a template of cardiac stress and rest reoriented SPECT images. Medical Imaging, IEEE Transactions on, 1997, 16.6: 727-737.

120. LEE, Eunjung; GUNZBURGER, Max. An optimal control formulation of an image registration problem. Journal of mathematical imaging and vision, 2010, 36.1: 69-80.

121. SHAFIQUE, Khurram; SHAH, Mubarak. A noniterative greedy algorithm for multiframe point correspondence. Pattern Analysis and Machine Intelligence, IEEE Transactions on, 2005, 27.1: 51-65.

122. SHAPIRO, Larry S.; MICHAEL BRADY, J. Feature-based correspondence: an eigenvector approach. Image and vision computing, 1992, 10.5: 283-288.

123. LECLERC, Yvan G.; LUONG, Q.-Tuan; FUA, Pascal. Self-consistency and MDL: A paradigm for evaluating point-correspondence algorithms, and its application to detecting changes in surface elevation. International Journal of Computer Vision, 2003, 51.1: 63-83.

124. JOHNSON, Hans J.; CHRISTENSEN, Gary E. Consistent landmark and intensity-based image registration. Medical Imaging, IEEE Transactions on, 2002, 21.5: 450-461.

125. BETKE, Margrit, et al. Landmark detection in the chest and registration of lung surfaces with an application to nodule registration. Medical Image Analysis, 2003, 7.3: 265-281.

126. AUDETTE, Michel A.; FERRIE, Frank P.; PETERS, Terry M. An algorithmic overview of surface registration techniques for medical imaging. Medical Image Analysis, 2000, 4.3: 201-217.

127. POSTELNICU, Gheorghe; ZOLLEI, Lilla; FISCHL, Bruce. Combined volumetric and surface registration. Medical Imaging, IEEE Transactions on, 2009, 28.4: 508-522.

128. HERLINE, Alan J., et al. Surface registration for use in interactive, image-guided liver surgery. Computer Aided Surgery, 2000, 5.1: 11-17.

129. JIA, Jiaya; TANG, Chi-Keung. Tensor voting for image correction by global and local intensity alignment. Pattern Analysis and Machine Intelligence, IEEE Transactions on, 2005, 27.1: 36-50.

130. YANG, Miin-Shen; WU, Kuo-Lung. A similarity-based robust clustering method.Pattern Analysis and Machine Intelligence, IEEE Transactions on, 2004, 26.4: 434-448.

131. HURVITZ, Aviv; JOSKOWICZ, Leo. Registration of a CT-like atlas to fluoroscopic X-ray images using intensity correspondences. International journal of computer assisted radiology and surgery, 2008, 3.6: 493-504.

132. WU, C.; MURTHA, P. E.; JARAMAZ, B. Femur statistical atlas construction based on two-level 3D non-rigid registration. Computer Aided Surgery, 2009, 14.4-6: 83-99.

133. ZAGORCHEV, Lyubomir; GOSHTASBY, Ardeshir. A comparative study of transformation functions for nonrigid image registration. Image Processing, IEEE Transactions on, 2006, 15.3: 529-538.

134. BRONSTEIN, Alexander M.; BRONSTEIN, Michael M.; KIMMEL, Ron. Topology-invariant similarity of nonrigid shapes. International journal of computer vision, 2009, 81.3: 281-301.

135. BUDD, Chris, et al. Global non-rigid alignment of surface sequences.International Journal of Computer Vision, 2013, 102.1-3: 256-270.

136. KADYROV, Alexander; PETROU, Maria. Affine parameter estimation from the trace transform. Pattern Analysis and Machine Intelligence, IEEE Transactions on, 2006, 28.10: 1631-1645.

137. RAMSAY, Jim O., et al. Parameter estimation for differential equations: a generalized smoothing approach. Journal of the Royal Statistical Society: Series B (Statistical Methodology), 2007, 69.5: 741-796.

138. STEFANESCU, Radu; PENNEC, Xavier; AYACHE, Nicholas. Grid powered nonlinear image registration with locally adaptive regularization. Medical image analysis, 2004, 8.3: 325-342.

139. SORZANO, Carlos OS; THEVENAZ, Philippe; UNSER, Michael. Elastic registration of biological images using vector-spline regularization. Biomedical Engineering, IEEE Transactions on, 2005, 52.4: 652-663.

140. ANDREETTO, Marco; CORTELAZZO, Guido Maria; LUCCHESE, Luca. Frequency domain registration of computer tomography data. In: 3D Data Processing, Visualization and Transmission, 2004. 3DPVT 2004. Proceedings. 2nd International Symposium on. IEEE, 2004. p. 550-557.

141. LARREY-RUIZ, Jorge; VERDÚ-MONEDERO, Rafael; MORALES-SÁNCHEZ, Juan. A fourier domain framework for variational image registration. Journal of Mathematical Imaging and Vision, 2008, 32.1: 57-72.

142. OLIVEIRA, Francisco PM; PATAKY, Todd C.; TAVARES, João Manuel RS. Registration of pedobarographic image data in the frequency domain. Computer methods in biomechanics and biomedical engineering, 2010, 13.6: 731-740.

143. PAN, Wei; QIN, Kaihuai; CHEN, Yao. An adaptable-multilayer fractional Fourier transform approach for image registration. Pattern Analysis and Machine Intelligence, IEEE Transactions on, 2009, 31.3: 400-414.

144. GEFEN, Smadar, et al. Surface alignment of an elastic body using a multiresolution wavelet representation. Biomedical Engineering, IEEE Transactions on, 2004, 51.7: 1230-1241.

145. ROGERS, Mike; GRAHAM, Jim. Robust and accurate registration of 2-D electrophoresis gels using point-matching. Image Processing, IEEE Transactions on, 2007, 16.3: 624-635.

146. ŠERIFOVIĆ-TRBALIĆ, A., et al. Intensity-based elastic registration incorporating anisotropic landmark errors and rotational information.International journal of computer assisted radiology and surgery, 2009, 4.5: 463-468.

147. BAYRO-CORROCHANO, Eduardo; RIVERA-ROVELO, Jorge. The use of geometric algebra for 3D modeling and registration of medical data. Journal of Mathematical Imaging and Vision, 2009, 34.1: 48-60.

148. REYES-LOZANO, Leo; MEDIONI, Gerard; BAYRO-CARROCHANO, Eduardo. Registration of 2d points using geometric algebra and tensor voting. Journal of Mathematical Imaging and Vision, 2010, 37.3: 249-266.

149. FISCHER, Bernd; MODERSITZKI, Jan. A unified approach to fast image registration and a new curvature based registration technique. Linear Algebra and its applications, 2004, 380: 107-124.

150. KYBIC, Jan; UNSER, Michael. Fast parametric elastic image registration.Image Processing, IEEE Transactions on, 2003, 12.11: 1427-1442.

151. GROSLAND, Nicole M.; BAFNA, Ritesh; MAGNOTTA, Vincent A. Automated hexahedral meshing of anatomic structures using deformable registration.Computer methods in biomechanics and biomedical engineering, 2009, 12.1: 35-43.

152. TAGARE, Hemant D.; GROISSER, David; SKRINJAR, Oskar. Symmetric non-rigid registration: A geometric theory and some numerical techniques. Journal of Mathematical Imaging and Vision, 2009, 34.1: 61-88.

153. NIELSEN, Mads, et al. Brownian warps for non-rigid registration. Journal of Mathematical Imaging and Vision, 2008, 31.2-3: 221-231.

154. KLEIN, Stefan, et al. Adaptive stochastic gradient descent optimisation for image registration. International journal of computer vision, 2009, 81.3: 227-239.

155. BEUTEL, Jacob, et al. Handbook of Medical Imaging, Volume 3. Display and PACS. Washington, DC: SPIE Press, 2002.

156. HOFFER, Paul B. Difference Images Calculated from Ictal and Interictal Technetium-. 99m-HMPAO SPECIT Scans of Epilepsy. 1995.

157. PLUIM, Josien PW; MAINTZ, JB Antoine; VIERGEVER, Max A. Mutual-information-based registration of medical images: a survey. Medical Imaging, IEEE Transactions on, 2003, 22.8: 986-1004.

158. PLUIM, Josien PW; MAINTZ, JB Antoine; VIERGEVER, Max A. F-information measures in medical image registration. Medical Imaging, IEEE Transactions on, 2004, 23.12: 1508-1516.

159. MAES, Frederik, et al. Multimodality image registration by maximization of mutual information. Medical Imaging, IEEE Transactions on, 1997, 16.2: 187-198.

160. SEPPA, Mika. Continuous sampling in mutual-information registration. Image Processing, IEEE Transactions on, 2008, 17.5: 823-826.

161. OLIVEIRA, Francisco PM; TAVARES, João Manuel RS. Novel framework for registration of pedobarographic image data. Medical & biological engineering & computing, 2011, 49.3: 313-323.

162. COLLIGNON, André, et al. Automated multi-modality image registration based on information theory. In: Information processing in medical imaging. 1995. p. 263-274.

163. MARQUES, Jorge S.; ABRANTES, Arnaldo J. Shape alignment—optimal initial point and pose estimation. Pattern Recognition Letters, 1997, 18.1: 49-53.

164. NGUYEN, Minh Hoai; DE LA TORRE, Fernando. Metric learning for image alignment. International Journal of Computer Vision, 2010, 88.1: 69-84.

165. MARAI, G. Elisabeta; LAIDLAW, David H.; CRISCO, Joseph J. Super-resolution registration using tissue-classified distance fields. Medical Imaging, IEEE Transactions on, 2006, 25.2: 177-187.

166. TELENCZUK, Bartosz, et al. Molecular image registration using mutual information and differential evolution optimization. In: Biomedical Imaging: Nano to Macro, 2006. 3rd IEEE International Symposium on. IEEE, 2006. p. 844-847.

167. PENNEY, Graeme P., et al. Registration-based interpolation. Medical Imaging, IEEE Transactions on, 2004, 23.7: 922-926.

168. KEELING, Stephen L. Generalized rigid and generalized affine image registration and interpolation by geometric multigrid. Journal of Mathematical Imaging and Vision, 2007, 29.2-3: 163-183.

169. FRAKES, David H., et al. A new method for registration-based medical image interpolation. Medical Imaging, IEEE Transactions on, 2008, 27.3: 370-377.

170. ZHANG, Xiangjun; WU, Xiaolin. Image interpolation by adaptive 2-D autoregressive modeling and soft-decision estimation. Image Processing, IEEE Transactions on, 2008, 17.6: 887-896.

171. KEREN, Daniel. A probabilistic method for point matching in the presence of noise and degeneracy. Journal of Mathematical Imaging and Vision, 2009, 33.3: 338-346.

172. WILES, Andrew D., et al. A statistical model for point-based target registration error with anisotropic fiducial localizer error. Medical Imaging, IEEE Transactions on, 2008, 27.3: 378-390.

173. NICOLAU, Stéphane, et al. Evaluation of a new 3D/2D registration criterion for liver radio-frequencies guided by augmented reality. In: Surgery Simulation and Soft Tissue Modeling. Springer Berlin Heidelberg, 2003. p. 270-283.

174. LEE, Jae Sung, et al. Development and applications of a software for Functional Image Registration (FIRE). Computer methods and programs in biomedicine, 2005, 78.2: 157-164.

175. DICKSON, John C., et al. The impact of reconstruction method on the quantification of DaTSCAN images. European journal of nuclear medicine and molecular imaging, 2010, 37.1: 23-35.

176. MUTIC, Sasa, et al. Multimodality image registration quality assurance for conformal three-dimensional treatment planning. International Journal of Radiation Oncology* Biology* Physics, 2001, 51.1: 255-260.

177. SLOMKA, Piotr J.; BAUM, Richard P. Multimodality image registration with software: state-of-the-art. European journal of nuclear medicine and molecular imaging, 2009, 36.1: 44-55.

178. ALPERT, N. M., et al. Improved methods for image registration. NeuroImage, 1996, 3.1: 10-18.

179. IBANEZ, Luis, et al. The ITK software guide. 2003.

180. KLEIN, Stefan, et al. Elastix: a toolbox for intensity-based medical image registration. Medical Imaging, IEEE Transactions on, 2010, 29.1: 196-205.

181. AVANTS, Brian B.; TUSTISON, Nick; SONG, Gang. Advanced normalization tools (ANTS). Insight J, 2009.

182. ROSSET, Antoine; SPADOLA, Luca; RATIB, Osman. OsiriX: an open-source software for navigating in multidimensional DICOM images. Journal of Digital Imaging, 2004, 17.3: 205-216.

183. LOENING, Andreas Markus, et al. AMIDE: a free software tool for multimodality medical image analysis. Molecular imaging, 2003, 2.3: 131-137.

184. EICKHOFF, Simon B., et al. A new SPM toolbox for combining probabilistic cytoarchitectonic maps and functional imaging data. Neuroimage, 2005, 25.4: 1325-1335.

185. PAPADEMETRIS, Xenophon, et al. BioImage Suite: An integrated medical image analysis suite. The Insight Journal, 2005, 1: 3.

186. WAHL, Richard L. To AC or not to AC: that is the question. Journal of Nuclear Medicine, 1999, 40.12: 2025-2028.

187. TOWNSEND, David W. Positron emission tomography/computed tomography. In: Seminars in nuclear medicine. WB Saunders, 2008. p. 152-166.

188. SLART, Riemer HJA, et al. Diagnostic pathway of integrated SPECT/CT for coronary artery disease. European journal of nuclear medicine and molecular imaging, 2009, 36.11: 1829-1834.

189. XUE, Zhong; SHEN, Dinggang; DAVATZIKOS, Christos. Determining correspondence in 3-D MR brain images using attribute vectors as morphological signatures of voxels. Medical Imaging, IEEE Transactions on, 2004, 23.10: 1276-1291.

190. SHEKHAR, Raj, et al. High-Speed Registration of Three-and Four-dimensional Medical Images by Using Voxel Similarity 1. Radiographics, 2003, 23.6: 1673-1681.

191. ZAIDI, Habib, et al. Quantitative analysis in nuclear medicine imaging. New York: Springer, 2006.

192. SLOMKA, P. J., et al. Automated three-dimensional quantification of myocardial perfusion and brain SPECT. Computerized medical imaging and graphics, 2001, 25.2: 153-164.

193. HUTTON, Brian F.; BUVAT, Irene; BEEKMAN, Freek J. Review and current status of SPECT scatter correction. Physics in medicine and biology, 2011, 56.14: R85.

194. CERQUEIRA, Manuel D., et al. Standardized myocardial segmentation and nomenclature for tomographic imaging of the heart a statement for healthcare professionals from the cardiac imaging committee of the Council on Clinical Cardiology of the American Heart Association. Circulation, 2002, 105.4: 539-542.

195. HESSE, B., et al. EANM/ESC guidelines for radionuclide imaging of cardiac function. European journal of nuclear medicine and molecular imaging, 2008, 35.4: 851-885.

196. SHARIR, Tali, et al. A new algorithm for the quantitation of myocardial perfusion SPECT. II: validation and diagnostic yield. Journal of Nuclear Medicine, 2000, 41.4: 720-727.

197. MARIANI, Giuliano, et al. A review on the clinical uses of SPECT/CT. European journal of nuclear medicine and molecular imaging, 2010, 37.10: 1959-1985.

198. RUDD, James HF, et al. Imaging atherosclerotic plaque inflammation with [18F]-fluorodeoxyglucose positron emission tomography. Circulation, 2002, 105.23: 2708-2711.

199. TAKALKAR, Amol M.; EL-HADDAD, Ghassan; LILIEN, David L. FDG-PET and PET/CT-Part II. The Indian journal of radiology & imaging, 2008, 18.1: 17.

200. ČÍŽEK, Jiří, et al. Fast and robust registration of PET and MR images of human brain. Neuroimage, 2004, 22.1: 434-442.

201. GARCIA, Ernest V.; FABER, Tracy L. Advances in nuclear cardiology instrumentation: clinical potential of SPECT and PET. Current Cardiovascular Imaging Reports, 2009, 2.3: 230-237.

202. BADIAVAS, Kosmas, et al. SPECT imaging evaluation in movement disorders: far beyond visual assessment. European journal of nuclear medicine and molecular imaging, 2011, 38.4: 764-773.

203. LOI, Gianfranco, et al. Acceptance Test of a Commercially Available Software for Automatic Image Registration of Computed Tomography (CT), Magnetic Resonance Imaging (MRI) And 99mTc-methoxyisobutylisonitrile (MIBI) Single-Photon Emission Computed Tomography (SPECT) Brain Images. Journal of digital imaging, 2008, 21.3: 329-337.

204. ARDEKANI, Babak A., et al. A fully automatic multimodality image registration algorithm. Journal of computer assisted tomography, 1995, 19.4: 615-623.

205. SOLOMON, Chris; BRECKON, Toby. Fundamentals of Digital Image Processing: A practical approach with examples in Matlab. John Wiley & Sons, 2011.

206. GONZALEZ, Rafael C.; WOODS, Richard E. Digital image processing. 2002.

207. THÉVENAZ, Philippe; BLU, Thierry; UNSER, Michael. Interpolation revisited [medical images application]. Medical Imaging, IEEE Transactions on, 2000, 19.7: 739-758.

208. BEHRENBRUCH, C. P., et al. Image filtering techniques for medical image post-processing: an overview. 2014.

209. SAKAS, Georgios; POMMERT, Andreas. Processing and Segmentation of 3D Images. In: New Technologies in Radiation Oncology. Springer Berlin Heidelberg, 2006. p. 17-25.

210. GONZALEZ, Rafael C.; WOODS, Richard E.; EDDINS, Steven L. Digital image using Matlab processing. Person Prentice Hall, 2004, 183-193.

211. SURI, Jasjit S.; WILSON, David L.; LAXMINARAYAN, Swamy (ed.). Handbook of biomedical image analysis. Kluwer Academic/Plenum Publishers, 2005.

212. VAN DER HEIJDEN, Ferdinand, et al. Classification, parameter estimation and state estimation: an engineering approach using MATLAB. John Wiley & Sons, 2005.

213. SONKA, Milan; FITZPATRICK, J. Michael. Handbook of medical imaging(Volume 2, Medical image processing and analysis).

214. Zaret, B.L., M. Moser, L.S. Cohen. Yale University School of Medicine Heart Book. New York: Hearst Books, 1992.